EXPERIMENTAL AND NUMERICAL STUDY OF SONIC WAVE PROPAGATION

IN FREEZING SAND AND SILT

A

THESIS

Presented to the Faculty

of the University of Alaska Fairbanks

in Partial Fulfillment of the Requirements

for the Degree of

DOCTOR OF PHILOSOPHY

By

Hui Li, M.S.

Fairbanks, Alaska

May 2009

UMI Number: 3374164

INFORMATION TO USERS

The quality of this reproduction is dependent upon the quality of the copy
submitted. Broken or indistinct print, colored or poor quality illustrations
and photographs, print bleed-through, substandard margins, and improper
alignment can adversely affect reproduction.
In the unlikely event that the author did not send a complete manuscript
and there are missing pages, these will be noted. Also, if unauthorized
copyright material had to be removed, a note will indicate the deletion.

UMI®

EXPERIMENTAL AND NUMERICAL STUDY OF SONIC WAVE

PROPAGATION IN FREEZING SAND AND SILT

By

Hui Li

RECOMMENDED:
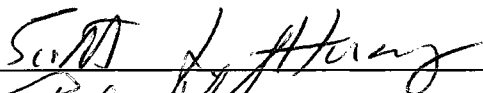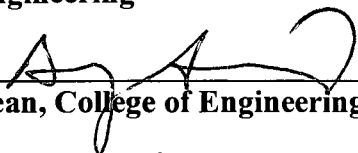
Advisory Committee Chair

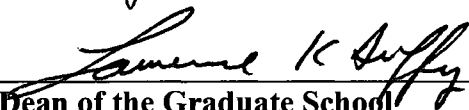Chair, Department of Mining and Geological
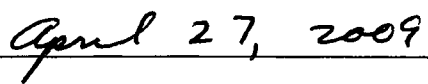Engineering

APPROVED:

Dean, College of Engineering and Mines

Dean of the Graduate School

Date   April 27, 2009

Abstract

A numerical model for delineating the temperature-velocity relationship of freezing porous media and soil is developed in Matlab based on Leclaire et al's Biot-type three-phase theory. Leclaire et al's theory gives lower sonic velocities than the experimental results because it does not take into consideration the effect of the solid-ice frame when water is freezing. To take the solid-ice effective frame into account, the average bulk and shear moduli estimation are modified with a proposed procedure. The modification gives higher P-wave and S-wave velocities that fit experimental data well. A comprehensive suite of physical and acoustic laboratory experiments are conducted on artificial sands, sand-clay mixtures and Fairbanks silts to investigate the temperature-velocity relationship during the freezing process and the effects of grain size and fine clay content.

A multi-channel ultrasonic scanning system (MUSS) is designed, installed and programmed for the experimental computerized ultrasonic tomography (CUST) study. The inward and outward freezing process and freezing front development in Fairbanks silt samples are observed using computerized ultrasonic tomography (CUST) in the laboratory. The experiments generate sonic wave velocity and temperature distribution during the freezing process. The freezing front is clearly identified in the CUST as a function of time and temperature. Comprehensive numerical finite element method (FEM) simulations, which account for the conduction in porous media, the latent heat effect and the nonlinear thermal properties of soil, are performed on the inward and outward

freezing process of Fairbanks silt based on the experimental conditions. In conjunction with the temperature-velocity model developed in the study, sonic wave velocity tomograms are generated. The results are comparable with those obtained by CUST. The study indicates that CUST is an effective method for studying freezing processes and has potential for indirect measurement of unfrozen water content variations in the soil without interfering with the freezing process.

Table of Contents

List of Figures

List of Tables

List of Appendices

Acknowledgement

I am grateful to my advisor, Dr. Gang Chen, for his advice and support, and for giving me the opportunity to conduct this research.

I am grateful to Dr. Yuri Shur, Dr. Scott Huang and Dr. Paul Metz for reviewing this work. I am thankful for their critical comments and useful suggestions for improving the quality of this thesis.

I would like to thank Dr. Wendy Zhou, Professor of Colorado School of Mines, who continually gave me support and advice and with whom I had many interesting discussions. I wish to express my gratitude to her.

I also thank Dr. Paul Metz for financial support. Moreover, I am grateful to the management and staff of the Department of Mining & Geological Engineering, and Institute of Northern Engineering (INE) for providing me with all facilities needed to conduct my research.

Financial support from EPSCoR is acknowledged.

Finally, deep thanks to my family and my wife.

Chapter 1. Introduction

1.1. Overview

Soil is a complex system made up of a heterogeneous mixture of solids, liquids, and gaseous materials. Soil freezing occurs when soil is cooled below 0 °C, when water in the soil crystallizes with decreasing temperature. Large areas of land with subsurface soil freezing are found worldwide. Artificial ground freezing is utilized in various engineering practices as well. Permafrost occurs over about 14 percent of the Earth's land surface, and the permafrost is over 1000 m thick in some regions (Washburn, 1980). Even at mid-latitudes, most of the ground surface is subject to seasonal or short-term freezing. Soil freezing in this manner is estimated to occur in almost 70 percent of the Earth's land surface. Soil is sometimes frozen artificially for various engineering applications since the mechanical strength of soil increases with freezing and its permeability dramatically decreases. For example, cold storage for farm produce and barriers against contaminant migration (Mohamed et al., 1995) have been constructed from soil kept frozen using refrigeration pipes. Artificially frozen ground is also utilized for underground tunnel construction in urban areas and for soft ground construction in caves and underwater (artificial soil freezing method). The soil around pipelines under construction in cold regions is also kept frozen to maintain a stable construction base (Nixon, 1987).

If soil expands when it freezes, the volume change is called frost heave. Clay particles in soil migrate as a result of frost heaving and thawing. The migration of clay

particles can change water paths and micro-pores in soil and damage irrigation and drainage systems in farmland. Disturbance of soil and changes of aggregated structure and hydraulic conductivity due to the action of freeze-thaw are also reported. The ground surface sometimes heaves upwards dozens of centimeters due to frost heaving and the heaving pressure can exceed 10 kPa. The heaving and subsidence of the surface causes much damage to paved roads, airports, railways, and foundations, etc.

When heaving occurs, some of the ice formed within the ground is present as seams of pure segregated ice; this ice is called an ice lens. The growth of ice lenses induces soil water to flow from the unfrozen zone toward the freezing front and the lens grows behind the frost front. In this case, some solutes illuviate to near the ground surface with the water flow, so that salinization occurs. If the ice lenses thaw and water collected near the ground surface runs off, soil loss can occur. The thawing of ice lenses softens the ground. Furthermore, construction piles or plant roots are sometime cut or extracted by frost heaving and ice lensing, so that the damage to piles or plants occurs in the field. With artificial soil freezing, unless the freezing is well controlled, frost heaving also occurs and affects the surrounding soil. Frost heave is also reported in concrete (Wang et al., 1996) and can damage the bases of dams and bridges. To overcome such frost-action damage, it is important to clarify the mechanism of frost heave.

Various features associated with frost action can be identified, such as solifluction and patterned ground in cold regions, where the ground undergoes repeated freezing and thawing (e.g. Washburn, 1980; Mackay, 1993). Pingos occur in Siberia, Alaska, and northern Canada. These are perennial frost mounds, 10 m or more in height, consisting of

surface soil and a core of massive ice. Soil freezing and frost heave play important roles in the formation of these landforms.

Knowledge of soil freezing is also required in the field of climate change and global warming. The surface layer of ground above the permafrost thaws in summer and freezes again in winter (active layer). When soil water in this layer melts, the melting water is not drained by infiltration because of the low hydraulic conductivity of permafrost (Bridges, 1978). Consequently, wetlands are a major feature in permafrost areas. Wetlands also are a major source of atmospheric greenhouse gasses. The surface soil of permafrost contains large quantities of stored carbon. If the permafrost soil thaws, this carbon may be released as carbon dioxide and methane (Kane, 1997).

Knowledge of the physical properties of freezing soils is fundamental for engineering development in cold regions such as the design and construction of highways and pipelines, the exploitation of mineral resources, and other projects. Most engineering practices in cold regions require in-depth understanding of permafrost properties, in particular the degree of freezing of the interstitial water.

Permafrost is a very dynamic substance since it may contain both ice and unfrozen water simultaneously and their proportion changes when the temperature changes. The physical and mechanical properties of permafrost are temperature sensitive, particularly when the temperature is near 0°C. The properties of permafrost that concern engineers may include sediment type, porosity factor, permafrost spatial distribution, content of ice and unfrozen water, frozen material strength under different temperatures, thermal

properties of frozen materials, and others. Much effort has been expended on measurements of permafrost and frozen ground, and valuable data have been accumulated and published in the literature. In additional to traditional geotechnical testing, various geophysical methods such as resistivity tomography, refraction seismology tomography, frequency-domain and time-domain electromagnetic induction methods, passive microwave radiometry, and the surface wave method have been used. Freezing has a marked effect on wave velocities (Timur, 1968). Therefore, seismic and acoustic logging methods constitute the best way to quantify the degree of ice and water saturation. Laboratory measurements of acoustic velocities in frozen porous media have been reported by several researchers (Nakano et al., 1972; King, 1977; and Kurfurst, 1976). All of them observed a sharp increase in velocities as the temperature was decreased to below 0°C.

In this study, experiments have been conducted to examine the feasibility and effectiveness of applying a relatively new technique –computerized ultrasonic tomography (CUST) for the observation of frozen front development and the measurements of freezing soil properties.

CUST, which relies on propagation of sonic/ultrasonic waves between two or more access drill holes to measure the velocity and signal strength of the propagated waves, has been successfully utilized to check the concrete integrity in dam and foundation structures. Other materials which support transmission of sonic waves, such as slurry, rock, grout, water-saturated media, and cemented radioactive wastes, can also be tested using sonic/ultrasonic waves. Sonic velocity is sensitive to material density, compressive

strength, porosity, ice and water content, and possibly thermal conductivity as well. The variation of sonic velocity in different media depends also upon the sonic frequency. Therefore, sonic velocity scanning with different pre-determined sonic wave frequencies may be utilized to quantitatively characterize the frozen ground and permafrost. The CUST technique may have the potential to be developed into an effective and efficient tool for laboratory measurements of frozen ground and permafrost properties.

1.2. The objectives of the study

The experimental and theoretical study of wave propagation in frozen media and frozen soil have been reported by a number of researchers, but, to the best of the author's knowledge, no research work has been conducted to study the dynamic soil freezing process by applying CUST. The objectives of the research presented in this dissertation are: 1) to study the dynamic physical and acoustic properties of freezing soil during the freezing process, and 2) to conduct FEM numerical simulations of sonic wave propagation in freezing soil and comparatively analyze the velocity tomograms obtained from CUST and FEM simulations. Figure 1.1 gives a graphical representation of the organization of this dissertation. The works conducted in this research include:

a) MUSS (Multi-channel Ultrasonic Scanning System) design, installation, and programming;

b) Laboratory sonic velocity testing of freezing media;

c) Laboratory ultrasonic scanning and P-wave velocity tomography study of inward and outward freezing process of Fairbanks silt;

d) Laboratory unfrozen water content (UWC) test using FDR;

e) Numerical estimation of temperature-velocity functions of Fairbanks silt using Matlab;

f) FEM simulation of inward and outward freezing process of Fairbanks silt using Comsol Multiphysics;

g) Comparative analyses of velocity tomography obtained from CUST and FEM simulation.

A comprehensive suite of physical and acoustic laboratory experiments were conducted on artificial sand, a sand-clay mixture, and Fairbanks silt. Table 3.1 gives a summary of sand and soil tests conducted in this research. The experiments were designed to investigate the temperature-velocity relationship of sand and soil during the freezing process, and the effects of the grain size and fine (clay) content. The numerical temperature-velocity models of wave propagation in freezing sand and soil were reconstructed in Matlab, and the necessary modifications were made to suit the experimental data.

Two physical models of Fairbanks silt were built and the inward and outward freezing process and freezing front development of the Fairbanks silt samples were observed using MUSS. Velocity tomograms were generated using the simultaneous iterative reconstruction technique (SIRT) to perform tomographic inversions.

The comprehensive numerical FEM simulations, which take into account the conduction in porous media, the latent heat effect, and the nonlinear thermal properties of soil, were performed on the inward and outward freezing process of Fairbanks silt. The

velocity tomograms were obtained based on simulation output of temperature

distributions in the FEM model and the derived temperature-velocity relationship.
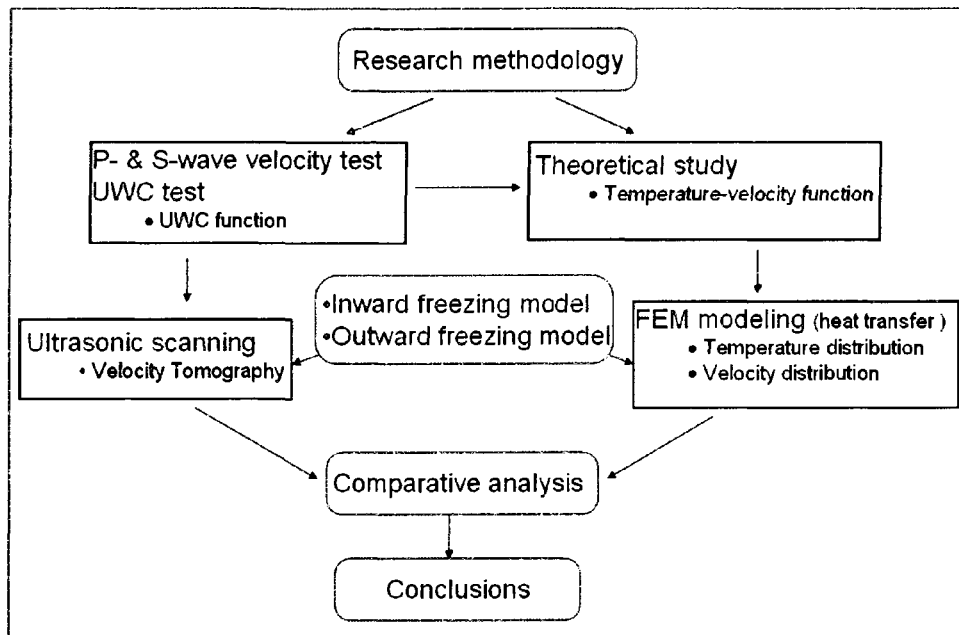
Figure 1-1. Flowchart detailing the organization of this dissertation

After an introduction in Chapter 1, Chapter 2 summarizes the literature review,

which focuses on laboratory work, associated theoretical approaches and numerical

modeling on the acoustic and thermal properties of freezing soils related to this research.

Chapter 3 contains a detailed description of all laboratory and numerical methods and

procedures used in this research, including the unfrozen water content measurement,

acoustic velocity measurement, ultrasonic velocity scanning and tomogram generation,

temperature-velocity modeling, and the FEM simulation procedures. The laboratory

velocity test results of samples and numerical temperature-velocity modeling results are

presented in Chapter 4. The numerical temperature-velocity models for Fairbanks silt are

reconstructed in Matlab based on Leclaire et al's Biot-type three-phase theory, which considers the existence of two solids (solid and ice matrices) and a liquid (unfrozen water) and also assumes that there is no direct contact between solid grains and ice. The model gives lower velocities than the experiment results because it does not account for the effect of the solid-ice frame when water is freezing. To take the solid-ice effective frame into account, we modified the average bulk and shear moduli estimation by Minshull et al's model (1994), and this modification gives higher P-wave and S-wave velocities which fit the experimental data well. Chapter 4 also includes the unfrozen water content test results and an analysis of the effect of grain size and clay content on acoustic velocity. Laboratory ultrasonic scanning and P-wave velocity tomography study results of the inward and outward freezing process of Fairbanks silt are presented in Chapter 5. FEM simulation results, temperature distributions and velocity distributions of inward and outward freezing process of Fairbanks silt using Comsol Multiphysics are presented in Chapter 6. Chapter 6 also includes a comparative analysis of velocity tomography obtained from CUST and FEM simulation. Finally, Chapter 7 contains the summaries and conclusions, as well as suggestions for future research.

Chapter 2. Literature Review on Characteristics of Freezing Soil and Associated Theories

This chapter presents a review of the important literature related to laboratory work, associated theoretical approaches and numerical modeling of the acoustic and thermal properties of freezing soils.

In the past few decades, a number of excellent summaries and reviews of experimental and theoretical studies of the physical, acoustic and thermal properties of freezing soil have been written. Barnes (1963) compiled a summary of the compressional wave velocity data obtained in permafrost regions for over twenty-five years. Zykov (1966) reviewed Russian works on this subject. Kay and Perfect (1988) and Ladanyi and Shen (1989) presented reviews of heat and mass transfer, and of frost heave theories in freezing soil. Anderson and Morgenstern (1973) presented a comprehensive review of physics and chemistry as related to frozen ground. Their paper included summaries of x-ray diffraction studies of clay-water mixtures and experiments using the nuclear magnetic resonance method, as well as other methods for unfrozen water content measurements. Henry (2000) presented reviews of the thermodynamics of freezing soils.

2.1. Characteristics of freezing soil

Soil is a very complex system made up of a heterogeneous mixture of solids, liquids, and gaseous materials. Some water in soil remains liquid well below the freezing point (0 °C). In order to observe and model the freezing process, we first need to understand

the mechanisms of water and heat migration and the liquid-solid phase transition of water during soil freezing.

The classic research focuses of soil freezing is on mechanisms and thermodynamics associated frost heave and ice lensing. Over the last century, the study of frost heave became a major topic in civil engineering, with research into measures against frost heave, the utilization of frozen soil, and soil stabilization.

Soil freezing was regarded as a unidirectional heat transfer problem until the 1930s. It was then understood to be a problem of coupling the water and heat fluxes with a boundary at the freezing front, although the mechanism of ice lensing was not yet understood. After 1950, numerous theoretical and semi-empirical models were developed, with the intention of clarifying the mechanism of ice lensing or predicting and overcoming damage due to frost heave. In the 1960s and 70s, frost heave was described by capillary theory, which explained the generation of ice lenses, and by semi-empirical hydrodynamic models. However, these models do not sufficiently explain the formation of intermittent layers of ice lenses in the soil freezing process. In the mid-1970s, a secondary frost heave theory that can explain the formation of intermittent layers was proposed. Takashi et al's theory and concept (1974) of segregation potential have also been used to predict and overcome frost heave. Presently, the models most often used for frost heave and ice lensing are the capillary theory, the secondary frost heave theory, and the segregation potential concept. These models and theories, however, still leave much to be physically explained, and some have not been developed fully. Recently, approaches to understanding ice lensing based on thermodynamics, crystal growth, and

intermolecular forces have appeared. Nevertheless, no theories or models fully explain the mechanism of ice lensing.

2.1.1. Unfrozen water content (UWC)

Faraday (1859) believed that liquid water exists on the surface of ice at temperatures below its freezing temperature. This water, which does not freeze below the bulk freezing temperature, is called unfrozen water. Although most soil water freezes when it is cooled to below 0 °C, releasing latent heat, water adjacent to particles does not freeze, even when it is cooled substantially. Therefore, there is a film of unfrozen water on the surface of particles. It is believed that water flowing through the film plays an important role in the growth of ice lenses (Loch and Kay, 1978; Horiguchi and Miller, 1980; Ishizaki, 1995). The amount of unfrozen water in soil decreases drastically at near sub-zero temperatures (-0 °C) and decreases further with decreasing temperature. A change in the amount of unfrozen water strongly influences soil properties, such as strength, permeability, and thermal conductivity. Furthermore, the amount of unfrozen water will change with pressure, the surface area of soil particles, soil components, and so on. The factors affecting the amount of unfrozen water include specific surface area, temperature, and overburden pressure; osmotic potential of the soil solution; fine pore geometry of mineral grains; particle packing geometry; surface charge density; and exchangeable ions (Anderson and Tice, 1972; Darrow et al., 2008).

The presence of unfrozen water is accounted for using the free energy concept. When water is cooled to below 0 °C, ice, which has an orderly molecular arrangement

with lower energy, is more stable than liquid water, which has a disordered molecular arrangement. On the other hand, breaking hydrogen bonds on the ice surface increases the interfacial free energy. When liquid water exists between ice and the soil surface, the interfacial free energy is lower than when ice contacts the soil surface directly:

$$\gamma_{is} > \gamma_{iw} + \gamma_{ws} \qquad \text{(Eq. 2-1)}$$

where γ_{is}, γ_{iw} and γ_{ws} are the interfacial free energy per unit area between ice and soil, ice and liquid water, and liquid water and soil, respectively.

The film of unfrozen water exists between ice and soil particles in order to minimize the free energy of the system considered. The presence of unfrozen water has also been explained from the viewpoint of intermolecular forces (Dash et al., 1995).

Solutes and pores in soil induce freezing-point depression, so that they have a great effect on the presence of unfrozen water. The depression of the freezing point ΔT_f associated with a solute is known as Raoult's Law:

$$\Delta T_f = -iK_f C \qquad \text{(Eq. 2-2)}$$

where C is the molality, i is Van't Hoff's factor, which indicates the electrolytic dissociation of the solute, and K_f is the molar cryoscopic constant. K_f in soil is about 1.86 K kg/mol. If water in saline soil, for instance, contains a solute with a concentration of 0.025 mol/kg and i = 2, we obtain $\Delta T_f = -0.1°C$. The depression of the freezing point associated with the capillary of a cylindrical pore with radius r_p is explained by the

balance between the free energy of the system considered and the solid-liquid interfacial

energy and is given by

$$\Delta T_f = \frac{3 V_w \times T_m \times \gamma_{iw}}{L \times r_p}$$

(Eq. 2-3)

where V_w is the specific volume of water, T_m is the bulk freezing point of water,

and L is the latent heat. With values $V_w = 20 \times 10^{-6}$ m³/mol, $T_m = 273.15$ K,

$L = 6000$ J/mol, and $\gamma_{iw} = 35 \times 10^{-3}$ J/m², the depression of the freezing point is 1.0 °C when

$r_p = 0.1$ μm.

Considerable progress has been made toward understanding the nature of the

unfrozen water that persists in soils at temperatures below the freezing temperature of

bulk water (Dash et al., 1995; Wettlaufer and Worster, 1995). The focus of the work by

Dash et al. (1995) and Wettlaufer and Worster (1995) is on isolating the roles that

curvature, confinement in pores, physical characteristics of ice surfaces, and the presence

of impurities in soil water play on the thickness and mobility of unfrozen water in

freezing soils.

Many methods have been used to measure the amount of unfrozen water in frozen

soil, e.g., X-ray diffraction (Anderson and Hoekstra, 1965), dilatometry (Pusch, 1979),

diabatic calorimetry (Kolaian and Low, 1963), isothermal calorimetry (Anderson and

Tice, 1971,1972,1973), differential scanning calorimetry (DSC) (Handa et al., 1992),

nuclear magnetic resonance methods (NMR) (Tice et al., 1982; Tice and Oliphant, 1984;

Kuyala, 1989; Ishizaki, 1995; Ishizaki et al., 1996), frequency domain reflectometry

(FDR) and time domain reflectometry (TDR) (Topp and Davis, 1985; Spaans and Baker, 1995) and many other methods (Kozlowski, 1995). NMR and DSC are best used for accurate measurements in the laboratory with the ability of continuous phase changes monitoring during freezing or thawing of an individual soil sample. TDR is best used for field observations, due to its portability.

The NMR technique is one of the most accurate methods for determining the unfrozen water content of soils (Tice et al., 1982), as it depends on the spatial density of hydrogen atoms in the sample. The NMR signal from hydrogen nuclei is proportional to the population of hydrogen atoms in the sample, and the signal relaxation rate is proportional to the porosity. A drop in NMR signal intensity is observed during the soil freezing process, corresponding with the hydrogen proton of liquid water.

TDR measures the bulk soil dielectric permittivity based on the speed of propagation of a transverse electromagnetic wave and has been used successfully to measure soil moisture content over decades. Once instruments are properly calibrated and installed, accuracies of better than 0.05 m^3 m^{-3} arc usually quoted for TDR (e.g. Topp et al., 1980). TDR is one of the most popular techniques for measuring soil moisture content, but the cost of the system is still high. Smith and Tice (1988) compared nuclear magnetic resonance (NMR) and TDR measurements of the unfrozen water content of frozen soil and found a linear relationship between the two. They concluded that very accurate measurements were possible using TDR for unfrozen water content determinations. The NMR method is restricted to the laboratory.

FDR sensors measure some parameters that depend on the relative dielectric permittivity of the materials in which they are embedded. FDR methods of moisture measurement are also known as radio frequency (RF) capacitance techniques.

Laboratory comparison of five FDR and TDT probes and the reference sensor (NMR) (Yoshikawa and Overduin, 2005) indicated reasonable accuracy in measurements of moisture content in frozen soil by electromagnetic means. They concluded the FDR probes are capable of assessing unfrozen water content. They also provided unique exponential calibration equations to obtain unfrozen water content from probe output for clay (bentonite) and Fairbanks silt.

The amount of unfrozen water depends on temperature, pressure, water salinity, and the mineralogy and specific surface area of the soil (Dillon and Andersland, 1966; Anderson and Tice, 1972; Anderson and Morgenstern, 1973). There are several empirical formulae for predicting the amount of unfrozen water based on these experimental results (Anderson and Tice, 1972; Ishizaki et al., 1996).

Ivanov (1962) described the change of phase constitution of pore water in freezing soil due to temperature by the formula

$$W_u = W_0 + A(\frac{1}{1 + \alpha|\Delta t| + \beta \Delta t^2} - 1)$$

(Eq. 2-4)

where W_u is gravimetric unfrozen water content, %;

$\Delta t = T - t_f$; t_f is a freezing point of moisture, °C;

W_0 is an equilibrium value of moisture content at t_f;

A, α and β are parameters depending on a soil type. Over small ranges

of freezing temperatures ($|\Delta t| \leq 10^\circ C$), $\beta = 0$.

Table 2-1 gives the parameters of the formula for basic types of alluvial soils by

Votyakov (1975). Figure 2.1 shows their mean curves of unfrozen water content, UWC.

Table 2-1. Values of parameters in formula

Soil type	W_0	t_f, $^\circ C$	A	α
Sand	0.2	-0.1	0.198	12.75
Sandy loam	0.2	-0.3	0.182	4.78
Clayey loam	0.2	-0.6	0.158	2.34
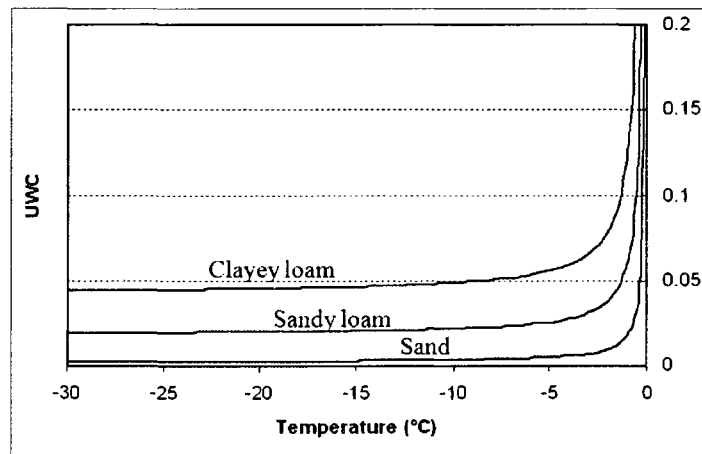
Figure 2-1. The UWC vs. temperature of typical soils, from Votyakov (1975)

Anderson and Tice (1972) fit freezing characteristic data for a number of soils to the

general equation

$$W_u = A|T|^B$$
<div align="right">(Eq. 2-5)</div>

where W_u is gravimetric unfrozen water content, %;

T is temperature, °C;

W_0 is an equilibrium value of moisture content at t_f ;

A , B are the empirical parameters depending on a soil type.

For Fairbanks silt, values of A and B reported by Anderson and Tice (1972) are 4.8 and -0.326, respectively.

2.1.2. Phase change and ice formation

There are two types of ice in freezing soil. One is pore ice, which forms among soil particles in situ and barely causes the particles to move. The other is an ice lens, which forms by excluding particles and segregates from the soil matrix. Both forms of ice have a crystal structure of I_h (hexagonal crystal) and form perpendicular to the direction of heat flow. Thin section observation has also shown that the crystals in an ice lens grow along its a-axis.

Ice formation in soil is regarded as a phase transition phenomenon from liquid to crystal. When soil water is cooled below the freezing point, ice has a lower energy than liquid water. Therefore, the change in the free energy explains ice formation:

$$G = H - TS$$

where G is the Gibbs free energy, H is enthalpy, T is temperature, and S is entropy.

Ice forms to minimize the free energy G in a temperature and pressure envelope. Assuming that ice forms at T_m, where the solid and liquid phases have the same free energy ($\Delta G_i = \Delta G_w$), this can be generalized in the Clausius-Clapeyron equation as

$$V_w dP_w - V_i dP_i = L\frac{dT}{T_m}$$

(Eq. 2-6)

where V_w and V_i are the specific volumes of liquid water and ice, respectively, and P_w and P_i are the respective pressures of liquid water and ice. Ice formation has been expressed using equation (5) in numerical studies of the mechanism of ice lensing and frost heave (e.g. Radd and Oertle, 1973; Biermans et al., 1978; Gilpin, 1980; Nixon, 1991; Black, 1995).

2.1.3. Water migration during soil freezing

Soil water flows downward due to gravitation and flows upward due to evaporation and transpiration. The major driving force of water flow in saturated soil is gravity. In saturated soil, the gravitational flow may be written using Darcy's Law. In addition, capillary force plays an important role for flow in unsaturated soil.

Frozen soil is permeable, even though with a very low permeability, since it contains liquid (unfrozen) water. If different parts of a frozen soil are at different pressures or temperatures, the soil water will flow between them. It has been experimentally

confirmed that Darcy's Law also governs the water flow in frozen soil. The water flow in freezing soil is considered to arise from gravity, ice lensing, and heat transfer. The full mechanism of such flow, however, is not yet clear, posing a great challenge for frost heave studies.

The hydraulic conductivity of frozen soil depends on the nature of the soil and the amount of unfrozen water. Since the amount of unfrozen water declines sharply with temperature, the hydraulic conductivity strongly depends on the temperature. It is reported that the hydraulic conductivity of soil decreases by ten times when the temperature changes from 0 °C to -1 °C. The hydraulic conductivity and its change with temperature are important factors when considering the mechanism of frost heave, and a number of researchers have therefore tried to determine these values (e. g. Loch and Kay, 1978; Konrad, 1980; Ishizaki et al., 1985; Black and Miller, 1985).

2.1.4. Heat transfer during soil freezing

When considering heat transfer in soil, the thermal properties of the soil, such as specific heat, heat capacity, thermal conductivity, and thermal expansion, are important. The thermal properties depend on the nature and proportions of the soil elements, i.e., soil minerals, water, ice, and gases. The thermal properties of frozen soil differ from those of unfrozen soil. In addition, latent heat arising from ice formation must be considered in soil freezing.

In soil, heat is transferred mainly by conduction. When mass transfer and latent heat are neglected, the heat transfer in a non-steady state is described by the Fourier equation:

$$Q = -k(T_2 - T_1)\frac{A}{d}$$

(Eq. 2-7)

where Q is the heat flux, T_1 and T_2 are the respective temperatures at points 1 and 2, d is the distance between 1 and 2, A is the area, and k is the thermal conductivity of the soil. If the change in the thermal conductivity due to the change in temperature is negligible, equation (2-7) becomes

$$k\frac{\partial^2 T}{\partial x^2} = \rho C\frac{\partial T}{\partial t}$$

(Eq. 2-8)

where ρ is the density of the soil, C is the specific heat of the soil, t is time, and x is location. Considering the latent heat arising from ice formation in an infinitesimal region, the heat transfer in a non-steady state is given by

$$k\frac{\partial^2 T}{\partial x^2} = \rho C\frac{\partial T}{\partial t} - L\rho_w\phi$$

(Eq. 2-9)

Consequently, heat transfer in freezing soil can be expressed by applying equations (2-8) and (2-9) to the frozen and unfrozen regions.

When the soil sample is freezing from one side to another, water in the soil pores flows toward the freezing front from unfrozen region because of a gradient in the soil moisture pressure (or tension). This occurs even when the soil pores are not saturated. Ice lenses form and grow at or slightly behind the freezing front and cause great uplifting forces so that frost heave occurs. Thermodynamics, or the study of heat and work and the conversion of one of these energy forms to the other, provides a means of understanding the soil freezing process.

The first researchers to make significant progress in understanding frost heave were Taber and Beskow. Taber (1929, 1930) proved that frost heave is not solely caused by the volume expansion of water upon freezing and introduced the idea that frost heave is dependent on freezing rate and occurs in a direction perpendicular to heat flow.

Beskow (1935) contributed the important idea that frost heave is analogous to soil drying and that in fine-grained soils frost heave is sometimes limited by water flow in the soils. He also noted that increasing effective stress (by some combination of lowering the water table and increasing the overburden pressure) reduces the rate of frost heave of a soil, all other things being equal. Beskow incorrectly concluded that frost heave rate in saturated soils is independent of freezing rate, so his generalizations about frost heave are correct only at a constant rate of freezing.

Everett (1961) applied equilibrium concepts to explain frost heave. He considered the mechanical equilibrium between pore ice and pore water, thereby concluding that the maximum pressure difference in a heaving soil is determined by the smallest pore sizes. This was an important theoretical advancement; it provided a qualitative explanation for what is now known as primary frost heaving. However, he did not consider temperature and chemical effects that can result in even smaller radii of curvature between ice and water in soil pores (leading to greater ice-water pressure differences).

Miller et al. (1960), Miller et al. (1975), and Loch (1978) developed a more complete understanding of thermodynamic equilibrium of pore ice and water; thus, chemical and thermal equilibrium are included. The Generalized Clapeyron Equation, based on the

equilibrium of ice and water in soils, is utilized by the thermodynamically based models of Miller (1978) and Gilpin (1980).

Miller (1978) and Gilpin (1980) used the equilibrium relationships as described by Loch (1978) and added heat and mass transfer in the frozen fringe to model frost heave. Darcy's Law and Fourier's Law describe heat and mass transfer, respectively, in the frozen fringe, and mass flow and heat flow are coupled by one equation that describes heat transfer in the frozen soil. Ice lenses start to grow when the effective stress in the frozen fringe becomes zero (Miller, 1978; Gilpin, 1980). The rigid ice model assumes that ice is one continuous rigid body that grows by regelation (Miller, 1978). Gilpin's model also assumes that the ice forms a continuous three-dimensional network, but it remains stationary in the frozen fringe. The main difference between the models is that Gilpin made a few reasonable simplifying assumptions that allowed the model to be programmed rather easily. However, more recent work with the rigid ice model has made it relatively easy to use (Black, 1995). Both models predict the same qualitative frost heave behavior, and are similar quantitatively. The rigid ice model is also the basis for the more recently developed numerical model used to predict frost heave in the field known as PC heave (Sheng, 1994).

Regarding the ability to predict the deformation of soils in response to freezing or thawing, engineers have had great success in predicting material behavior by treating it as a continuum. Blanchard and Fremond (1985) published a model of soil frost heaving and thaw settlement that utilized the continuum approach. The constitutive laws used to describe the soil behavior were elastic for the unfrozen soil and viscoplastic when frozen.

Michalowski (1992, 1993) extended that work to account for more factors affecting frost

heave (e.g., three-dimensional stress state of the soil). He used constitutive relations to

describe the rate of deformation of the soil during frost heave, as well as the constitutive

relations of heat conduction (Fourier's Law), water flow (Darcy's Law), and a

constitutive law describing the relation between stress and strain in the frozen soil or soil

skeleton. Recently, Hartikainen and Mikkola (1997) reported progress on using

equilibrium thermodynamics to predict the movement and phase change of water in

freezing soil, along with constitutive models to predict the deformation of the soil due to

frost heave.

2.2. Wave propagation in freezing soil

Modeling the acoustic properties of fluid-saturated porous media implies quantifying

the variations of wave velocities V_P, V_S and their amplitudes versus porosity, fine grain

content and frequency.

Gassmann (1951) derived a relation between the individual elastic properties of the

solid fabric (skeleton, matrix) and the effective elastic properties of the composite

medium.

Biot (1956 a, b) developed a complete poro-elasticity theory for the propagation of

acoustic waves in fluid-saturated porous solids. He developed different theories for the

low- and high-frequency waves. For low-frequency waves, the concept of Poiseuille flow

was used, while for the high-frequency range, this concept breaks down, and potential

flow is used instead. Biot found that in general there are two P-waves present, one slow

and one fast. Biot's theory has been tested and confirmed (Plona and Johnson, 1980; Berryman, 1980) and successfully applied for the interpretation of seismic waves observed in geophysics (Bourbie et al., 1987).

Soils (unconsolidated sediments), as sophisticated porous media, are often in the permanently frozen state in arctic regions. A number of studies have demonstrated that ice in the pore spaces of sediments can cause large increases in seismic velocity over the velocity when the interstitial water is unfrozen. Factors influencing the fraction of ice formed in the pore spaces of sediments are the temperature, the moisture content, the pore sizes and shapes, the pore water chemistry, and the states of stress in both the solid frame and the pore fluid. Theoretical aspects of these factors were discussed in great detail by Anderson and Morgenstern (1973). Timur (1968), Nakano et al. (1972), Kurfurst (1976), King (1977), Pandit and King (1979), King et al. (1982) and Zimmerman and King (1986) described experimental studies of these factors.

The first published laboratory measurements of compressional wave velocity (V_P) in porous media with ice filling the pore spaces were performed by Müller (1961), from Germany, to study the proposed excavation of mine shafts by a freezing method. He measured the compressional wave velocity in water-saturated sand and clay packs of various porosities as a function of decreasing temperature. Analysis of Müller 's data, based on the time-average formula (Wyllie et al., 1956 and 1958) used for approximating velocity in mineral-fluid or mineral-ice mixtures, gives a low compressional wave velocity for ice, 2500 m/s, compared to 3570 m/s, but a high velocity for quartz matrix, 6250 m/s, compared to 5943 m/s (Wyllie et al., 1958).

Frolov (1961) measured the velocities of 30 kHz compressional waves in four

different types of earth materials (sand, clay, sandstone, and silt) in the temperature range

from -20°C to 20°C.

Kaplar (1963) measured both the compressional and shear wave velocities in various

frozen earth materials in the temperature range from 0°C to -20°C by the resonant bar

method, in which flexural, longitudinal, or torsional vibrations are induced by

electromagnetic means.

Barnes (1963) compiled a summary of the compressional wave velocity data

obtained in permafrost regions for over twenty-five years. Later, Zykov (1966) reviewed

Russian works on this subject.

Desai and Moore (1967) reported laboratory measurements of compressional wave

velocity in Berea Sandstone at freezing temperatures. They observed a 45% increase in

velocity upon freezing of Berea Sandstone saturated with 15,000 ppm brine and a slight

increase in velocity in dry and oil-saturated cores. Using a time-average equation, they

expressed their results in terms of a decrease in the matrix travel time from 3465 m/s at

20°C to 5542 m/s at -24°C. They attributed most of this decrease to the pressure of

expanding ice in the pore spaces upon the rock matrix.

Timur (1968) concluded from studies of acoustic wave propagation in sedimentary

rocks at permafrost temperatures that, as the temperature is decreased below 0°C, ice

forms first in the larger pore spaces, and then in progressively smaller ones. He attributed

this behavior to steadily increasing interfacial forces associated with the larger specific

surface areas of smaller pores. Nakano et al. (1972), King (1977), Pandit and King (1979)

and King et al. (1982) confirmed Timur's hypothesis during measurements of elastic

wave velocities, electrical resistivity, and thermal conductivity of samples of natural

permafrost and different water-saturated porous rocks at temperatures below 0°C. Timur

(1968) proposed a three-phase time-average equation based on slowness averaging

(Wyllie's equation) for calculating the fraction of ice in the pore spaces of consolidated

permafrost sediments:

$$\frac{1}{v} = \frac{(1-S_i)\phi}{v_l} + \frac{S_i\phi}{v_i} + \frac{(1-\phi)}{v_m}$$

(Eq. 2-10)

where $\quad S_i$ is the relative fraction of pore space occupied by ice;

ϕ is porosity;

v_l and v_i are velocities in interstitial liquid and ice, respectively; and

v_m is the velocity in the matrix material.

However, this particular relation only applies to consolidated porous rocks for which

there is a continuous rock-matrix phase. It is inapplicable to soils or unconsolidated

permafrost sediments unless an artificially low value is used for the matrix velocity

(Hoyer et al., 1975).

Nakano et al. (1972) measured ultrasonic velocities of the P- and S-waves in

water-saturated frozen soils as a function of temperature by both pulse first arrival and

critical angle methods from -19°C to 5°C. A strong correlation exists between P-wave

velocities and unfrozen water content. The observed hysteresis in the velocities of silt and

clay during a freeze-thaw cycle is considered to be caused by hysteresis in the frozen water content. A general tendency for the shear wave velocity to decrease with ascending temperature exists, but the effect of temperature is not as pronounced as on the P-wave velocity. Calculations based on measured dilatational and shear velocities showed that the Poisson's ratios of sand are almost constant. However, the ratios of silt and clay decrease monotonically with ascending temperature.

King et al. (1982) proposed a three-phase (mineral grain, ice, and water) model for the elastic wave velocities in unconsolidated permafrost. His model is based on the Kuster and Toksöz (1974) two-phase scattering theory. King concluded experimentally that the P-wave velocity in unconsolidated permafrost correlates fairly well with the water-filled porosity.

A number of two- and three-phase models are listed below:

1) Phenomenological and two-phase models

Several two-phase models have been adapted for modeling the wave velocity of a three-phase medium. The basic material properties and their descriptions are listed in Appendix A. All the models assume that the constituents move together, so that the composite density is simply the volume-weighted average of the densities of the constituents, given by

$$\rho = \phi_w \rho_w + \phi_i \rho_i + \phi_s \rho_s$$
(Eq. 2-11)

provided that $\phi_w + \phi_i + \phi_s = 1$. The compressional- and shear-wave velocities are then given by

$$V_p = \sqrt{\frac{K + 4G/3}{\rho}}$$

(Eq. 2-12)

$$V_s = \sqrt{\frac{G}{\rho}}$$

(Eq. 2-13)

where K is the composite bulk modulus and G is the composite shear modulus.

Voigt's model:

This model (Voigt, 1928) is based on hulk modulus averaging (isostrain assumption). The composite moduli are given by

$$K = \phi_w K_w + \phi_i K_i + \phi_s K_s$$

and

$$G = \phi_i \mu_i + \phi_s \mu_s$$

Reuss's model:

Reuss's model (Reuss, 1929), also known as Wood's model (Wood, 1941), averages the reciprocal of the bulk moduli (isostress assumption). The composite bulk modulus is obtained from

$$\frac{1}{K} = \frac{\phi_w}{K_w} + \frac{\phi_i}{K_i} + \frac{\phi_s}{K_s}$$

and the shear modulus is obtained from

$$\frac{1}{G} = \frac{\phi_i}{\mu_i} + \frac{\phi_s}{\mu_s}$$

for $\phi_w = 0$ and $G = 0$ for $\phi_w \neq 0$. These equations have been proved useful for

emulsions and suspensions of solid particles in a continuous liquid phase (unconsolidated

sediments) (White, 1965; Schön, 1996).

Time-average model:

Wyllie, Gregory and Gardner (1956) introduced the time-average formula that

consists of slowness averaging. The composite moduli are obtained from

$$\sqrt{\frac{\rho}{K + 4G/3}} = \phi_w \sqrt{\frac{\rho_w}{K_w}} + \phi_i \sqrt{\frac{\rho_i}{K_i + 4\mu_i/3}} + \phi_s \sqrt{\frac{\rho_s}{K_s + 4\mu_s/3}}$$

and

$$\sqrt{\frac{\rho}{G}} = \phi_i \sqrt{\frac{\rho_i}{\mu_i}} + \phi_s \sqrt{\frac{\rho_s}{\mu_s}}$$

if $\phi_w = 0$ and $G = 0$ for $\phi_w \neq 0$.

This model was applied by Timur (1968) to consolidated permafrost sediments.

Minshull et al's model:

Application of Gassmann's two-phase equation (Gassmann, 1951) to permafrost

follows the work by Minshull et al. (1994), who used the equation for modeling partially

hydrated sediments. First, the time-average relationship is used to determine the moduli

K_1 and G_1 for full ice saturation,

$$\sqrt{\frac{\rho_1}{K_1 + 4G_1/3}} = \phi_s \sqrt{\frac{\rho_s}{K_s + 4\mu_s/3}} + (1-\phi_s)\sqrt{\frac{\rho_i}{K_i + 4\mu_i/3}}$$
(Eq. 2-14)

$$\sqrt{\frac{\rho_1}{G_1}} = \phi_s \sqrt{\frac{\rho_s}{\mu_s}} + (1-\phi_s)\sqrt{\frac{\rho_i}{\mu_i}}$$
(Eq. 2-15)

where $\rho_1 = \phi_s \rho_s + (1-\phi_s)\rho_i$. Secondly, Gassmann's equation determines the moduli for

the water-filled sediment:

$$K_2 - K_{sm} = \frac{(1 - K_{sm}/K_s)^2}{(1-\phi_s)/(K_w + \phi_s/K_s - K_{sm}/K_s^2)}$$
(Eq. 2-16)

$$G_2 = \mu_{sm}$$

with $\rho_2 = \phi_s \rho_s + (1-\phi_s)\rho_w$.

Finally, the moduli for partial saturation are obtained by slowness averaging as

$$\sqrt{\frac{\rho}{K + 4G/3}} = (1-s)\sqrt{\frac{\rho_1}{K_1 + 4G_1/3}} + s\sqrt{\frac{\rho_2}{K_2 + 4G_2/3}}$$
(Eq. 2-17)

$$\sqrt{\frac{\rho}{G}} = (1-s)\sqrt{\frac{\rho_1}{G_1}} + s\sqrt{\frac{\rho_2}{G_2}}$$
(Eq. 2-18)

where $s = \phi_w/(1-\phi_s)$ is the water saturation.

Zimmerman and King's model:

Zimmerman and King (1986) used the two-phase theory developed by Kuster and

Toksöz (1974), assuming that unconsolidated permafrost can be approximated by an

assemblage of spherical quartz grains embedded in a matrix composed of spherical

inclusions of water and ice. Following King et al. (1982), they assume unconsolidated

permafrost can be approximated by an assemblage of spherical quartz grains imbedded in

a matrix composed of spherical inclusions of water in ice. They then used Kuster and

Toksöz's (1974) theory to calculate the wave speeds as functions of the porosity, Φ, and

the fraction of pore space filled with water [denoted by s, so that the extent of freezing is

(1 - s)]. For a two-phase material comprising a continuous matrix permeated with

spherical inclusions, the Kuster- Toksöz equations for the effective bulk and shear moduli

K and G are

$$\frac{K}{K_m} = \frac{1 + [4G_m(K_i - K_m)/(3K_i + 4G_m)K_m]c}{1 - [3(K_i - K_m)/(3K_i + 4G_m)K_m]c}$$

(Eq. 2-19)

and

$$\frac{G}{G_m} = \frac{(6K_m + 12G_m)G_i + (9K_m + 8G_m)[(1-c)G_m + cG_i]}{(9K_m + 8G_m)G_m + (6K_m + 12G_m)[(1-c)G_i + cG_m]}$$

(Eq. 2-20)

where subscripts m and i indicate "matrix" and "inclusion" and c is the inclusion

concentration. They apply these equations to the three-phase permafrost model by first

computing the effective elastic moduli of the ice-water mixture, with ice playing the role

of matrix phase and water that of inclusion phase. Parameter s represents the inclusion

concentration. The quartz sand grains are imagined as imbedded in a homogeneous

medium with the same (previously computed) elastic moduli as the ice-water mixture; the

Kuster- Toksöz equations are again used to calculate the overall moduli. For this second

application of the effective moduli equations, the inclusion phase is quartz and the

inclusion concentration is (1 - Φ). The compressional (P)- and shear (S)-wave

velocities V_p and V_s are

$$V_p = \left(\frac{K + 4G/3}{\rho}\right)^{1/2},$$

$$V_s = \left(\frac{G}{\rho}\right)^{1/2},$$

where K and G are the computed moduli of the three-phase mixture, and the

effective density of the mixture is given by

$$\rho = (1-\phi)\rho_s + s\phi\rho_w + (1-s)\phi\rho_i .$$

(Eq. 2-21)

The model was tested against laboratory data from 23 core samples from the

Canadian Arctic. The data are in many respects consistent with the predictions of the

theory. Zimmerman and King conclude that this theory can be used to infer the water/ice

ratio of unconsolidated permafrost, based on knowledge of either of the seismic wave

speeds.

2) Leclaire et al's three-phase model

Leclaire, Cohen-Ténoudji and Aguirre-Puente (1994) proposed a comprehensive

three-phase theory based on Biot's theory. This model assumes that there is no direct

contact between solid grains and ice, since, in principle, water tends to form a thin film

around the grains (Figure 2-2). The theory developed by Leclaire et al. (1994) explicitly

takes into account the presence of the three phases. The theory predicts three

compressional waves and two shear waves and can be applied to unconsolidated and consolidated media. Leclaire et al. (1994, 1995) also provide a thermodynamic relationship between the proportion of unfrozen water and temperature.
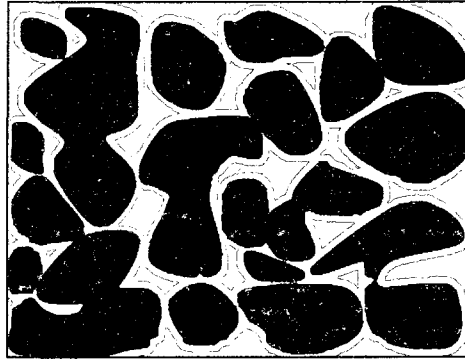
Figure 2-2. Interpenetrating solid (dark) and ice (light grey) matrices with unfrozen water film (white)

The theoretical detail and modeling procedures of Leclaire et al's three-phase model are given in Appendix B.

The equation of motion in Leclaire et al's theory is as follows:

$$\overline{R}.grad.div.\overline{u} - \overline{\mu}.curl.curl.\overline{u} = \overline{\overline{\rho}}\ddot{u} + \overline{\overline{A}}\dot{u}$$

where $\overline{u}$ is the local displacement matrix, $\dot{u}$ is the velocities matrix, and $\ddot{u}$ is the acceleration matrix.

The matrices of mass densities and friction coefficients are given by

$$\overline{\rho} = \begin{pmatrix} \rho_{11} & \rho_{12} & 0 \\ \rho_{21} & \rho_{22} & \rho_{23} \\ 0 & \rho_{32} & \rho_{33} \end{pmatrix} \text{ and } \overline{A} = \begin{pmatrix} b_{11} & -b_{11} & 0 \\ -b_{11} & b_{11}+b_{33} & -b_{33} \\ 0 & -b_{33} & b_{33} \end{pmatrix}$$

Matrices of bulk and shear stiffness moduli are

$$\overline{R} = \begin{pmatrix} R_{11} & R_{12} & 0 \\ R_{21} & R_{22} & R_{23} \\ 0 & R_{32} & R_{33} \end{pmatrix} \quad \text{and} \quad \overline{\mu} = \begin{pmatrix} \mu_{11} & 0 & 0 \\ 0 & 0 & 0 \\ 0 & 0 & \mu_{33} \end{pmatrix}$$

whose elements are given by

$$R_{11} = K_1 + \frac{4}{3}\mu_1, \quad R_{12} = R_{21} = C_{12}, \quad R_{22} = K_2$$

$$R_{23} = R_{32} = C_{23}, \quad R_{33} = K_3 + \frac{4}{3}\mu_3$$

$$\mu_{11} = \mu_1, \quad \mu_{33} = \mu_3$$

The three compressional velocities of the three-phase frozen porous medium are given by

$$V_{Pi} = [\text{Re}(\sqrt{\Lambda_i})]^{-1}, \quad i = 1,2.......,3 \tag{Eq. 2-22}$$

where Re denotes the real part and Λ_i are obtained from the following characteristic equation:

$$A\Lambda^3 - [\rho_{11}B + \rho_{22}C + \rho_{33}D - 2(R_{11}R_{22}\rho_{23} + R_{33}R_{12}\rho_{12})]\Lambda^2$$
$$+ [bR_{11} + cR_{22} + dR_{33} - 2(\rho_{11}\rho_{23}R_{23} + \rho_{33}\rho_{12}R_{12})]\Lambda - a = 0 \tag{Eq. 2-23}$$

The velocities of the two shear waves are given by

$$V_{Si} = [\text{Re}(\sqrt{\Omega_i})]^{-1}, \quad i = 1,2, \tag{Eq. 2-24}$$

where Ω_i are obtained from the second-order equation

$$\Omega^2 \rho_{22} \mu_1 \mu_3 - \Omega(\mu_1 b + \mu_3 d) + a = 0 \qquad \text{(Eq. 2-25)}$$

The coefficients in (2-23) and (2-25) are given in Appendix B.

Leclaire et al. (1994) proposed that the Unfrozen Water Content (UWC) in frozen soil can be obtained based on Thomson's formula:

$$Ln\frac{T}{T_0} = -\frac{2\sigma_{iw}}{r}\frac{1}{\rho_i L_w}$$

Assuming a Gaussian porosimetric distribution, the volumetric unfrozen water proportion ϕ_w can be obtained as a function of temperature as

$$\phi_w = (1-\phi_s)\Delta r^{-1}(2\pi)^{-1/2}\int_{-\infty}^{r_0/\ln(T_0/T)} \exp[-(r-r_{av})^2/(2\Delta r^2)]dr \qquad \text{(Eq. 2-26)}$$

where $r_0 = 2.28\times10^{-10}$ m, r_{av} is the average pore radius and Δ_r is the standard deviation (Leclaire et al. 1994). The temperature T is given in degrees Kelvin and $T_0 = 273°K$

Carcione and Seriani (1998) applied Leclaire et al's theory with some minor modifications to modeling the acoustic properties of permafrost and gas hydrates.

2.3. Ultrasonic tomography

Tomography is an application of nondestructive methods to view the interior of a body without penetrating its surface by physical means. In tomography, radiation is either passed through a material or reflected inside a material along a straight path. The radiation carries information about the physical properties in the medium (Terada and Yanagidani, 1986). This process is repeated with different locations of transmitting and

receiving radiation to achieve the desired resolution. This method of imaging is used widely in the medical field using X-ray CT scan to create a cross-sectional image. The data are then inverted using a transformation algorithm. Tomography inversion techniques are derived from the Radon Transform. The transform is named after Radon (1917), who first derived an inversion transformation. The Radon Transform is described in depth by Nolet (1987).

The focus of this study is on geophysical applications of tomography. Radiated energy is passed through a medium and measured in slightly different ways, producing transforms that display different physical information in the cross-section. Geophysical tomography can utilize different radiation sources such as X-ray, electrical resistivity, seismic, and ultrasonic. This area of study was pioneered by Dines and Lytle (1979). During the last few decades, numerous tomography techniques were developed based on the propagation of various signals like X-rays (Jacobs et al., 1995), magnetic resonance (Amin et al., 1998), electric resistivity (Binley et al., 1997; Zhou et al., 2001), and acoustic waves (Bording et al., 1987; Michelena and Harris, 1991; Dietrich et al., 1995).

In X-ray tomography the cross-sectional image is of the boundaries within a medium such as cracks in rock. In electrical resistivity tomography, the tomograph shows the resistivity through the medium (Daily and Owen, 1990; Jacobs et al., 1995). Reflection tomography measures reflected ultrasonic waves as they bounce off interfaces within a body. This method can be used to locate geologic structures or old mine workings (Hanson et al., 2002). Seismic tomography is very similar to ultrasonic tomography. The difference between these two methods of tomographic imaging is the frequency ranges

used. Seismic tomography utilizes low-frequency waves to measure structures within the earth. The low frequencies correspond to long wavelengths, which are capable of traveling long distances. Ultrasonic tomography is used more frequently for laboratory and field monitoring systems. Ultrasonic waves have shorter wavelengths which can resolve finer structures; however, ultrasonic waves attenuate quickly and can therefore only be transmitted over short distances. Ultrasonic tomography can be used to measure the slowness of the P or S wave across the sample as well as amplitude variations across the sample.

A tomographic survey which is conducted at a density or stress state within the acoustic-elastic region will show a cross-sectional picture of the relative internal density or stress. To observe this, the velocity within the material is first found by collecting an ultrasonic waveform by transmitting an ultrasonic wave through the material, and the arrival time of the wave is found. There are different methods of automatically finding the arrival time of the waveform. In seismology, automatic picking of the first break is very important and many studies have been done to make this process more robust. The main difference between laboratory applications of arrival time picking and seismic applications is the difference in the signal to noise ratio (SNR). The SNR for laboratory testing normally is very high; this is not the case for seismic testing. Therefore, the algorithms used for arrival time picking are complex for seismic data to account for the poor SNR.

The direct correlation method of arrival time picking is used in the laboratory and in the field. This method uses statistics to determine the arrival time of the waveform. It is a

simple method in which a portion of a waveform is compared to a reference waveform and the correlation between the two plots is compared. A high correlation indicates a high probability that the sections of the waveforms are the same. This method of arrival time picking is explored in depth by Molyneux and Schmitt (1999). Once the arrival time is picked, the velocity of the wave can be calculated. The velocity between one source and receiver pair represents an average velocity along that ray path. By conducting a tomographic survey where multiple ray-paths are measured at different orientations across the sample, many velocities along the different ray paths can be found. These velocities are then inverted to produce a velocity profile along the plane being measured.

The algorithms used for ultrasonic tomography have improved since the first application of geophysical tomography by Dines and Lytle (1979). Two common algorithms used for tomographic inversion are the algebraic reconstructive technique (ART) and the simultaneous iterative reconstructive technique (SIRT). The ART method is used for linear models. This method inverts all of the data at once to form a tomographic representation of the data. This method is simpler than the SIRT method; however, if a large data set is used it requires large amounts of computer memory and processing time to conduct the transformation. The SIRT method iteratively inverts rows of data that improve the initial inversion. The iterations continue until all data have been processed. This method is useful for large data sets because the amount of computer memory required is significantly less than the amount required when using the ART method. A comprehensive review of both methods is found in the literature (Nolet, 1987; and Trampert and Leveque, 1990).

Tomography has been used widely for geophysical applications such as earthquake tomography, three-dimensional structural imaging, geologic hazard identification, and stress identification. For large structures, seismic tomography is commonly used because seismic waves can travel longer distances than ultrasonic waves. The theory behind seismic tomography is comparable to that of ultrasonic tomography. Field studies using seismic tomography have been conducted in mines to characterize underground rock masses (Song et al., 1998) and map underground structures (Marti and Carbonell, 2002; Blaha, 2002). Tomography has also been used in mining to monitor for roof or pillar failure, to identify regions of relatively higher stress, and for strata identification. The use of these mine-wide monitoring systems can increase miner safety and also help maintain production by preventing potential roof failure. Hazard detection is one way in which ultrasonic tomography can increase miner safety. In active mining sections, structural analysis can be done by observing the roof, rib, and floor surfaces. Further geologic characterization and hazard recognition efforts are not undertaken due to cost constraints (Hanson et al., 2002). If a further geologic characterization is undertaken, it usually requires boreholes to be drilled from the surface to intersect the ore deposit. To reduce characterization costs, ultrasonic tomography can be employed to detect hazards ahead of mining or within the mine workings. Some hazards that can be detected are old mine workings, structural changes in geology, and high-stress zones (Hanson et al., 2002). To detect old mine workings, reflection tomography can be employed. Structural changes in geology are detected by measuring anisotropy (Song et al., 1998), high-resolution 3D tomography (Marti and Carbonell, 2002), or by noting velocity characteristic changes

across a rock mass (Blaha, 2002; Seebold et al., 1999). Using these methods, faults, strata

changes, and in some cases water content can be defined within a rock mass. This

information is very valuable in mine planning. High stress detection is also an important

application of ultrasonic tomography. Field studies have been conducted successfully

while excavating tunnels (Falls and Young, 1998), excavating longwall panels (Friedel et

al., 1996), identifying burst-prone faces (Semandeni and Calder, 1990), and measuring

mining induced geological changes (Cheng et al., 2001). Coupling tomography with

other imaging techniques such as ground- penetrating radar (GPR) can give an indication

of where surfaces are located, in addition to measuring the stress at these interfaces

(Dérobert and Abraham, 2000). Another application combines acoustic emission

detection with ultrasonic tomography to monitor faulting or failure (Itakura et al., 1995)].

This testing method has been used in mines but is mainly being studied on the laboratory

scale. An overview of other engineering applications and equipment design for ultrasonic

investigations can be found in the literature (Malinský, 1996; Plocek, 1996; Goulty, 1993;

Scott et al., 1999).

Ultrasonic tomography has been conducted in the laboratory to better understand the

implications of this monitoring method. By analyzing sample behavior in the laboratory,

many experiments with different loading conditions and sample characteristics can be

conducted readily. The design of a tomographic data acquisition system for the laboratory

would be advantageous to allow these experiments to be conducted. Laboratory

tomographic systems have been developed in past experiments (Terada and Yanagidani,

1986; Couvreur et al., 2001). These systems were not designed to accommodate new

technologies such as faster acquisition computers and higher resolution A/D converters. Experiments that have been conducted involve the stress distribution from indentation (Scott et al, 1994), as well as stress distribution and acoustic emission location in hydraulically loaded samples (Falls et al., 1992; Villaescusa et al., 2002).

Radon's (1917) transformation of line integrals provides the basic mathematics of tomography applied to straight rays. It defines a two-dimensional function f(x, y) through the line projections integrated over all angles. However, if considerable heterogeneity exits in the internal structure, such as in geological formations or soils, the assumptions of wave propagation along straight lines is no longer valid because of signal diffraction. To remedy this problem, computer codes have been developed that account for wave diffraction. Worthington (1984) and Phillips and Fehler (1991) summarized the most common strategies of ray path tomography. They distinguished among matrix inversion (Aki and Richards, 1980), Fourier transform methods (Merserau and Oppenheimer, 1974), convolutional or filtered back-projection methods (Robinson, 1982), and iterative methods (Gilbert, 1972; Dines and Lytle, 1979; Krajewski et al., 1989).

Berkenhagen et al. (1998) and Flammer et al. (2001) successfully applied acoustic waves to soil moisture variations. They found that the velocity of an acoustic wave is related to the elasticity modulus and the total density of the medium. According to Brutsaert (1964), the impact of the elasticity modulus on the acoustic velocity exceeds the soil density influence. Brutsaert (1964) also provided a relationship between acoustic velocities and water content.

This study involves ultrasonic P-wave velocity tomography of freezing soil. This type of tomography produces a series of cross-sectional images of velocity across a soil specimen during the freezing process.

2.4. Testing of freezing soil physical properties using ultrasonic techniques

The propagation of sound waves in materials is due to the vibrations or oscillatory motion of particles within materials, so acoustic properties of materials are important factors reflecting their constituents and physical structure (Rose, 1999). As one of the most effective nondestructive methods, the ultrasonic technique has been applied in many inspection fields such as materials analysis, medical and biological applications, underwater measurements, ultrasonic flaw detection, and so on. At the same time, ultrasonic techniques have been used in the area of minerals, rock, sand and unfreezing soil (Rose, 1999; Song et al., 2004; Abo-Qudais, 2005; Bucur, 2005). Recently, there has been considerable interest in the properties of freezing soil as its increasing importance becomes more widely recognized.

Generally speaking, the mechanism of ultrasonic detection is to distinguish the physical properties of the detected material through analyzing the propagating features of ultrasonic waves in the material. The higher the frequency of the ultrasonic wave, the better the resolution of detection because only more than 1/4 wavelength of a "spot" inspected can result in a distinct response to the wave propagation. This is why the ultrasonic wave is often chosen as a detecting tool. The selection of detection frequency is subject to the properties of the materials and the detection purpose. Since the 1970's,

researchers have been trying to apply ultrasonic technology to freezing soils. The studies

were mainly focused on the understanding of the propagating characteristics of ultrasonic

waves in freezing soils. The results revealed that the ultrasonic velocities changed little

with temperature in sand (Nakano et al., 1972; Nakano and Arnold, 1973), but decreased

with increasing temperature in frozen silt (Inoue and Kinoshita, 1975; Fukuda, 1991)

They also indicated that the unfrozen water content might be an important factor

affecting ultrasonic velocity in freezing soil (Fukuda, 1991; Thimus et al., 1991).

A summary of the dilatational wave velocity data obtained in permafrost regions for

over twenty-five years was compiled by Barnes (1963). Timur (1968) measured the

dilatational waves in rocks between 26 and -30 C by the pulse first arrival technique, in

which the time required for an elastic wave to traverse a sample of known length is

determined. He concluded that the dilatational wave velocity in water-saturated rocks

increases with decreasing temperature, whereas it is nearly independent of temperature in

dry rocks. The shapes of the velocity-versus-temperature curves are functions of

lithology, pore structure, and the nature of the interstitial fluids. Banthia et al. (1965)

employed the methods reported by King and Fatt (1962) to determine shear-wave

velocity for four dry sedimentary rocks as a function of the variation of both external

hydrostatic pressure and internal pore pressure in the range 0 to 2500 psi. Nakano et al.

(1972) measured ultrasonic velocities of dilatational and shear waves in water-saturated

freezing soils as a function of temperature by using both pulse first-arrival and critical

angle methods. They found that a strong correlation exists between dilatational wave

velocities and unfrozen water content. The observed hysteresis in the velocities of silt and

clay during a freeze-thaw cycle is considered to be caused by hysteresis in the frozen water content. They also found that in the frozen state there is a general tendency for the shear wave velocity to decrease with ascending temperature, but the effect of temperature is not as pronounced as that on the dilatational velocities. Subsequently, Nakano and Arnold (1973) measured the ultrasonic velocities of dilatational and shear waves as well as damping of dilatational waves in frozen Ottawa sand as a function of water content by using the critical angle method at a frequency of 1 MHz. They found that the dilatational velocity in frozen sand varies with increasing water content from about 0.35 to 4.6 km/s, and the shear velocity increases monotonically with increasing water content. Thimus et al. (1991) compared the unfrozen water content obtained by ultrasonic wave velocity with the results measured by other methods such as Gilpin theory, nuclear magnetic resonance, and differential calorimetry. Sheng et al. (2000a) measured the ultrasonic velocities of both dilatational and shear waves in tire-pieces mixed Tomakomai silt (in Hokkaido, Japan) within the temperature range of -0.2 to - 10 °C by the immersion sing-around method and discussed the relationships between ultrasonic velocities and unfrozen water content. But there have been few papers about applying ultrasonic technology to measuring mechanical characteristic of freezing soils.

Sheng et al. (2000a) studied the relationship between unfrozen water content and ultrasonic velocities in frozen Tomakomai silt and proposed a linear relationship (Sheng and Fukuda, 1998; Sheng et al., 2000a). The propagating features of ultrasonic waves in freezing soil reflect the dynamic properties of freezing soils, and the dynamic properties depend on the physical properties. Therefore, the physical index of freezing soils should

determine their ultrasonic propagating characteristics. In other words, measuring ultrasonic velocities in freezing soils may help us to understand the physical properties of freezing soils. Although we cannot establish a mechanistic model of the propagation of ultrasonic waves in freezing soils (because freezing soil is a multiphase material, and each component depends on the others during the mechanical vibration, which makes the micro-vibration in freezing soil complicated), considering freezing soil as a macro-uniform material, it is possible to find some empirical relationships between ultrasonic velocities and macro-physical properties such as strength or unfrozen water content.

Wang et al. (2006) summarized that ultrasonic wave velocities and dynamic mechanical parameters of freezing soils depend on freezing temperature and soil types. In general, ultrasonic wave velocities and dynamic modulus decrease with increasing temperature and increase as soil grains become coarse, while dynamic Poisson's ratio increases with increasing temperature decreases as soil grains become coarse.

The variation of ultrasonic wave velocities and dynamic parameters of freezing soils with freezing temperature is due to the variation of unfrozen water content with the freezing temperature fluctuation. The effect of soil grain size on the ultrasonic wave velocities and dynamic parameters is considered to be caused by different unfrozen water content in different freezing soil types under the same freezing temperature.

The relationship between dynamic elastic modulus and shear modulus of tested soils and freezing temperatures can be described by a simple logarithmic function with high correlation (R^2 values).

Since the acoustic properties of materials can reflect their constituents and physical structure, we can study freezing soil's physical-mechanical properties by observing the speed of ultrasonic waves propagating through the freezing soils. At the same time, investigations of the relation between the acoustic properties of well-defined freezing soils and their constituents under variable physical conditions can promote further understanding of frozen ground.

The velocity of ultrasonic waves traveling in a medium reflects the dynamic properties of that medium, which depend on the physical properties. Taking advantage of the ease of operation and non-destructive nature of ultrasonic technology, it is possible to determine some physical properties of freezing soils by using this technique, either in the laboratory or in the field. In the present study, a series of experiments were carried out to obtain dynamic properties of freezing soils and to establish relationships between ultrasonic velocities and unfrozen water contents, as well as the strength of freezing soil. Experimental results indicated that the strength of freezing soil can be estimated as a function of a single factor by measuring ultrasonic velocities. Additionally, ultrasonic velocities can be used to predict the unfrozen water content of freezing soil at different temperatures.

2.4.1. Direct determination of dynamic parameters of freezing soils

Dynamic properties of freezing soils are important to geophysical exploration, excavation by blasting, and design involving vibrating machinery. Sonic propagation in freezing soils can be used to determine dynamic properties of freezing soils (Young's

modulus, shear modulus and Poisson's ratio). Elastic parameters should be expressed as follows as functions of ultrasonic velocities (Bourbie et al., 1987):

$$E = \frac{\rho V_s^2 (3V_p^2 - 4V_s^2)}{V_p^2 - V_s^2}$$

$$G = \rho V_s^2$$

$$\mu = \frac{V_p^2 - 2V_s^2)}{2(V_p^2 - V_s^2)}$$

Here, E is Young's modulus, Pa; G is shear modulus, Pa; μ is Poisson's ratio; ρ is density in kg/m³. V_p refers to longitudinal wave velocity in m/s: V_s refers to shear wave velocity in m/s. Given the density of freezing soil, we can calculate elastic constants from the above equations by measuring the ultrasonic velocities of waves in freezing soil.

Sheng et al. (2003) showed that the ultrasonic velocities of both longitudinal and shear waves decrease with increasing temperature and that Young's modulus and shear modulus also decreased with increasing temperature. These results show the same trends as the experimental results obtained from a uniaxial strength test (He et al., 1993). The modulus obtained by the ultrasonic method is an order of magnitude higher than the results from a materials test machine. Considering the higher frequency and the lower strain in the ultrasonic method, the higher modulus is understandable. It is not an easy job to determine Poisson's ratio of soil with a common test machine. However, it is relatively straightforward to obtain Poisson's ratio for freezing soils by using ultrasonic technology.

Compared with normal elastic materials, Poisson's ratio of freezing soil is somewhat

lower, and it increases with increasing temperature (Sheng et al., 2003).

2.4.2. Uniaxial compressive strength and ultrasonic velocities in freezing soils

Theoretically, ultrasonic velocities should not directly reflect the strength

characteristics of freezing soils. However, when a factor affecting the strength of freezing

soil changes, the ultrasonic velocity in that freezing soil also changes. If there is a good

relationship between the uniaxial strength and ultrasonic velocities, it should be possible

to estimate the uniaxial strength of freezing soils by measuring the ultrasonic velocities of

waves through freezing soils. Inoue and Kinoshita (1975) conducted experiments on

ultrasonic velocity and strength for frozen silt and sand with different water content at a

constant temperature. Their results indicated that there is a linear relationship between

uniaxial compressive strength and shear velocity.

Sheng et al. conducted series of tests of uniaxial strength for different temperatures

in frozen Lanzhou Loess (Sheng et al., 2003). They found that the strength of freezing

soil can be expressed as a power function of the longitudinal velocity of ultrasonic waves

when changing temperature of freezing soil (longitudinal velocity varies with

temperature). The lower the temperature of freezing soil, the faster the ultrasonic longi-

tudinal velocity and the higher the strength of freezing soil. This relationship between

strength and wave velocity in freezing soil makes it possible to estimate the strength of

freezing soil by ultrasonic measurement on only one sample after conducting a few

strength tests to calibrate the relationship.

Another experiment was carried out by Sheng et al. (2000a) for Tomakomai silt mixed with tire powder (from discarded rubber tires) at different mixing fractions at the same temperature (-5°C). They found that the compressive strength of frozen Tomakomai silt has a linear relationship to longitudinal velocity, as in the mix with the tire powder fraction (Sheng et al., 2000a, b).

2.4.3. Unfrozen water content and ultrasonic velocity

Unfrozen water content is one of the most important factors affecting the physical and mechanical properties of freezing soils. Understanding the relationship between unfrozen water content and ultrasonic velocities makes it possible to use ultrasonic wave velocities to determine unfrozen water content (Fukuda, 1991). Because the change in unfrozen water content indicates a change in ice content, which plays a cementing role in freezing soils, the change of ice content must result in the change in mechanical properties of freezing soils. Sheng et al. have conducted ultrasonic experiments on Tomakornai silt to study the effect of unfrozen water content on the ultrasonic velocities (Sheng and Fukuda, 1998; Sheng et al., 2000a). Their results showed a linear relationship between unfrozen water content and both longitudinal and shear waves velocities.

After experimental study on glass beads, with diameters ranging from 2.2 to 10 μm, Sheng et al. concluded that a power function exists between unfrozen water content and the longitudinal velocity. The unfrozen water content of freezing soil strongly affects the ultrasonic velocity. The higher the unfrozen water content, the lower the ultrasonic velocity. The existing power function is different from the linear function that was found for

frozen Tomakomai silt by Fukuda (1991) and Sheng and Fukuda (1998). This may be a result of the difference in the nature of the materials. Empirically, the good correlation between unfrozen water content and ultrasonic velocity suggests that it is possible to measure unfrozen water content by ultrasonic techniques.

In conclusion, the propagation of ultrasonic waves in freezing soils responds to the dynamic properties of the materials. Taking advantage of the simple, fast, non-destructive nature of ultrasonic technology, elastic parameters can be measured directly. Compressive strength also shows a good relationship to ultrasonic velocity. Unfrozen water content obviously affects the ultrasonic velocity, and a good empirical relationship exists between unfrozen water content and ultrasonic velocity. It is obvious that many factors, such as ice content, grain size, temperature, and structure of the soil, may have effects on the ultrasonic velocity and physical properties. The relationships between ultrasonic velocity and the physical and mechanical properties of frozen soil make the estimation of uniaxial strength and unfrozen water content possible.

Chapter 3. Research Methodology

This chapter contains a detailed description of all laboratory and numerical methods and procedures used in this research. Section 3.1 describes experimental methods and procedures, including sample preparation, unfrozen water content measurement, acoustic velocity measurement and computerized ultrasonic tomography (CUST). The configuration and programming of Multi-channel Ultrasonic Scanning System (MUSS) are also introduced in this section. Section 3.2 describes numerical methods and procedures, including temperature-velocity modeling and FEM simulation procedures.

3.1. Experimental methods and procedures

3.1.1. Samples for laboratory tests

Eleven samples were prepared for freezing process observation (Table 3-1). Four reconstituted sand samples with different grain size were prepared for investigation of the grain size effect on ultrasonic wave velocity in freezing sand. Four sand-clay mixtures with different clay content were used to study the effect of fines (clay) content on the variation of wave velocities in the freezing process. Three Fairbanks silt samples with the same physical properties were used to perform dynamic ultrasonic velocity-temperature tests, including both inward and outward freezing processes with CUST scanning (See Table 3-1).

Table 3-1. Samples for laboratory testing

Sample Type	Sample Number	Test Type	
Reconstituted Sand	RS80	P & S_wave velocity test	
	RS140	P & S_wave velocity test	
	RS200	P & S_wave velocity test	
	RS325	P & S_wave velocity test	UWC test
Sand-clay Mixture	SC10	P & S_wave velocity test	
	SC20	P & S_wave velocity test	
	SC30	P & S_wave velocity test	
	SC40	P & S_wave velocity test	
Fairbanks Silt	FS01	P & S_wave velocity test	UWC test
	FS_IW	CUST (Inward freezing process)	
	FS_OW	CUST (Outward freezing process)	

1) Fairbanks silt

The Fairbanks area is covered with silty aeolian loess deposits. The loess sedimentary record in the Fairbanks area indicates that deposition began in the Pliocene Epoch and continued through the Pleistocene. Some minor loess deposition continues today when strong winds travel over the Alaska Range and transport glacial outwash material to the north. The Tanana River, immediately to the south of the Fairbanks area, provides a local source of loess. The thickness of the loess varies, depending on location. As it is easily eroded, loess often is less than one meter thick on the crests of hills where it typically overlies bedrock. In valley bottoms, transported and reworked loess deposits range from 3 to 90 m thick (Darrow, 2007).

The Fairbanks silt sample for this study was collected from a chilled pipeline experiment site, near 3.8 km of Chena Hot Springs Road in the Fairbanks. This research facility is operated and funded by the Japan Science and Technology Corporation (JST) in cooperation with the University of Alaska Fairbanks. The depth of soil sampling was 0.9-1.2 m. The natural soil consists of brown silt with few rootlets.

2) Reconstituted sand

The reconstituted sand samples for this study were Fairbanks sand and silt collected on the bank of the Tanana River near Fairbanks, Alaska. The samples were collected using 60#, 80#, 140#, 200#, 325# sieves. Thus, four grain size samples were obtained (Table 3-2).

Table 3-2. Reconstituted samples of Fairbanks sand and silt

Specimen	Sieves	D10 particle size (μm)	Specific Gravity	Porosity
RS80	60-80#	184	2.632	0.443
RS140	80-140#	112	2.660	0.464
RS200	140-200#	77	2.670	0.473
RS325	200-325#	47	2.717	0.491

3) Artificial sand-clay mixture

For studying wave propagation in frozen sand-clay mixture soils, four artificial fully saturated Fairbanks sand with various clay content (10%, 20%, 30%, and 40%) samples

were prepared (Table 3-3). The sand in the mixture was reconstituted sand RS325, and the clays were separated from Copper River soil using the hydraulic method. The oven-dried sands and clays were weighed and were well mixed with 20% of gravimetric water content.

Table 3-3. Samples of artificial sand-clay mixtures

Sample	Proportion of Sand and Clay		D10 Grain size(μm)	Porosity
	Sand(RS325)	Clay		
SC10	0.9	0.1	1.5	0.50
SC20	0.8	0.2	1.2	0.51
SC30	0.7	0.3	0.9	0.52
SC40	0.6	0.4	0.5	0.53

3.1.2.   Sample preparation

1) Soil particle size analysis of soil

A soil particle size distribution (PSD) test was carried out following ASTM D2487-1969 (1970).

- Sieve analysis

The soil samples were oven dried, crushed and ground into soil powder. The PSD curve for a coarser portion, whose particle size was greater than 0.063 mm, was obtained by sieving the sample through a stack of ordered sieves. Sieving was carried out in the same way on samples of the same totally dry mass for an identical amount of time by

means of a mechanical shaker. By weighing the mass of soil collected from each sieving and expressing that mass as a percentage of the total, the PSD curve was constructed.

- Hydrometer analysis

The PSD curve for fine-portion particles (< 0.063 mm) was determined by sedimentation tests. The soil sample containing an assortment of fine particles was shaken up in water to form a fully dispersed suspension and left to settle out. Samples of the suspension then were taken by pipette from a fixed depth at various times after the beginning of sedimentation. After the water had evaporated, the mass of the remaining solids allowed the proportion of particles having an equivalent diameter within the original sample to be calculated. The PSD curve was constructed in the same way as by sieve analysis. Figure 3-1 shows the PSD curve of Fairbanks silt (FS01).
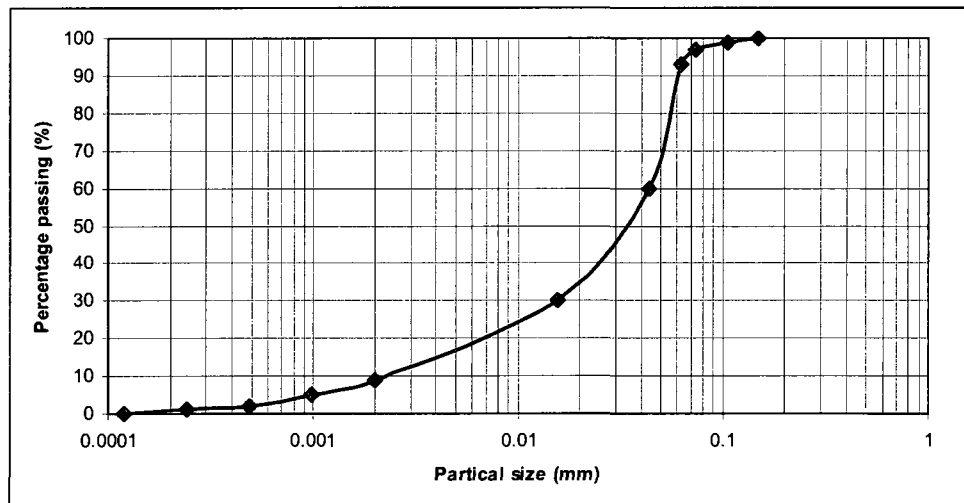
Figure 3-1. PSD curve of Fairbanks silt sample (FS01)

- Effective grain size

The effective grain size, D10, was used in modeling the function of temperature-velocity of freezing soil in this study. D10 is defined as the maximum grain size of the smallest 10% of the sample.

2) Basic properties of remolded Fairbanks silt

The oven-dried soil mixed with 20% distilled water, following the original Proctor test standard, ASTM D698, calls for compaction of three separate layers of soil using 25 blows by a 5.5 lb hammer falling 12 inches. The resultant basic properties of FS01 are shown in Table 3-4.

Table 3-4. Properties of Fairbanks silt (FS01)

	Fairbanks silt
Specific gravity (g/cm³)	2.70
Dry density (g/cm³)	1.54
Bulk density (g/cm³)	1.85
Gravimetric water content	0.2
Volumetric water content	0.37

3.1.3. Unfrozen water content (UWC) measurement

Two of the soil moisture measurement technologies used in the scientific community are Frequency Domain Reflectometry (FDR) and Time Domain Transmissometry (TDT). Both of these types of sensors measure a parameter that depends on the relative dielectric

permittivity of the materials in which they are embedded. FDR methods of moisture

measurement are also known as radio frequency (RF) capacitance techniques.

The UWC is measured using the FDR sensor (Hydra Vitel Probe soil water sensor,

50MHz). The Hydra Probe differs from most other alternative sensors in that outputs

from the sensor include bulk soil electrical conductivity and temperature (measured with

a thermistor), in addition to a reference temperature at 0°C. The Hydra Probe is better

described as a soil dielectric sensor than a capacitance sensor because it measures both

components of the complex dielectric constant.

The Hydra Probe is currently in wide use (e.g., the Soil Climate Analysis Network of

the Natural Resource Conservation Service) and is under active consideration for use in

other soil water monitoring programs. It has proven to be robust under a variety of field

conditions (Seyfried and Murdock, 2002).

The dielectric constant of a material is, in general, complex and proportional to the

electrical permittivity of the material and the permittivity of free space:

$$K_d = \varepsilon_r + i\varepsilon_i$$

where K_d is the dimensionless complex dielectric constant, ε_r is the real

component of the complex dielectric constant, ε_i is the imaginary component of the

complex dielectric constant, and $i = (-1)^{1/2}$. The Hydra Probe measures both ε_r and ε_i.

The Hydra Probe design is based on the work of Campbell (Campbell, 1988 and

1990), who described its theory of operation. The instrument consists of a 4-cm-diameter

cylindrical head which has four 0.3-cm-diameter tines which protrude 5.8 cm. These are

arranged such that a centrally located tine is surrounded by the other three tines in an

equilateral triangle with 2.2 cm sides. A 50 MHz signal is generated in the head and

transmitted via planar waveguides to the tines, which constitute a coaxial transmission

line. The impedance of the probe depends on the electronic components and the K of the

material between the tines (e.g., soil). The relationship is

$$Z_p = \cot anh \frac{(\omega L \sqrt{K_d})}{c} i$$

where Z_p is the probe impedance, L is the electric length of the probe, and c is

the speed of light (Campbell, 1990).

When a voltage is applied to the probe, the reflected signal is related to Z_p such

that

$$\frac{Z_p}{Z_c} = \frac{1 - \Gamma}{1 + \Gamma}$$

where Z_c is the characteristic impedance of the coaxial cable and Γ is the

complex ratio of the reflected voltage to the incident voltage. The Hydra Probe uses

measured Γ to determine Z_p, which can, in turn, be used to determine K_d. A

seven-conductor cable transmits analog DC voltages to a programmable Datalogger.

Downloaded voltage data are then used to calculate ε_r, ε_i, and temperature. Calibration

software is supplied by the manufacturer (Vitel Inc., 1994).

The Vitel Hydra Probe is delivered with binary versions of proprietary software. This software calculates soil-water content from 3 sensor output voltages and temperature from the fourth voltage. Software output values include the real and imaginary parts of the soil dielectric constant, the soil conductivity, water content and temperature.

Seyfried and Murdock (2004) and Yoshikawa and Overduin (2005) evaluated the UWC measured in frozen soil using FDR sensors (including the Hydra Vitel Probe) in comparison with NMR and TDR methods. They concluded that FDR probes are capable of assessing unfrozen water content.

3.1.4. Velocity testing

There are three modes of operation in an ultrasonic test system: pulse echo, through transmission, and pitch catch. The through transmission mode is most suitable for measuring wave velocities and attenuations of geomaterials. The experimental setup for a velocity test is illustrated in Fig. 3-2. A polyethylene container with inner dimensions of 10×20×20cm is used to hold testing soil. Two pairs of transducer-size holes on both sides of the container are fitted with P- and S-wave transducer pairs. The container is squeezed into a supporting wooden jacket to prevent the expansion of the container during the freezing process. To prepare the test, a thin plastic paper is placed against the inner wall of the container to prevent moisture loss. Premixed soil with required moisture content is packed in, following the original Proctor test standard, ASTM D698, which calls for compaction of three separate layers of soil using 25 blows by a 5.5 lb hammer falling 12

inches. A copper-constantan thermocouple is then inserted into the center of the sample

to monitor the temperature using a programmable data logger.
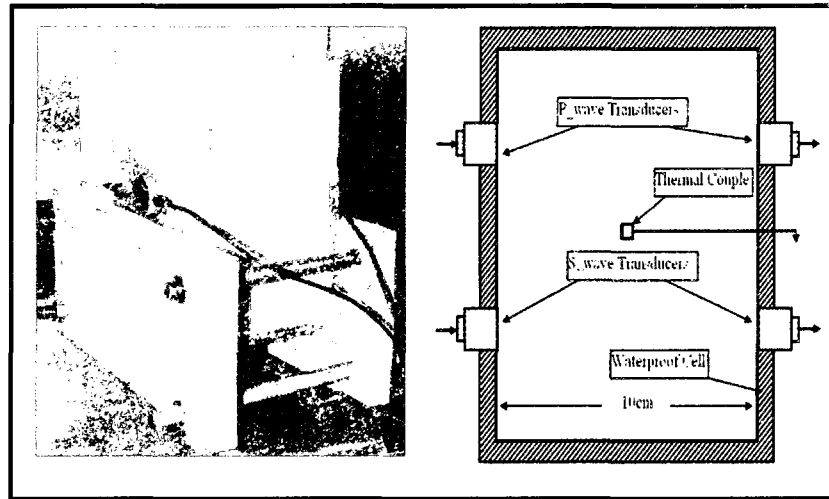
Figure 3-2. Configuration of velocity test cell

The velocities of propagating waves in the sample are measured with the pulse first

arrival technique (Kolsky, 1963). The P-wave piezoelectric transducers (PZT,

specifically, Micro 80 transducers in this study) are pressed against the surface of the

sample with a few drops of Vaseline cream for better coupling, while the S-wave PZT

transducers (Panametric V151-RM) use a special shear-wave couplant. One of the

transducers serves as a transmitter and the other as a receiver. The propagation distance is

10 cm, which can isolate useful signals from unexpected reflection and improve the

precision of the velocity measurement. An ultrasonic pulse originates from a Panametric

5077PR ultrasonic square wave pulser. The transmitter is driven by 300-volt peak pulses

of 1 second duration at a repetition rate of 100-2000 pulses/s, depending on attenuation in

the soil and the time required for ghosts and echoes to die out. The received signal passes

from the sensors into NI PXI 5102 Digital Oscilloscopes with built-in A/D converters which collect analog signals at 20 MS/s. The digitized waveforms are then uploaded to a personal computer for post-processing. The received signal is adjusted to 20-40 db of amplification, band-pass filtered at 300 kHz to 600 kHz, and the first-arrive time is picked from the waveform.

The sample with jacket is placed in a refrigerator in which cold air is circulated by a fan. The inner temperature of the sample is dropped to -30°C by blowing in cold air at -30°C. During a slow reheating over 24 hours in an isolated enclosure, the temperature of the sample is monitored by a thermocouple located in the center of the sample while acoustical measurements are made.

3.1.5. Computerized ultrasonic tomography (CUST)

3.1.5.1. Multi-channel ultrasonic scanning system (MUSS)

The accuracy and precision of a tomographic imaging system are determined by the quality of the acquisition system used. Several factors were taken into consideration before designing the MUSS system. Samples to be analyzed using this system can have a cross sectional area between 20 cm^2 and 100 cm^2. Sensors with smaller diameters should be used to improve the contact between the sensor and the sample. Additionally, the small diameter increases the number of sensors that can be attached to the sample. Selection of the proper couplant is important to increase the signal-to-noise ratio (SNR) of the received signal. A high SNR will increase the accuracy of arrival-time picking. The sensors must be capable of both transmitting and receiving an ultrasonic pulse. The

ultrasonic pulser that is used with this system should have adjustable output frequency and output amplitude. This allows for more precise matching of the resonant frequency of the transmitted signal to that of the sample. Once the signal is received, it is digitized using an analog to digital (A/D) converter. The resolution of this device must be fine enough to resolve the first break of the received waveform to accurately calculate the velocity of the wave. The resolution of the A/D converter is determined by the number of quantization steps (vertical resolution) and also by the acquisition speed (horizontal resolution). All of the devices within the system should be capable of being controlled by the user at one location for the convenience of operation.

Based on the above considerations, a MUSS was designed to be used in this study and was operated in the through-transmission mode. The system was installed and programmed for the sample velocity tomography study in the Rock Mechanics Laboratory in the Department of Mining and Geological Engineering at the University of Alaska Fairbanks. Figure 3-3 shows the schematic of the ultrasonic scanning system. The MUSS is controlled by a personal computer. An ultrasonic pulse originates from a Panametrics 5077PR Ultrasonic Square Wave Pulser. The pulser transmits an ultrasonic frequency that matches that of the material being measured at a repetition rate of 100 to 2000 Hz. This signal is relayed to one sensor on the sample through an NI PXI 2585 Multiplexer. The NI PXI 2585 relays are controlled digitally by the LabVIEW program. The computer multiplexes the pulse through each of the predetermined source locations, switching after the signal has been received by each of the reception sensors. Once the signal is relayed, it enters a transmitter on the sample. This signal is received by the

reception sensors, which are passively waiting for the ultrasonic signal. The received data

pass from the sensors into NI PXI 5102 Digital Oscilloscopes with built-in A/D

converters which collect analog signals at 20 MS/s. The digitized waveforms are then

passed back into the personal computer for post-processing.
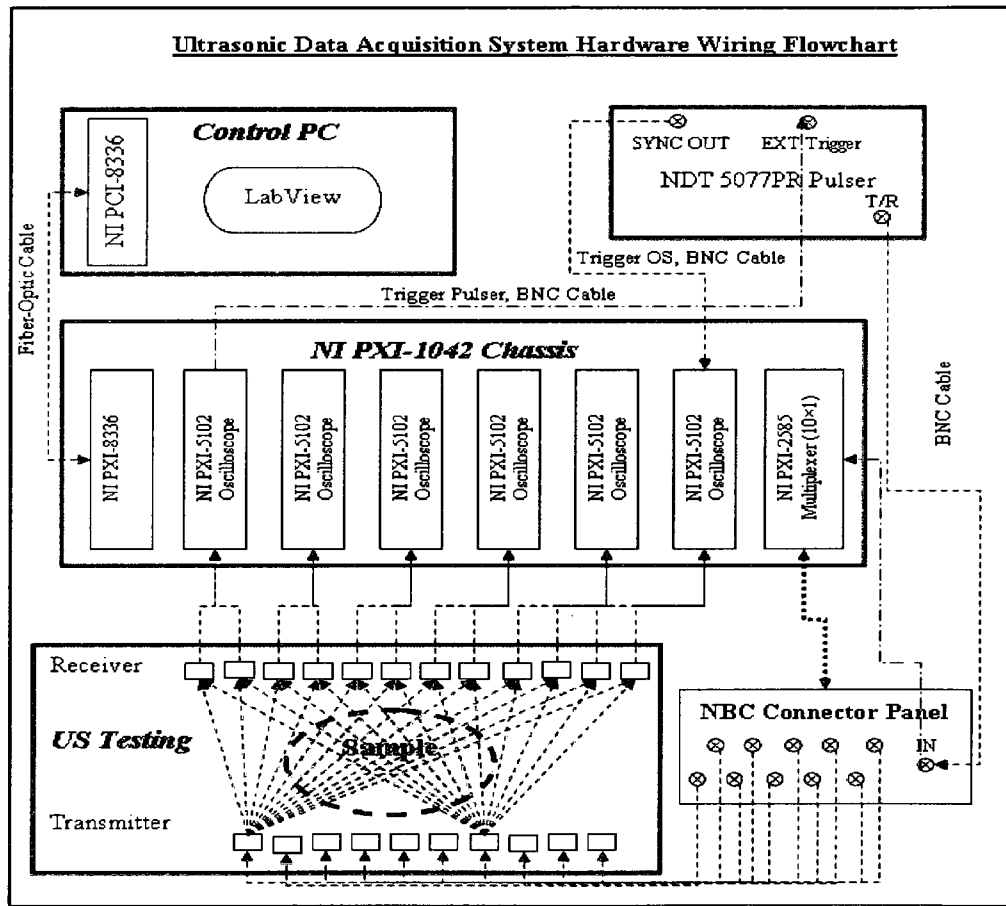
Figure 3-3. MUSS Hardware Wiring Flowchart

The most sensitive components of the ultrasonic data acquisition system are the

sensors. Piezoelectric transducers (PZT) are often used for ultrasonic testing to translate

vibration into an electrical signal. A perfect match between the resonant frequency of the

sensor and the sample would result in the maximum energy transfer of the ultrasonic

signal through the soil specimen. The other consideration at the interface of the sensor and the sample involves acoustic impedance. Acoustic impedance is the opposition to the flow of sound through a material. The effect of acoustic impedance can be minimized by using a couplant that has impedance close to the impedance of the sample. The typical frequency range for ultrasonic testing is 100 kHz to 1 MHz. Based on these criteria, the sensors used in this study are Micro80 miniature P-wave piezoelectric ceramic transducers with a central frequency of 400 kHz. The sensors have a wide bandwidth, allowing for a wide range of frequency matching to different sample types. Their small diameter (10 mm) allows for a reduction in energy loss through the couplant by mounting the flat sensor face to the curved sample surface.

After the waveforms that have been digitized by the PXI 5102 A/D cards, digital signal processing (DSP) of the waveforms is performed in LabVIEW. The processing that needs to be conducted is the automated picking of the first arrival times. This is done by waveform transition measurement (first edge number of wave rise) in LabVIEW. A LabVIEW program is written to filter and magnify waveforms, and then to measure the time of first rise as first-arrive time. This method works well for waveforms with a high signal to noise ratio (SNR). Even so, all of the picks are double checked manually to ensure accurate picking. The accuracy of the picks is very important due to the small scale that is used. Therefore, great care must be exercised to ensure the accurate picks of the first-arrival times.

3.1.5.2. Tomography generation

For this study, tomograms were created in GeoTomCG. This software was

developed by GeoTom, LLC (Apple Valley, MN), for creating tomograms from

geophysical data. This program uses simultaneous iterative reconstruction technique

(SIRT) to perform tomographic inversions. It is assumed that the acoustic velocity varied

in space during the freezing process, resulting in curved ray paths because of wave

diffraction. A modified version of the SIRT code was applied in this study. GeoTom

provides algorithms for both straight and curved rays. According to Krajewski et al.

(1989), the straight-ray assumption is no longer valid if the acoustic velocity, as a result

of heterogeneities, is larger than 1.5 times the uniform acoustic velocity. For this study,

we assumed that the acoustic velocity was randomly distributed. The curved ray

procedure was used whenever the maximum acoustic velocity of a single tomogram

exceeded 1.5 times the minimum acoustic velocity, as determined from the first

tomographic data set using both the straight-ray and the curved-ray algorithm. The

acoustic P-wave velocity range between 500 and 4100 m/s and 600 and 4200 m/s for the

straight-ray and curved-ray computations, respectively. Both cases required application

of the curved-ray procedure, which was subsequently used for all computations.

SIRT requires an initial acoustic velocity model to start the iteration procedure. A

uniform acoustic velocity was assumed for that purpose. In the first iteration, step travel

times were initiated for each ray path on the basis of previous experience. The residuals

between initial and measured travel times were used for fitting the acoustic velocities

along each ray path. The resulting acoustic velocity distribution was used as the initial

model for the second iteration, for which the acoustic velocities were fitted again to the residuals. The iteration procedure was repeated 9 to12 times. This model then underwent an iterative inversion using SIRT. The inverted model was then displayed to show a pixilated cross section of the model. Each pixel represented a point velocity at ray-path intersections. It is important to have at least one intersection for each pixel so that each pixel represents an average velocity.

3.2. Numerical methods and procedures

3.2.1. Modeling the temperature-velocity relationship

For simulating the velocity distribution based on the numerical thermal analysis results (temperature distribution), it is essential that a model be established to describe the temperature-velocity relationship for the specific sample.

Several models of temperature-velocity relationship were introduced in Section 2.2 above. Two of them were investigated in this study, i.e., (1) Zimmerman and King's model, and (2) Leclaire et al's three-phase model. Zimmerman and King's semi-empirical model (1986) has been accepted by many researchers to be used to infer the temperature-velocity relationship of unconsolidated permafrost, while Leclaire et al's three-phase model predicts three compressional waves and two shear waves and can be applied to unconsolidated and consolidated media.

The detailed numerical procedures are described in Section 2.2. The user-oriented programs for each model were created and compiled in Matlab, which allows inputs of

customized parameters (soil properties, moisture content and ambiance condition) and outputs the temperature-velocity curves.

As described in 3.1.1, for investigating the influencing factors of the temperature-velocity relationship, the P- and S-wave velocity tests were conducted on nine samples (reconstituted Fairbanks silts, sand-clay mixtures, and Fairbanks silt) in the laboratory in this study. Numerical modeling studies of temperature-velocity relationships were also performed on these nine samples.

3.2.2. FEM modeling of the freezing process

Frozen soils are porous media which consist of solid particles, water, and ice. Heat transfer in freezing soils is a complex process because of the multi-phase nature of the mixture. The phase change of the liquid part adds complexity since not all water changes phase at the freezing temperature. Difficulties with convergence are known to appear when simulating the process.

Three important effects associated with the freezing process are (1) effect of the latent heat during the phase change of water, (2) nonlinearity of the soil's thermal properties, and (3) the existence of unfrozen water in freezing soil. As soil is subjected to freezing, liquid water inside soil pores turns into ice. However, not all water freezes at the freezing temperature. The amount of unfrozen water drops as the temperature decreases, but some liquid water is still present in freezing soil at temperatures well below 0°C. As a result, the latent heat of fusion of water is released over a range of temperatures rather than at one particular temperature. Release of the latent heat has a

strong influence on the temperature profile of the soil and retards frost penetration. As the freezing front penetrates into soil, thermal properties of the freezing soil also change. The thermal conductivity and the heat capacity of soil vary with the volumetric fractions of phases, which are dependent on temperature.

In this study, the numerical procedure for simulating the transient heat transfer in freezing soils was conducted using the Earth Science module in Comsol Multiphysics. Based on the Conduction in Porous Media method in the Earth Science module, combined with the phase change model and moisture content function of a particular soil, the transient heat transfer of the freezing process of soil can be simulated and analyzed. Simulations of inward and outward two-dimensional freezing patterns in saturated soils are presented in this study to compare with experimental results obtained in the laboratory. The outputs of the simulation are the temperature profile, frost penetration, and ice and water distribution in the soil.

1) Assumptions of transient heat transfer in soils

Some assumptions are made for the transient heat transfer analysis in soils:

(a) The heat transfer takes place by conduction only.

(b) The soil is fully saturated.

(c) The thermal conductivity of soil is isotropic.

(d) The volume change of water upon freezing is neglected.

(e) The frost heaving and water migration associated with the freezing process are neglected.

2) PDE formulation

Fourier's law describes heat transfer by conduction with phase change as follows:

$$C_{eq} \frac{\partial T}{\partial t} - L\rho_i \frac{\partial \theta_i}{\partial t} + \nabla \cdot (-K_{eq} \nabla T) = \sum Q_i \qquad \text{(Eq. 3-1)}$$

In this equation, temperature (T) is the dependent variable. The volumetric heat capacity of the soil mixture, C_{eq} (J/K·m³), describes the potential per volume to store heat and so dictates changes in heat stored with time. The effective thermal conductivity, K_{eq} (W/m·K), characterizes how readily the heat is transmitted. ρ_i is the density of ice [m/L³], θ_i is the volumetric fraction of ice, L is the latent heat of fusion per unit mass of water (approximately 3.33×105 J/kg), Q is a heat source (W/ m³), and ∇ is the gradient operator, where

$$\nabla = \frac{\partial}{\partial x} + \frac{\partial}{\partial y} + \frac{\partial}{\partial z}$$

The first term in Equation 3-1 represents the change in energy storage with respect to time. The second term represents the rate of the latent heat released during the change of water into ice. The third term represents the net energy flow by conduction.

Fourier's law of condition,

$$N = -K_{eq}\nabla T$$

gives the magnitude and direction of the heat flux. The equation states that the flux, N, is proportional to the temperature gradient, and K_{eq} prescribes the temperature gradient needed to achieve a given flux.

After incorporating the latent heat into the heat capacity, Eq. 3-1, can be rewritten as

$$(C_{eq} - L\rho_i \frac{\partial\theta_i}{\partial t})\frac{\partial T}{\partial t} = \nabla(K_{eq}\nabla T)$$

where $C_{eq} - L\rho_i \frac{\partial\theta_i}{\partial t}$ is termed the apparent volumetric heat capacity.

3) Effective thermal properties:

The equation coefficients C_{eq} and K_{eq} are effective properties that describe a representative volume of the solids, liquids and gases in a model to store and transmit heat. The effective properties may change value in space and time and even depending on the results from this equation and others.

As an option, the Earth Science Module automatically defines C_{eq} and K_{eq} with information provided about the volume fraction, θ, density, ρ, specific heat capacity, Cp, and thermal conductivity, K. Data are given for the fluids and solids in a model and how they vary with temperature and reactions. The equations defining C_{eq} and K_{eq} are

$$C_{eq} = \frac{\sum \theta_{Li} \rho_{Li} C_{pLi} + \sum \theta_{Pi} \rho_{Pi} C_{pPi}}{\sum \theta_{Li} + \sum \theta_{Pi}} \quad \text{and}$$

$$K_{eq} = \frac{\sum \theta_{Li} K_{Li} + \sum \theta_{Pi} K_{Pi}}{\sum \theta_{Li} + \sum \theta_{Pi}}$$

where the subscripts "L" and "P" denote liquid and solid properties, respectively. The equations are volume-average based.

4) Subdomain settings

Time-scaling coefficient (δts)

This coefficient is normally 1, but the time scale can be changed from seconds to minutes by setting it to 1/60.

Density (ρ)

This specifies the material's density. This quantity is entered as mass per volume.

Heat capacity (Cp)

The heat capacity C describes the amount of heat energy required to produce a unit temperature change in a unit mass.

Thermal conductivity (k)

The thermal conductivity k describes the relationship between the heat flux vector q and the temperature gradient, as in

$$q = -k\nabla T$$

which is Fourier's law of heat conduction. This quantity is entered as power per length and temperature.

Heat source (Q)

The heat source describes heat generation within the domain. Heating and cooling are expressed by positive and negative values, respectively. The quantity Q is entered as unit power per unit volume (W/m^3 in SI units).

5) Boundary Conditions

The Conduction application mode of the Earth Science Module predefines a number of boundary conditions used in heat transfer modeling. Often the temperature is known, for example, at the ground surface or the core-mantle boundary, which gives the Dirichlet condition

$$T = T_0$$

where the specified temperature, T_0, can be a constant, an expression that depends on time, t, or can hinge on results from another COMSOL Multiphysics application mode.

Often, a model predicts just the temperature change related to a given process or the zero-temperature condition

Any combination of generalized, radiative, and convective fluxes can be specified on the boundary using the condition

$$-n \cdot (-K_{eq} \nabla T) = q_0 + \frac{h}{dA}(T_{\text{inf}} - T) + \frac{C_{const}}{dA}(T_{amb}^4 - T^4)$$

In this equation, n is the normal to the boundary, and dA represents thickness. Here, the generalized flux, q_0, can be an arbitrary expression. The second and third terms on the right side of the flux equation are analogs to, respectively, the convective and radiative source terms for 1D and 2D applications. Dividing by the thickness of the diffusive boundary layer, for example, provides dimensional consistency.

The final predefined boundary conditions represent insulation and symmetry as

$$n \cdot (K_{eq} \nabla T) = 0$$

which specifies zero flux perpendicular to the boundary but allows temperatures to change along its length. This condition specifies where the domain is well insulated, or it reduces model size by taking advantage of symmetry. Intuitively, this equation means that the gradient across the boundary must be zero. For this to be true, the temperature on one side of the boundary must equal the temperature on the other side. Because there is no temperature difference across the boundary, heat cannot transfer across it.

In this study, the scenario of the freezing process in the laboratory test is that the soil sample is placed in a refrigerator where the cold air is circulated. Therefore, in this research, only the convective heat source is considered. Three types of boundary conditions are used in the soil freezing process (Table 3-5).

A wide variety of heat sources and sinks can be represented in a model. The software

provides templates for formulating the convective (Q_c) and radiative (Q_R) terms and

leaves the general heat source (Q_H) entirely to the user's discretion.

Table 3-5. Boundary conditions

Boundary condition	Description
$n \cdot (-K_{eq} \nabla T) = q_0 + h(T_{inf} - T)$	Heat flux
$n \cdot (-K_{eq} \nabla T) = 0$	Insulation or Symmetry
$T = T_0$	Prescribed temperature

The convective heat source, (Q_c), represents heat transfer in proportion to an

external temperature. Typical scenarios include heating and cooling with flowing fluids

such as air, water, or magma, and transfer through an overlying but unmolded layer. The

equation for Q_c reads

$$Q_c = h(T_{inf} - T)$$

In this formulation, T_{inf} is the external temperature and T is the temperature at the

present location. The proportionality term h denotes a heat transfer coefficient, which

depends on material properties, model geometry, and model physics.

6) Basic thermal properties of Fairbanks silt

The values of thermal properties of Fairbanks silt for soil skeleton, water and ice are

listed in Table 3-6. These values are used in the simulations in this study.

The unfrozen water content (UWC) plays an important role in heat transfer in soils. It determines not only how much latent heat is released, but also the effective thermal properties C_{eq} and K_{eq}. A UWC function with the temperature as the only variable is predetermined for specific specimens based on the FDR experimental data, and then a scalar expression of this function is recreated in the Earth Science module of Comsol Multiphysics.

Table 3-6. Thermal properties of Fairbanks silt

	Density $\rho(kg/m^3)$	Specific heat capacity $C_p(J/kg^\circ C)$	Thermal conductivity $k(W/m^\circ C)$
Soil Skeleton	2700	765	1.5
Water	1000	4179	0.613
Ice	920	2052	2.13

With the volumetric unfrozen water content provided, the volumetric ice content can be calculated.

Chapter 4. Study of Wave Propagation in Freezing Soil

The laboratory velocity test results for samples, and the numerical temperature-velocity modeling results are also presented in this chapter. The unfrozen water content test results and an analysis of the effect of grain size and clay content on acoustic velocity are included in this chapter as well. Experimental determination of unfrozen water content in freezing soil is presented in Section 4.1. Section 4.2 describes the laboratory observation and numerical modeling of wave propagation in the freezing of reconstituted Fairbanks sands. Section 4.3 presents an analysis of wave propagation in freezing sand-clay composites. Section 4.4 gives the results of laboratory observation and numerical modeling of wave propagation in freezing Fairbanks silt.

4.1. Experimental determination of UWC

The Unfrozen Water Content (UWC) of freezing soil samples was measured in the laboratory by using the FDR sensor (Hydra Vitel Probe soil water sensor, 50 MHz). The samples were quickly taken from ambient to -35°C. During a 12-hour slow reheating, the inner soil temperature and 4 DC voltage data were recorded by a programmable data logger at 15-minute intervals. The soil dielectric constants, the soil conductivity, UWC and temperature were calculated using software provided by Vitel, Inc.

Two samples, RS325 and FS01, were picked to be tested for UWC. The plot of UWC test results versus temperature and its regression curve for the reconstituted sand sample RS325 are presented in Figure 4-1. The W_u presented in the figure is the

volumetric unfrozen water content, as determined using the FDR method. The regression

function is

$$W_u = 0.038|T|^{-0.6117}$$

(Eq. 4-1)

where W_u is volumetric unfrozen water content and T is the temperature in Celsius.
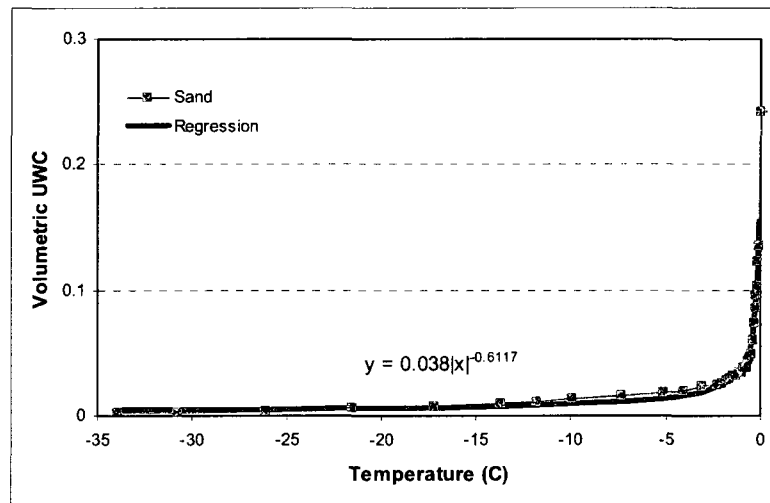
Figure 4-1. UWC vs. temperature in RS325 sand

The UWC test results for Fairbanks silt sample RS01 are shown in Figure 4-2. The

regression function is

$$W_u = 0.0765|T|^{-0.5297}$$

(Eq. 4-2)

A comparison of the W_u for the tested samples indicated that FS01 silt has more than

twice the amount of W_u (3.2% at -10°C,4.3% at -5°C, and 6.9% at -1°C) than that of

reconstituted sand RS325 (1.3% at -10°C,1.9% at -5°C, and 3.4% at -1°C). It is partly

due to the fact that FS01 silt has higher fine content as compared to FS325. Both samples,

however, have the same curve pattern: W_u drops significantly from initial moisture

content from 0°C to -1°C, with little change at temperatures below -5°C.
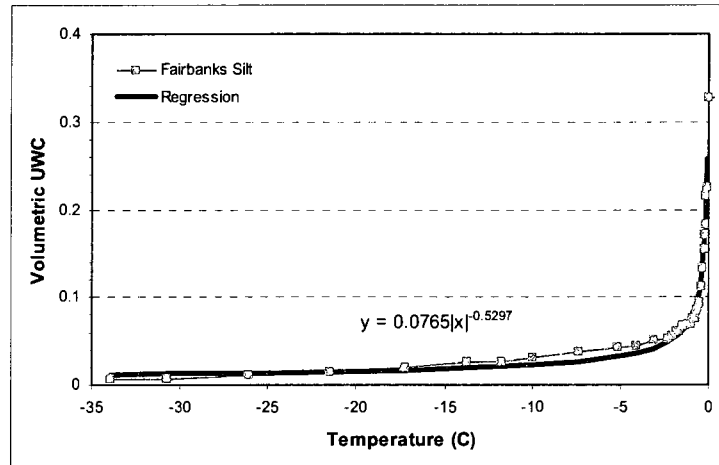
Figure 4-2. UWC vs. temperature in FS01 soil

4.2. Wave propagation in freezing reconstituted Fairbanks sands

As mentioned before, for modeling the wave velocities of freezing reconstituted sand,

sand-clay mixture and Fairbanks silt, the two-phase theory developed by King,

Zimmerman and Corwin (1988) and the Biot type-three phase theory proposed by

Leclaire et al. (1994) were reconstructed in Matlab. The compressional wave and shear

wave velocities and attenuations for unconsolidated freezing soil under various

temperatures, porosities, and saturations were calculated and compared with experimental

data.

4.2.1. Laboratory observations

The samples for this study were Fairbanks sand and silt collected on the bank of the

Tanana River near Fairbanks, Alaska. The samples were classified using 60#, 80#, 140#,

200#, and 325# sieves. Four samples with different grain sizes were obtained (Table 4-1).

The experimental sonic wave velocity test cell setup is shown in Figure 3-2. A cell

containing the water-saturated sample at ambient temperature was cooled down to -32°C.

When the inner temperature reached -30°C, the external temperature was reheated slowly

up to 0°C over 24 hours. The temperature was monitored by a thermocouple embedded in

the sample while ultrasonic measurements were made. The nominal frequencies of the

compressional transducers and the shear transducers were 400 kHz and 250 kHz,

respectively.

The P- and S-wave velocity variations of reconstituted sands caused by temperature

variations during the reheating process are shown in Figure 4-3. Generally, there is an

agreement among the 4 samples. All samples have the same curve pattern: the

compressional wave velocity, V_p, and the shear wave velocity, V_s, decrease slowly and

steadily from -30°C to -3°C, and drop quickly above -3°C. The results indicate that with

greater D10 particle size, higher P- and S-wave velocities are achieved. For instance, at

-30°C, for RS80, V_p is 4160m/s and V_s is 2524m/s; and for RS 325, V_p is 4015m/s and

V_s is 2459m/s. Effective particle size does not significantly affect the sonic velocity. But

due to the fact that the D10 particle size affects the porosity, which affects the ice and

water content, velocity variations do occur. Smaller D10 particle sizes produce greater

porosity, causing higher ice and water content; therefore, lower P- and S- wave velocities result. At freezing temperature (0°C), for all samples, V_p was 2140m/s and V_s was 843m/s, which was partly due to the high attenuation and effective signal collection.

Table 4-1. Reconstituted samples of Fairbanks sand and silt

Specimen	Sieves	D10 particle size (μm)	Specific Gravity	Porosity
RS80	60-80#	184	2.632	0.443
RS140	80-140#	112	2.660	0.464
RS200	140-200#	77	2.670	0.473
RS325	200-325#	47	2.717	0.491
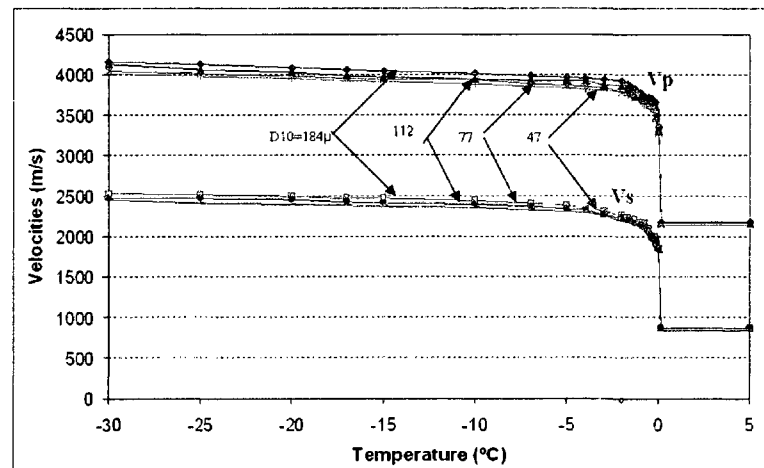
Figure 4-3. P- and S-wave velocities vs. temperature at various grain sizes (Fairbanks sand)

4.2.2. Numerical modeling

The compressional wave and shear wave velocities for unconsolidated freezing soil under various temperatures, porosities, and saturations were calculated in Matlab based on numerical theories. The physical properties of reconstituted Fairbanks sand chosen for the calculation are given in Table 4-2.

Table 4-2 Properties of reconstituted Fairbanks sand

Grain	ρ_s= 2700kg/m³	K_s=40GPa	μ_s=37GPa	k_{s0}=1.07×10⁻¹³
Ice	ρ_i= 920kg/m³	K_i=8.5GPa	μ_i=3.6GPa	K_{i0}=5×10⁻⁴
Water	ρ_w= 1000kg/m³	K_w=2.25GPa	μ_w=0GPa	$\bar{\eta}_w = 1.798 \times 10^{-3}$ Pa.S
K_{sm}=0GPa	μ_{sm}=0GPa	r_s=D10	r_{12}=0.5	R_{23}=0.5

The unfrozen water content versus temperature curves in the following calculation models are based on the empirical UWC regression function of reconstituted sand (Eq. 4-1).

1) Zimmerman and King's two-phase model

P- and S-wave velocities for experimental samples predicted by the Zimmerman and King's theory are shown in Figure 4-4. Compared with the experimental results (4000-4100m/s of P-wave velocities and 2400-2500m/s of S-wave velocities at -25°C), the Zimmerman and King theory predicts a lower P- velocities (3700-3800m/s) and S-wave velocities (2050-2100m/s).

Zimmerman and King's theory is based on the Kuster and Toksöz (1974) two-phase scattering theory. The assumptions in Kuster and Toksöz's theory are (a) the matrix is solid, (b) the inclusions are spherical, (c) the wavelengths of all waves are much longer than the inclusion radius, and (d) multiple scattering effects can be neglected. Because of these assumptions, this model is limited to two-phase media where the concentration of inclusions is small. In Kuster and Toksöz's study, it was found that the shapes and aspects ratio of inclusions (pores) had significant effects on the effective moduli and velocities. In all cases, the effective moduli and the velocities decrease with an increasing concentration of inclusions. For a given concentration, flatter inclusions (pores) have greater effect than rounder inclusions. Even a very low concentration (i.e., 0.01 percent) of thin inclusions can decrease the velocities in the composite medium by as much as 10 percent or more. Zimmerman and King's three-phase spherical inclusion model does not account for the variation of particle sizes and shapes in water-saturated media. There is some theoretical evidence (Mackenzie, 1950) that the effect of particle size distribution is also of minor importance, as long as the wavelengths considered are much greater than the diameters of the sand and clay particles, which is the case for the data collected in this study. Therefore, while the particle size distribution does not directly affect the moduli, it does have a large indirect effect, since the unfrozen water content (UWC) at a given temperature is determined by the distribution of pores, and hence particle sizes. In the experiments, because of the variation in particle sizes, the fine grains occupy the pore spaces and decrease the concentration of pores. As a consequence, the effective moduli and the velocities increase.
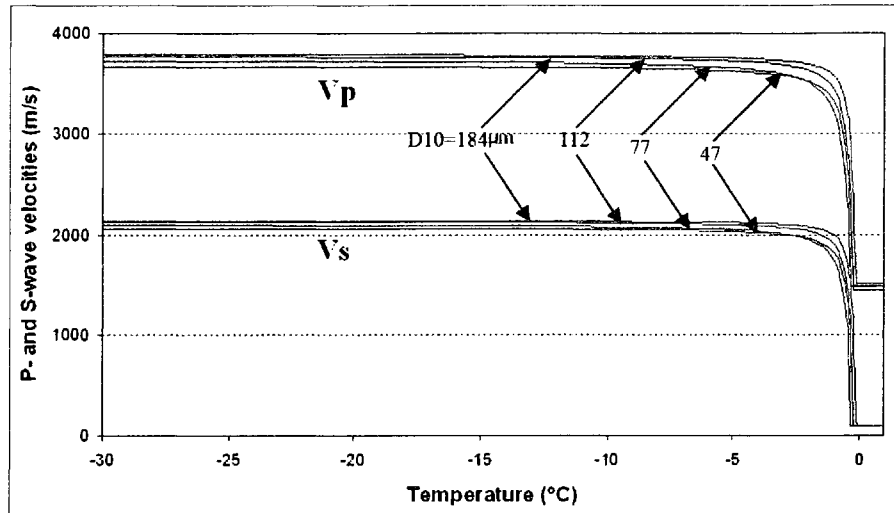
Figure 4-4. P- and S-wave velocities vs. temperatures predicted by the Zimmerman and

King's theory

2) Leclaire et al's Biot-type three-phase theory

The procedural details for the application of Leclaire et al's Biot-type three-phase

theory are given in Appendix B. P- and S-wave velocities for unconsolidated classified

sand samples predicted by Leclaire et al's Biot-type three-phase theory are shown in

Figure 4-5. As can be seen, the velocities are underestimated below 0°C. Leclaire et al's

theory predicts much lower P- velocities (2400-2450m/s) and S-wave velocities

(970-1000m/s).

Leclaire et al. (1994) computed the average moduli by extending Biot's equation to

include the ice phase. In the process of computing the rigidity and shear moduli $\tilde{R}$, the

average bulk and shear moduli (K_{av} and μ_{av}) are obtained based on Wood's (1941)

model:

$$K_{av} = [(1-c_1)\phi_s / K_s + \phi_w / K_w + (1-c_3)\phi_i / K_i]^{-1}$$

$$\mu_{av} = [(1-g_1)\phi_s / \mu_s + \phi_w / 2\omega\eta_w + (1-g_3)\phi_i / \mu_i]^{-1}$$

where c_1 and g_1 are consolidation coefficients for the solid, while c_3 and g_3 are

consolidation coefficients for the ice.
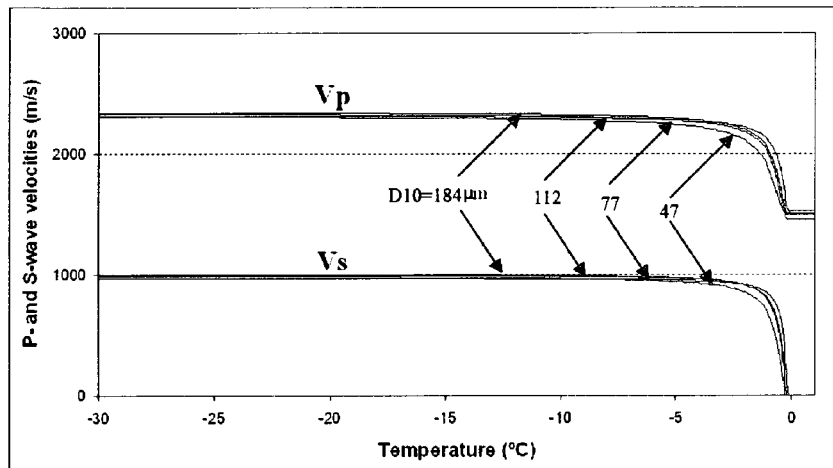
Figure 4-5. P- and S-wave velocities vs. temperatures predicted by Leclaire et al's theory

The resulting values of the elastic moduli and sonic velocities were significantly

lower than the tested values because Leclaire et al's theory does not account for the effect

of the solid-ice frame when water becomes frozen.

3) Modification of Leclaire et al's Biot-type three-phase theory

To bring the solid-ice effective frame into account, the average bulk and shear

moduli are modified based on Minshull et al's model (1994).

First, the time-average relationship is used to determine the moduli K_1 and G_1 for full

ice saturation:

$$\sqrt{\frac{\rho_1}{K_1 + 4G_1/3}} = \phi_s \sqrt{\frac{\rho_s}{K_s + 4\mu_s/3}} + (1-\phi_s)\sqrt{\frac{\rho_i}{K_i + 4\mu_i/3}},$$

$$\sqrt{\frac{\rho_1}{G_1}} = \phi_s \sqrt{\frac{\rho_s}{\mu_s}} + (1-\phi_s)\sqrt{\frac{\rho_i}{\mu_i}},$$

where $\rho_1 = \phi_s \rho_s + (1-\phi_s)\rho_i$. Secondly, Gassmann's equation determines the moduli for

the water-filled sediment:

$$K_2 - K_{sm} = \frac{(1 - K_{sm}/K_s)^2}{(1-\phi_s)/(K_w + \phi_s/K_s - K_{sm}/K_s^2)},$$

$$G_2 = \mu_{sm},$$

with $\rho_2 = \phi_s \rho_s + (1-\phi_s)\rho_w$.

Finally, the moduli for partial saturation are obtained by slowness averaging:

$$\sqrt{\frac{\rho}{K + 4G/3}} = (1-s)\sqrt{\frac{\rho_1}{K_1 + 4G_1/3}} + s\sqrt{\frac{\rho_2}{K_2 + 4G_2/3}} \qquad \text{(Eq.4-1)}$$

$$\sqrt{\frac{\rho}{G}} = (1-s)\sqrt{\frac{\rho_1}{G_1}} + s\sqrt{\frac{\rho_2}{G_2}},$$

where $s = \phi_w/(1-\phi_s)$ is the water saturation.

These average bulk and shear moduli estimation procedures were implanted into the Matlab program to replace Wood's average model. P- and S-wave velocities for unconsolidated reconstituted sand samples predicted by the modified Leclaire et al's Biot-type three-phase theory are shown in Figure 4-6. The predicted velocities fit the laboratory testing data fairly well. Leclaire et al's model gives a 0 m/s S-wave velocity at 0°C because of the assumption of no direct contact between grains. However, the lab test result gave 843 m/s. This can be explained because there exist certain solid frames at thaw condition.
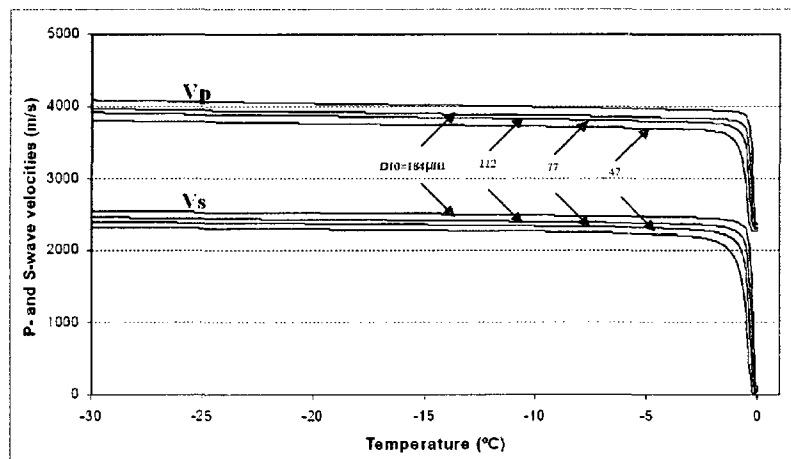
Figure 4-6. P- and S-wave velocities vs. temperatures predicted by modified Leclaire et al's theory

Zimmerman and King's model is suitable for unconsolidated freezing soil, although with a relatively large difference from what was observed in the laboratory. Leclaire et al's model underestimates the sonic wave velocities when applied to unconsolidated and consolidated frozen media. In Leclaire et al's model, modifying the average bulk and

shear moduli estimation by Minshull et al's model can significantly improve the accuracy of prediction.

For specific freezing soil samples, Leclaire et al's model needs to be modified by taking into account the clay content, partial saturation, viscosity, and pore pressure.

4.3. Wave propagation in freezing sand-clay composite

4.3.1. Laboratory observation

For studying wave propagation in frozen sand-clay mixture soils, four artificial fully-saturated Fairbanks sand samples with various clay content (10%, 20%, 30%, and 40%) were prepared (Table 4-3). The sand in the mixture was the reconstituted sand RS325, while the clay was separated from Copper River soil using a hydraulic method. The oven-dried sands and clays were weighted and well mixed, and gravimetric 20% water was added.

Table 4-3 Samples of artificial sand-clay mixture

Sample	Proportion of Sand and clay		D10 Grain	Porosity
	Sand(RS325)	Clay	size(μm)	
SC10	0.9	0.1	1.5	0.50
SC20	0.8	0.2	1.2	0.51
SC30	0.7	0.3	0.9	0.52
SC40	0.6	0.4	0.5	0.53

Plots of the V_p and V_s versus temperature for the reconstituted sands during the reheating process are presented in Figure 4-7. Generally, samples with higher clay content tested in the laboratory had a lower V_p and V_s. For instance, at -30°C, for SC10 (10% clay), V_p is 3880 m/s and V_s was measured at 2321 m/s, while for SC40 (40% clay), V_p was 3714 m/s and V_s was 2271 m/s. The velocity curve patterns also indicate significant differences. Samples with a lower clay content demonstrated a sharp change on the velocity-temperature curve; while samples with a higher clay content tended to have a gentle change on the curve. For example, for SC10, the V_p and V_s decreased slowly and steadily from -30°C to -3°C, and dropped significantly above -3°C. In contrast, for SC40, the V_p and V_s decreased slowly and steadily from -30°C to -15°C, and dropped significantly above -15°C. It appears that the content of fines greatly affected the unfrozen water content and effective porosity in the sample, which caused the variation in sonic wave propagation velocities. The lower fine content the sample contained, the smaller porosity it had, resulting the lower ice and water content and, therefore resulting in higher P- and S- wave velocities.. At freezing temperature (0°C) for SC40, V_p was 1645m/s, and V_s was 553 m/s.
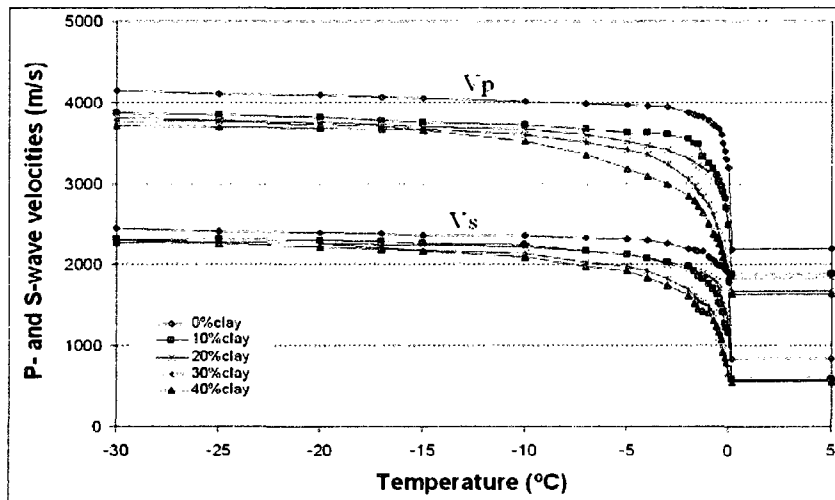
Figure 4-7. Experimental velocities vs. temperature at various clay content (Sand-clay

mixtures)

4.3.2. Numerical modeling

The physical properties of the reconstituted sand-clay mixture chosen for the

mathematical modeling are given in Table 4-4.

Table 4-4. Properties of artificial sand-clay mixture

Grain	$\rho_s= 2700kg/m^3$	$K_s=40GPa$	$\mu_s=37GPa$	$k_{s0}=1.07\times10^{-13}$
Clay	$\rho_c= 2650kg/m^3$	$K_c=20GPa$	$\mu_c=10GPa$	
Ice	$\rho_i= 920kg/m^3$	$K_i=8.5GPa$	$\mu_i=3.6GPa$	$K_{i0}=5\times10^{-4}$
Water	$\rho_w= 1000kg/m^3$	$K_w=2.25GPa$	$\mu_w=0GPa$	$\bar{\eta}_w = 1.798\times10^{-3}$ Pa.S
$K_{sm}=0GPa$	$\mu_{sm}=0GPa$	$r_s=1.5\mu m$	$r_{12}=0.5$	$R_{23}=0.5$

The mathematical model is based on

a) A modified Leclaire et al's Biot-type three-phase model

b) Mixture theory of elastic moduli of a sand-clay composite:

The mathematical model requires a composite mixing law relating the elastic moduli of a composite material to the elastic moduli and volume fractions of the constituent materials. This is a classical problem in mechanics of composite materials (Christensen, 1985). The elastic moduli of a composite are not uniquely defined by the moduli and volume fractions of constituents, but depend on the geometrical distribution of the constituents in the composite. However, the range of possible moduli of the composite is not infinite. For an isotropic geometry, its bulk and shear moduli must lie within the so-called Hashin-Shtrikman bounds (Christensen, 1985; Berryman, 1995). The lower and upper Hashin-Shtrikman bounds correspond to the geometrical distribution of the constituents, such that the softer and harder material, respectively, serve as the primary load-bearing phase. For any other isotropic geometrical distribution of the constituents, the moduli lie between these two bounds.

A clay-sand mixture can be thought of as a material with two constituents, with sand being the harder and clay   the softer constituent. For this reason, the lower Hashin-Shtrikman bound is sometimes used as a mixing law for sand-clay mixtures, such as in the homogenized matrix model (Goldberg and Gurevich, 1998).

The Composite Mixing Law (Lower Hashin-Shtrikman bound) can be expressed as follows:

$$K_s = K_{HS-} = K_{clay} + \frac{(1-C)(K_{sand} - K_{clay})}{1 + C(K_{sand} - K_{clay})/(K_{sand} + \frac{4}{3}K_{clay})}$$

$$\mu_s = \mu_{HS-} = \mu_{clay} + \frac{(1-C)(\mu_{sand} - \mu_{clay})}{1 + C(\mu_{sand} - \mu_{clay})/(\mu_{sand} + \frac{4}{3}\mu_u)}$$

μ_u is given by

$$\mu_u = \frac{3}{2}\left(\frac{1}{\mu_{clay}} + \frac{10}{9K_{clay} + 8\mu_{clay}}\right)^{-1}$$

By applying this Lower Hashin-Shtrikman Bound Mixing Law to the physical properties of reconstituted Fairbanks sand-clay mixture in Table 4-4, the bulk and shear moduli versus clay content obtained are shown in Figures 4-8 and 4-9. The bulk and shear moduli of the solid grain material at low but non-zero clay contents exhibit a rapid reduction.
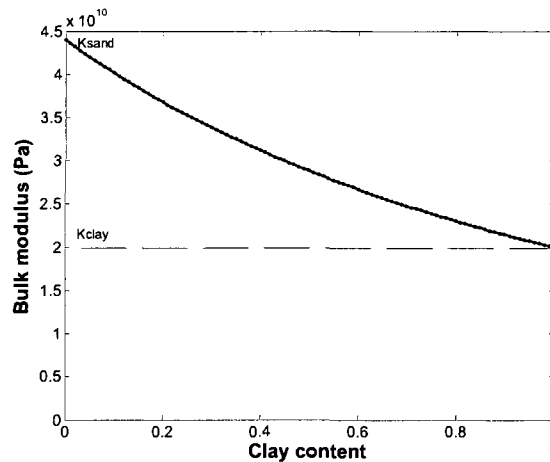
Figure 4-8. Bulk moduli of the quartz grain material versus clay content
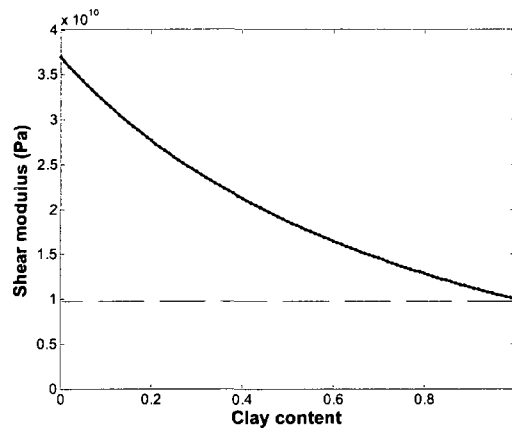
Figure 4-9. Shear moduli of the quartz grain material versus clay content

By migrating these equations into Matlab, the elastic moduli of the sand-clay

composite were obtained. Subsequently, V_p and V_s can be calculated.

The V_p and V_s for sand-clay composite samples predicted by the modified Leclaire

et al's Biot-type three-phase theory combine with composite mixing law are presented in

Figure 4-10. The predicted velocities fit the laboratory testing data fairly well with an

exception. Leclaire et al's model gave a 0 m/s S-wave velocity at 0°C for all samples

because of the assumption of no direct contact between grains. The actual lab test result

yielded 553 m/s for SC40, mainly due to some contacts between grains.
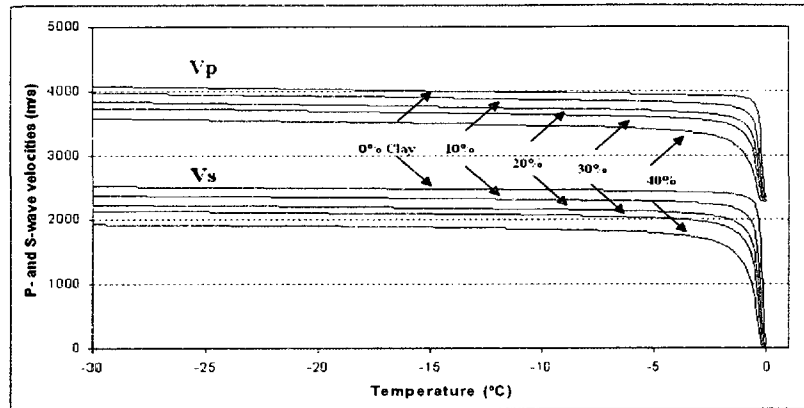
Figure 4-10. P- and S-wave velocities of sand –clay composite predicted by modified

Leclaire et al's theory

4.4. Wave propagation in freezing Fairbanks silt

4.4.1. Laboratory observation

Following the test procedure described in Section 3.1, the V_p and V_s of Fairbanks

silt (FS01) were tested from -30°C to 5°C. Plots of the V_p and V_s versus temperature

for FS01 during the reheating process are presented in Figure 4-11.

The pattern of V_p and V_s curves is close to SC20 (Sand-clay composite with 20%

clay content). The V_p and V_s decreased slowly and steadily from -30°C to -15°C, and

dropped quickly above -5°C. At -30°C, V_p was 3985 m/s and V_s was 2911 m/s; at

-15°C, V_p was 3768 m/s and V_s was 2157 m/s; and at -0°C, V_p was 1857m/s and V_s

was 658 m/s;
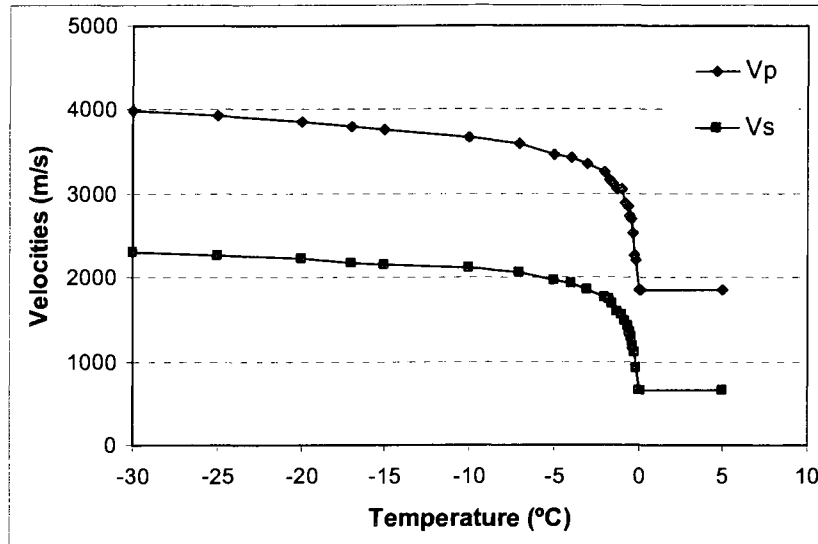
Figure 4-11. Tested P- and S-wave velocities vs. temperature (Fairbanks silt FS01)

The regression functions of tested V_p and V_s are:

$$Vp = 319.83Ln(-T) + 2946.9 \quad (T<0)$$ (Eq. 4-3)

$$Vs = 248.22Ln(-T) + 1527.9 \quad (T<0)$$ (Eq. 4-4)

4.4.2. Numerical modeling

The Fairbanks silt (FS01) is a sand-clay composite material. Its PSD curve (Figure 3-1) indicates that it consists of 9% clay and 90% silt. The elastic moduli of FS01 were calculated using composite mixing law (Lower Hashin-Shtrikman bound) with 9% clay content. The physical properties of FS01 chosen for the calculation are given in Table 4-5.

Table 4-5. Properties of Fairbanks silt

Grain	ρ_s= 2700kg/m³	K_s=40GPa	μ_s=37GPa	k_{s0}=1.07×10⁻¹³
Clay	ρ_c= 2650kg/m³	K_c=20GPa	μ_c=10GPa	
Ice	ρ_i= 920kg/m³	K_i=8.5GPa	μ_i=3.6GPa	k_{i0}=5×10⁻⁴m²
Water	ρ_w= 1000kg/m³	K_w=2.25GPa	μ_w=0GPa	$\bar{\eta}_w = 1.798\times10^{-3}$ Pa.S
K_{sm}=0GPa	μ_{sm}=0GPa	r_s=1.5µm	r_{12}=0.5	R_{23}=0.5

The V_p and V_s for Fairbanks silt (FS01) predicted by the modified Leclaire et al's

Biot-type three-phase theory combined with the composite mixing law are presented in

Figure 4-12. The predicted velocities fit the laboratory testing data fairly well. Leclaire et

al's model gives a 0 m/s of V_s at 0°C because of the assumption of no direct contact

between grains. The lab test result was 658 m/s. The regression functions of simulated

V_p and V_s are:

$$Vp = 175.35\mathrm{Ln}(\text{-T}) + 3338.2 \quad (\text{T<0}) \qquad\qquad (\text{Eq. 4-5})$$

$$Vs = 209.69\mathrm{Ln}(\text{-T}) + 1479.3 \quad (\text{T<0}) \qquad\qquad (\text{Eq. 4-6})$$

The predicted V_p at low temperature (<-20°C) are a bit lower than tested values,

but higher in the -15 to -2°C temperature range. The predicted values reveal   a flat

pattern, while the actual tested V_p reduced faster from -15 to -5°C. Although

discrepancy exists, the prediction is reasonably good and the model is acceptable to be

applied in numerical simulations. Eq. 4.5 is, therefore, used to convert the temperature

distributions obtained in FEM simulation to P-wave velocity tomograms, as described in

Chapter 6.
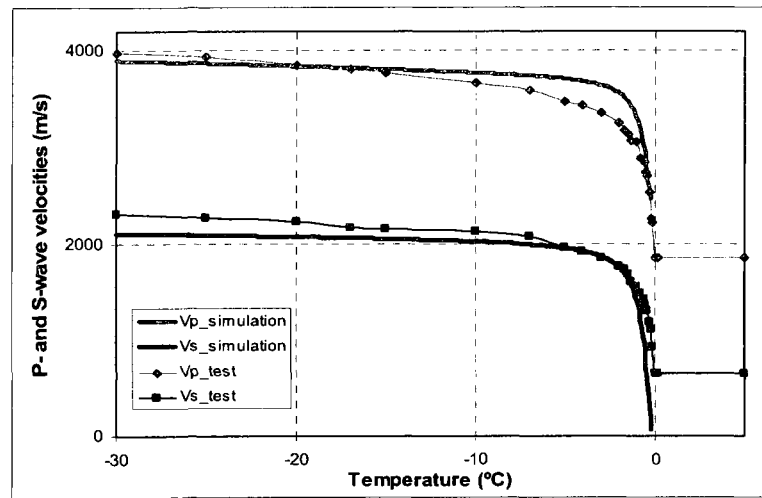
Figure 4-12. P- and S-wave velocities vs. temperature (Fairbanks silt FS01)

Chapter 5. Experimental Study of Dynamic Freezing Process Using Computerized Ultrasonic Tomography (CUST)

In this chapter, the inward and outward freezing process and freezing front development of Fairbanks silt samples are observed using a Multi-channel Ultrasonic Scanning System (MUSS), and sonic wave velocity tomographies are generated using a simultaneous iterative reconstruction technique (SIRT). In Section 5.1, the Computerized Ultrasonic Tomography (CUST) scanning on dynamic inward freezing process (IW test) is discussed. In Section 5.2, the CUST study on dynamic freezing process of soil surrounding chilled pipe (OW test) is presented.

5.1. Dynamic inward freezing process (IW test)

A cylindrical Fairbanks silt (FS_IW) specimen with a 101.6 mm diameter, 152 mm length and 20% moisture content was used to perform the inward dynamic freezing process. The MUSS was used to conduct the P-wave velocity (V_p) scanning. The laboratory setup is shown in Figure 5-1. The axes of the 14 P-wave transducers point to the center of the soil column, with angles of 25.7° between their axes. The horizontal acoustic measurement plane perpendicular to the axis of the cylindrical specimen was installed at the midpoint of the soil column length. The transducers were fixed to the soil surface with a mounting rack. The mounting rack consisted of a 101.6 mm inner diameter PVC cylinder ring with 14 holes of 8.5 mm in diameter. The transducers mounted in the holes were tightened by another aluminum ring with an adjusting screw. Final contact was achieved by applying the couplant into the holes before attaching the transducers

onto the soil surface. As compared with direct contact, the gel-contacting glue markedly improved the travel time measurements with enhanced signal strength at the receiving sensors.
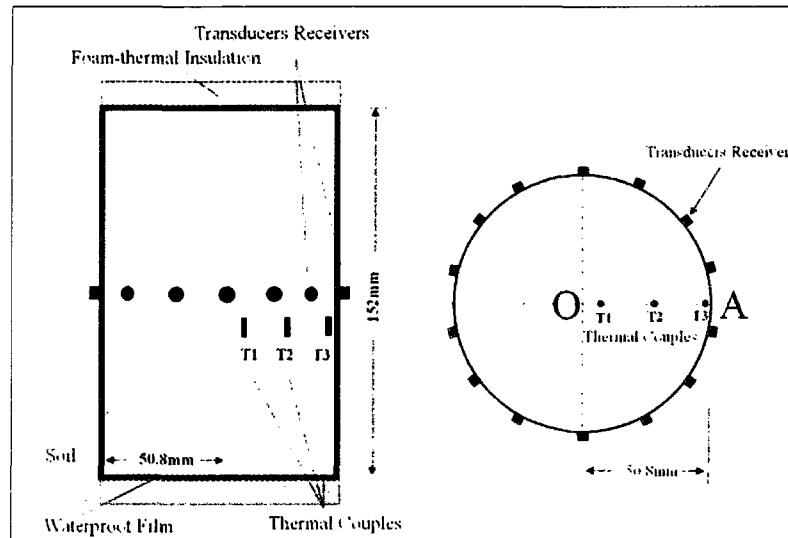
Figure 5-1. Laboratory setup of IW test

The soil sample was prepared using a standard 4-inch soil test mold following the original proctor test standard, ASTM D698. The oven-dried soil was mixed with gravimetric 20% distilled water. Three thermal couples (T1, T2, and T3) were installed on the plane of 10mm below the horizontal scanning measurement plane at the positions of 5, 0; 27, 0; and 50, 0 mm (using a Cartesian coordinate system with the origin at the center of the sample). The sample was sealed with thin plastic film to prevent the loss of moisture content and placed in a freezer with the temperature stabilized at -32°C.
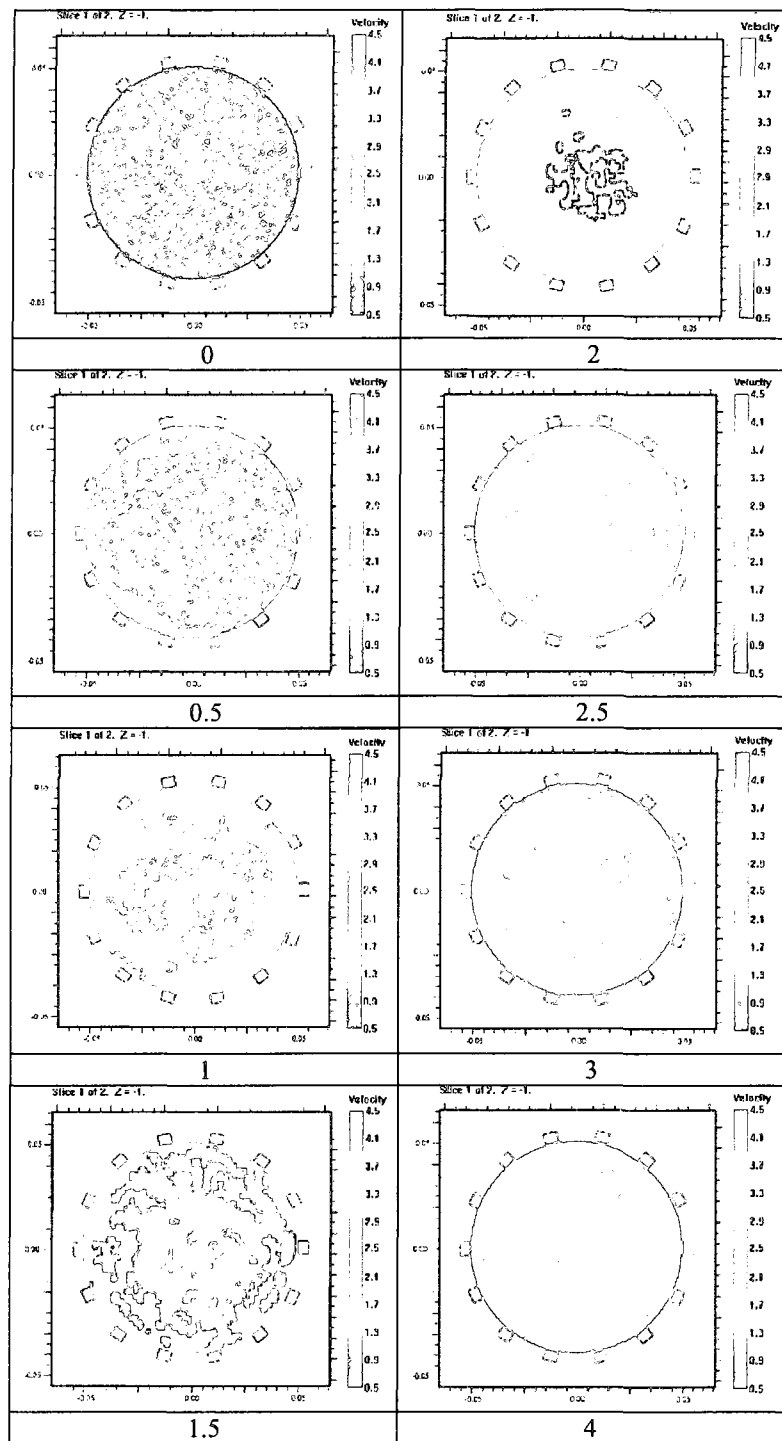
Figure 5-2. Sonic wave velocity tomograms vs. time from IW test (number under

tomography is the time from start point of freezing process in hours)

The ultrasonic scanning followed the procedure described in Section 3.1.5. The process began by initiating a P-wave pulse from one ultrasonic sensor serving as a transmitter and using the remaining 13 sensors as the receivers. The scanning continued one transmitter at a time until all 14 sensors were covered and a total of 14x13 = 182 ray paths were tested. Therefore, 182 waveforms are recorded and processed to obtain the first breaks. The scan was performed and recorded each 15 minutes until 4 hours after freezing, when no significant travel time changes could be observed.

Sonic wave velocity tomograms vs. time from IW test are presented in Figure 5-2.

The significant changes of the velocity concentration region can be identified during first 2.5 hours, while the tomograms keep steady after 4 hours. The freezing front development can be clearly observed in these tomograms by giving a certain velocity as a soil frozen point.

In order to visualize and quantify the variation of sonic velocities, the V_p values were   picked at 5 locations (x1, x2, x3, x4, x5) along the x axis on the O-A cross-section (refer to Figure 5-1) of each tomogram, with x1 at 5mm from center, x2 at 16 mm, x3 at 27 mm, x4 at 38 mm, and x5 at 50 mm, based on the Cartesian coordinates system with the origin at the center of the sample. The V_p profiles were generated and are presented in Figure 5-3. Locations of x1, x3, and x5 (5, 27 and 50 mm) are equivalent to thermal couple locations T1, T2 and T3, as illustrated in Figure 5-1. The recorded temperature variation from three thermal couples is presented in Figure 6-3. The initial temperature was 17°C at 0 hours of freezing and the velocities tested were around 685-725 m/s at the

5 locations. After 0.5 hours of freezing, the V_p at x5 rose to 1505 m/s, with a

temperature of -2°C at T3 due to a small amount of water partially frozen, while there

were no identifiable velocity changes at x1 and x2. From 0.5 to 2 hours of freezing, the

temperature recorded at x5 tended to slowly decrease from -2°C to -5°C, while the

temperature dropped quickly before 0.5 hours and after 2 hours of freezing. This can be

explained by the effect of phase change from water to ice. At 1 hour of freezing,

temperatures at T1 and T2 were close to 0°C, and were -3°C at T3. The V_p at x5 was

2510 m/s, indicating the soil was frozen at that location. At x5 (T3), after 2 hours of

freezing, the V_p reached the maximum, 4100 m/s, and no change was observed

thereafter. At x1(T1), after 2 hours of freezing, the V_p was 2300 m/s. It then sped up to

3800 m/s at 2.5 hours. Velocities at all locations reached the steady state after about 3

hours, with magnitudes in the range of 4100-4200 m/s.
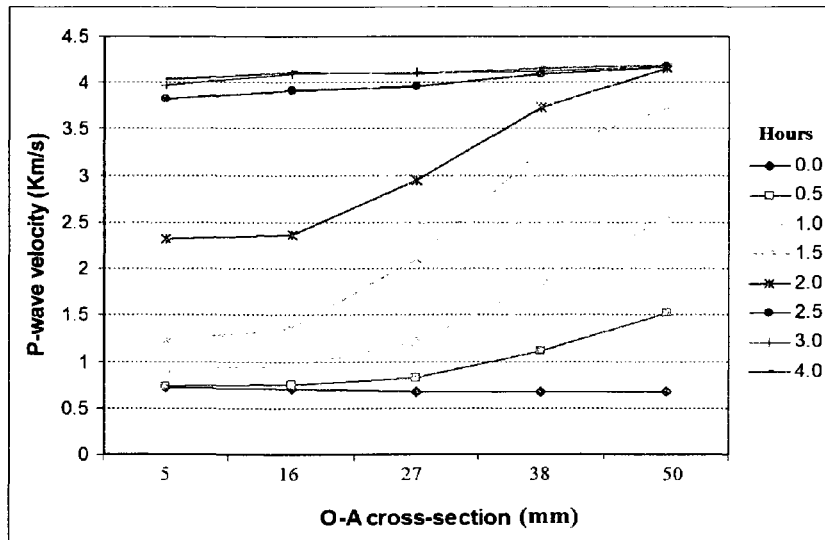
Figure 5-3. Velocity profiles of OA cross-section vs. time steps (IW test)

5.2. The dynamic outward freezing process in soil surrounding a chilled pipe (OW test)

Much like the setup for the IW test, the outward dynamic freezing process was tested using a cylindrical Fairbanks silt (FS_OW) specimen 10.16 cm in diameter, 15.2 cm in length and with 20% moisture content. Also, the MUSS was used to conduct the P-wave velocity (V_p) scanning. The laboratory setup is shown in Figure 5-4. One copper pipe 10 mm in diameter was installed along the axis during specimen preparation. The axes of the 14 P-wave transducers pointed to the center of the soil column, with angles of 25.7° between their axes. The horizontal acoustic measurement plane perpendicular to the axis of the cylindrical specimen was installed in the middle of the specimen. The transducers were fixed to the soil surface with a mounting rack. The mounting rack consisted of a 101.6 mm inner diameter PVC cylinder ring with 14 holes with 8.5 mm diameter. The transducers mounted in the holes were tightened by another aluminum ring with an adjusting screw. Final contact was achieved by applying the couplant into the holes before attaching the transducers onto the soil surface. The gel-contacting glue was also used to improve the signal strength.

The soil sample was prepared using a standard 4-inch soil test mold. The 10 mm diameter copper pipe was placed in the middle of the mold. The oven-dried soil was mixed with gravimetric 20% distilled water and compacted following the original proctor test standard, ASTM D698. Three thermal couples (T1, T2, T3) were installed on the plane 10mm below the horizontal scanning measurement plane at the positions of 5, 0; 27, 0; and 50, 0 mm (Cartesian coordinates system with the origin at the center of the

sample). The sample was sealed with thin plastic film to prevent the loss of moisture

content. The sample was well insulated using insulation foam. The copper pipe was

connected to a cold bath. The soil specimen was refrigerated by flowing cold antifreeze

from the cold bath, with the temperature of the antifreeze maintained at -22°C.
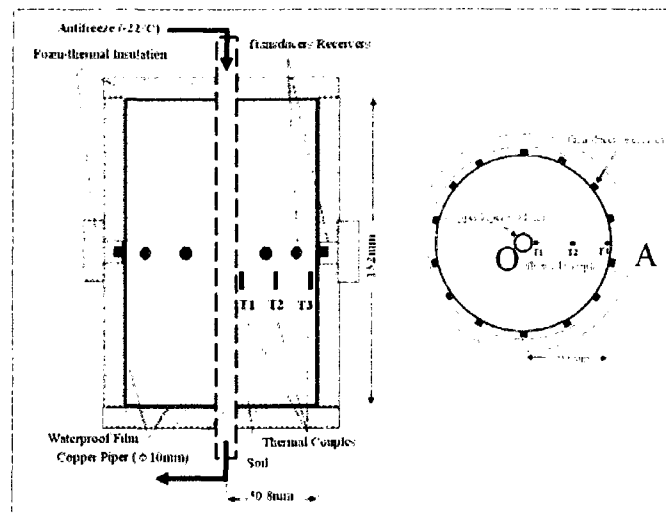
Figure 5-4. Laboratory setup of OW velocity scanning test

The ultrasonic scanning followed the procedure described in Section 3.1.5. The

process was begun by initiating a P-wave pulse from one ultrasonic sensor serving as a

transmitter and using the remaining 13 sensors as receivers. The scanning continued with

one transmitter at a time until all 14 sensors were covered and a total of 14x13 = 182 ray

paths were tested. Thus, 182 waveforms were recorded and processed to obtain the first

breaks. The scanning was performed and recorded each 15 minutes until 7 hours of

freezing, after which no significant wave travel time changes could be detected.

Sonic velocity tomograms vs. time from the OW test are presented in Figure 5-5. Significant changes of velocity concentration regions were identified during the first 4 hours of freezing. The tomograms kept steady after 7 hours. The freezing front development can be observed clearly from these tomograms. The dynamic process of frost bulb development and the freezing front movement were clearly observed in the experiments. The freezing rate obtained by MUSS is comparable with that obtained by thermal couples. Average freezing front critical sonic velocity was 2400 m/s, but it appeared to be lower at earlier stages of freezing due to error introduced by a smaller frost bulb diameter. The same procedures performed for the IW test were followed to generate the V_p profiles for each tomogram of the OW test. The V_p values were picked at 5 locations along the x axis on the O-A cross-section (from center to outer surface) of each tomogram (x1 at 5 mm from center, x2 at 16 mm, x3 at 27 mm, x4 at 38 mm, and x5 at 50mm, based on the Cartesian coordinates system with the origin at the center of the sample). The V_p profiles are presented in Figure 5-6. Locations of x1, x3, and x5 (5, 27 and 50 mm) were equivalent to thermal couple locations T1, T2 and T3, which are illustrated in Figure 5-4. The recorded temperature variation from the three thermal couples is presented in Figure 5-7.
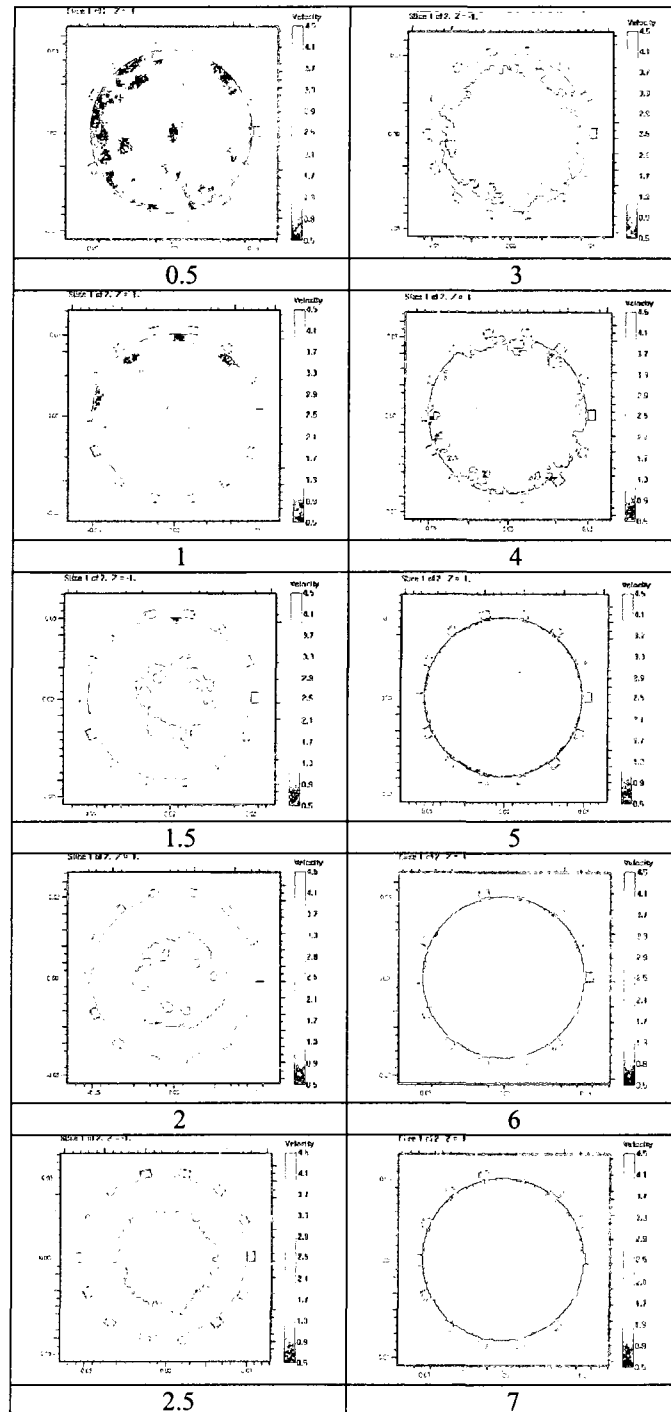
Figure 5-5. Sonic wave velocity tomograms vs. time from OW test (the number under the

tomography is the time from the starting point of the freezing process in hours)

The initial soil temperature was 17°C at 0 hours of freezing, and, as mentioned above, the temperature of the antifreeze flow in the pipe was maintained at -22°C. The sonic wave velocities tested were approximately 685-725 m/s at 5 locations. At 0.5 hours of freezing, the V_p at x1 rose to 1850 m/s with -11°C at T1 due to a small amount of water partially frozen, while there were no identifiable velocity changes at x5 after 1 hour of freezing. The experimental temperature profile in Figure 5-7 shows that there was a flat curve section at T2 and T3 from 1.0 to 2.5 hours of the freezing period, while the temperature dropped quickly before 1.0 hour and after 2.5 hours of freezing. Similar to the case of IW test, this can be explained by the effect of phase change from water to ice. At 0.5 hours of freezing, the temperature at T1 was -10°C and the V_p tested was 1930 m/s at x1. The V_p reached 2900 m/s at 1 hour, 3740 m/s at 1.5 hours, and 4100 m/s at 2.5 hours, which is close to the maximum V_p of 4200 m/s. At x5 (T3), after 1 hour of freezing, the V_p increased slowly and reached 1900 m/s after 3 hours. It then sped up, reaching 3500 m/s at 4 hours and 4150 m/s at 6 hours. After about 6 hours of freezing, there was no significant wave travel time change. At that time, the velocities at all locations reached the steady state, with a magnitude in the range of 4100-4200 m/s.
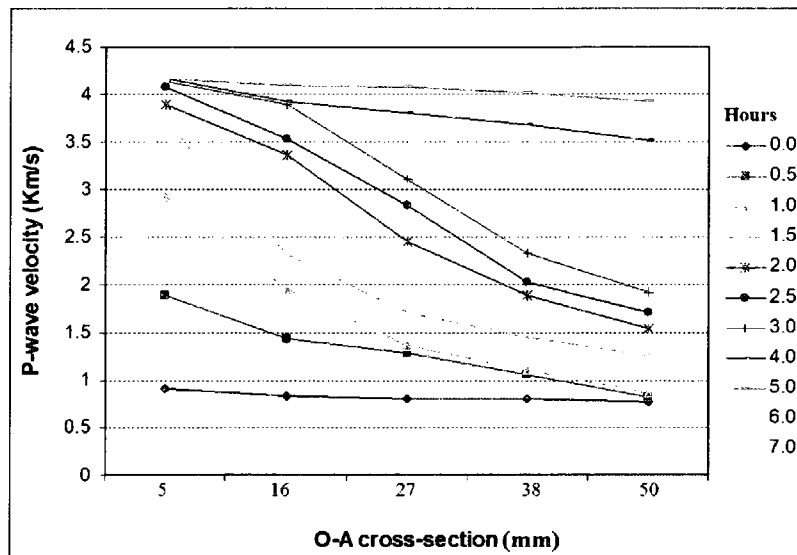
Figure 5-6. Sonic wave velocity profiles of OA cross-section vs. time steps (OW test)
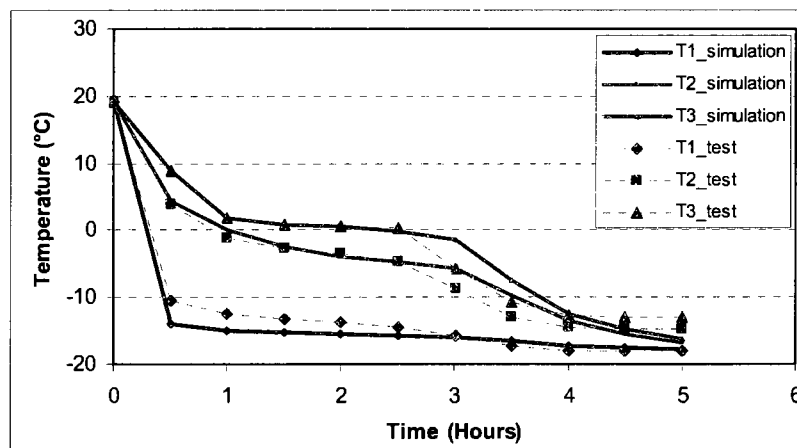
Figure 5-7. Temperature vs. time steps at 3 reference locations in the OW simulation

compared with those from the 3 thermal couples in the OW laboratory test

5.3. Discussion on Freezing Front Movement

The inward and outward freezing process and freezing front development of

Fairbanks silt samples were observed using a Multi-channel Ultrasonic Scanning System

(MUSS), and the sonic wave velocity tomographies were generated using the simultaneous iterative reconstruction technique (SIRT). The MUSS tomograms allow real-time observation of freezing front development, permitting in-depth analysis of the freezing process in the samples. The freezing front analysis is presented below.

Soil is called "frozen" at the accumulation of ice to a certain proportion. The P-wave velocity is proportional to the ice accumulation in the soil. By giving a certain P-wave velocity as a "frozen" point, the freezing front can be delineated as a contour line on a tomogram. As indicated by the P-wave vs. temperature curve in Figure 4-12, the P-wave velocity is around 1800 m/s before the silt is frozen. It increases steeply at the freezing point. Based on this observation, it is determined in the analysis that the freezing front is the contour line of P-wave velocity at 2000 m/s, a significant changing point for P-wave propagation velocity when silt is frozen. Figure 5-8 and Figure 5-9 illustrate the freezing front development for IW and OW CUST tests based on the P-wave velocity of 2000 m/s contour.

In Figure 5-8, soil starts to be partially frozen at a few areas of outer boundary after 1 hour of freezing in the IW test. Then the freezing front accelerates inward to the center of the sample. After 1.5 hours of freezing, forty percent of the regions are frozen (yellow region in the second graph). Ninety percent of the region is frozen after 2 hours of freezing, and the soil is considered to be "totally frozen" after 2.5 hours of freezing. The P-wave velocities, however, continue to increase until reaching their maximum since the unfrozen water content continues to decrease.
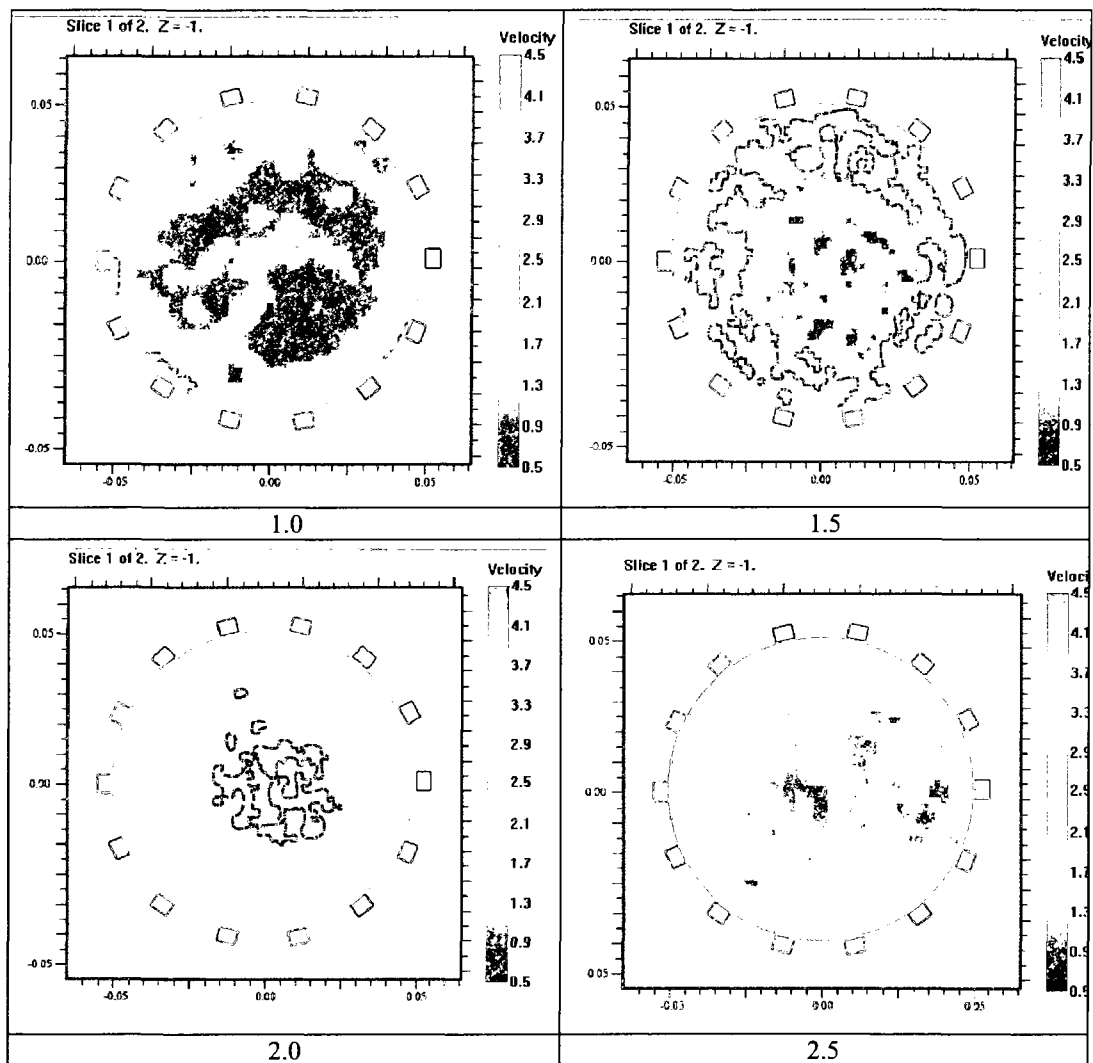
Figure 5-8. Frozen front development in the IW test (number under tomography is the
time from start point of freezing process in hours)

Figure 5-9 shows the freezing front development in the OW CUST test. After 1 hour

of freezing, soil starts to become partially frozen around the chilled pipe located in the

center of the sample. Then the freezing front gradually moves outward to the insulated

outer boundary. After 4 hours of freezing, the soil is considered "totally frozen" because

the velocities at all the regions are great than 2000 m/s. Similar to the IW test, the P-wave

velocities continue to increase until reaching their maximum due to continued decrease in the unfrozen water content.

The actual resolution of the tomograms present above for the IW and OW CUST tests is a bit lower than what it is shown. There were 14 P-wave PZT sensors with a 400 kHz frequency used in this study. With a 4000 m/s velocity for deeply frozen soil, the wavelength is about 1 cm. The maximum frequency-based resolution of the tomography is, therefore, 1 cm. Numerical interpretation was used to increase the data points used in the tomograms for better visualization of the graphs.

Porous media and soil have a higher wave attenuation compared with hard rock and concrete. Higher frequency ultrasonic is difficult to apply to soil study to improve the resolution, due to the high attenuation of the sonic waves, a low signal to noise ratio (SNR), and difficulty in first arrival time picking. S-wave CUST may produce additional information to study the freezing process and the physical properties of soil. However, it was not conducted in this study due to the size of shear wave sensors. A shear wave sensor is normally larger than 2.5 cm and needs stronger coupling. It is not possible to mount multiple shear sensors around a 10-cm-diameter cylindrical soil specimen. For larger specimens, the S-wave CUST could possibly be conducted.
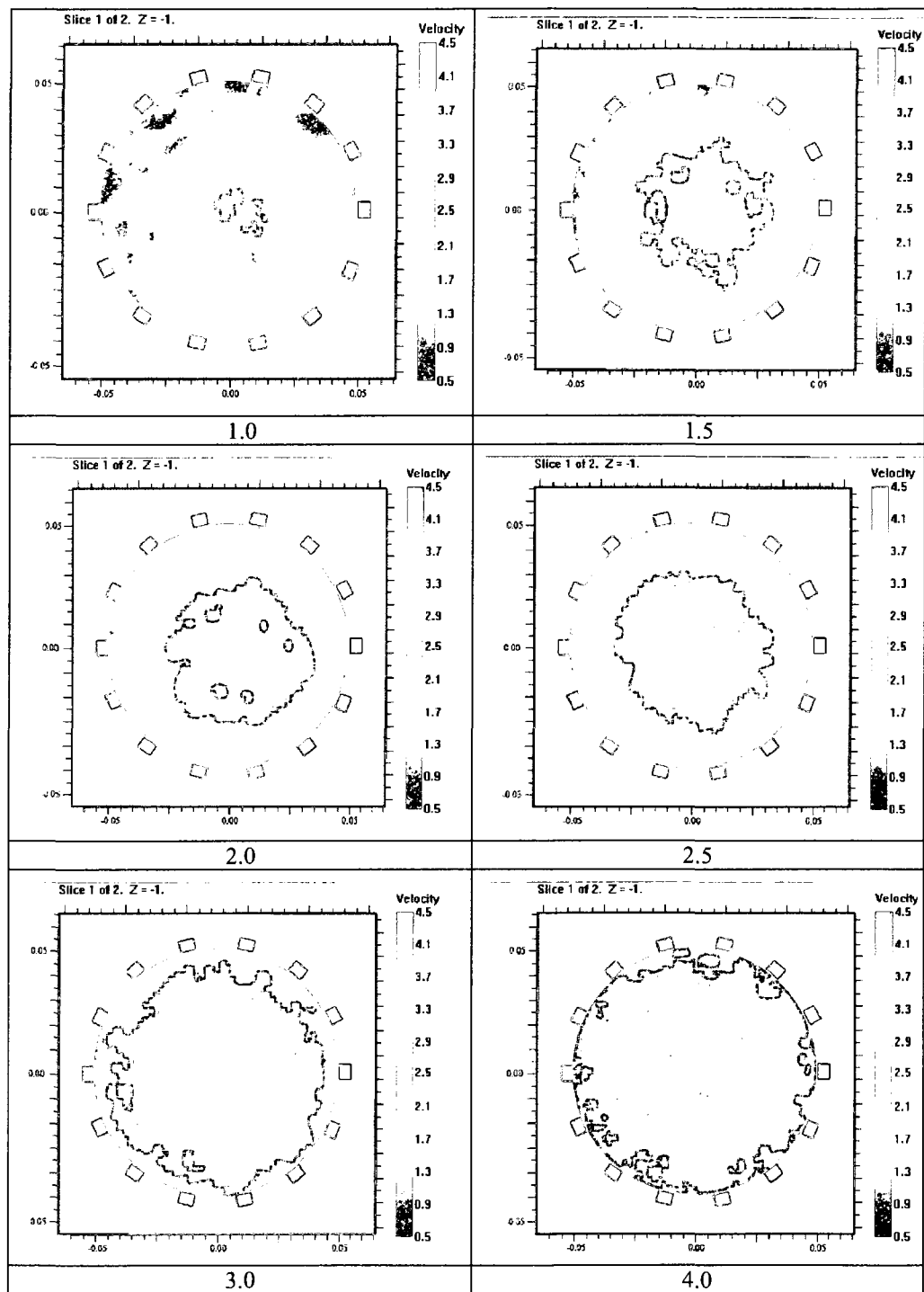
Figure 5-9. Frozen front development in OW test (number under tomography is the time

from start point of freezing process in hours)

Chapter 6. FEM Modeling of the Freezing Process

This chapter describes comprehensive numerical FEM simulations, which take into account the heat conduction in porous media, the latent heat effect, and the nonlinear thermal properties of soil, performed on the inward and outward freezing process of Fairbanks silt. The simulations are based on the experimental conditions described in Chapter 5. The output contains temperature distributions in the models. Sonic wave velocity tomograms are then generated based on the simulation output of temperature distributions utilizing the temperature-sonic velocity model discussed in Section 4.4.2.

6.1. Numerical experiment

The assumptions, governing equations, and procedures of FEM modeling used in this study are discussed in detail in Section 3.2.2. The numerical procedure for simulating the transient heat transfer in freezing soils was conducted using the Earth Science module in Comsol Multiphysics. Based on the Conduction in Porous Media method in the Earth Science module, combined with the phase change model and moisture content function of Fairbanks silt, the transient heat transfer of freezing process of Fairbanks silt were simulated and analyzed. Simulations of inward and outward two-dimensional freezing problems in freezing soils are presented to compare with the laboratory experimental results. The final outputs of the simulation are the temperature distributions and profiles in the spatial and temporal domains.

Based on the same configuration as in the laboratory CUST scanning, both inward and outward freezing process simulations use Fairbanks silt with the same physical properties.

The values of thermal properties of Fairbanks silt for the soil skeleton, water, and ice used in the simulations are listed in Table 6-1.

Table 6-1. Thermal properties of soil (Fairbanks silt)

	Density $\rho(kg/m^3)$	Specific heat capacity $C_p(J/kg°C)$	Thermal conductivity $k(W/m°C)$
Soil Skeleton	2700	765	1.5
Water	1000	4179	0.613
Ice	920	2052	2.13

The unfrozen water content (UWC) plays an important role in heat transfer in soils. It determines not only how much latent heat is released, but also the effective thermal properties C_{eq} and K_{eq}. The measurement of UWC for Fairbanks silt using FDR is described in Section 4.1. The UWC test results for Fairbanks silt sample RS01 are shown in Figure 4-2. The regression function is

$$W_u = 0.0765|T|^{-0.5297}$$

where W_u is the volumetric unfrozen water content and T is the temperature in degrees Celsius.

A scalar expression of this function was created in the Earth Science module of Comsol Multiphysics to calculate the volumetric UWC in Fairbanks silt, with temperature as the variable. With the volumetric unfrozen water content provided at certain temperatures, the volumetric ice content can be calculated by the function

$$\theta_i = (1 - \theta_s) - \frac{\rho_s}{\rho_w} \theta_s W_u$$

where θ_s is the proportion of soil grain.

As described in Section 3.22, the equation coefficients C_{eq} and K_{eq} are effective properties that describe a representative volume of the solids and liquids in a model to store and transmit heat. The effective properties may change value in space and time and may depend on the results from this equation and others.

The Earth Science Module of Comsol Multiphysics defines C_{eq} and K_{eq} with information provided on the volume fraction, θ, density, ρ, specific heat capacity, C_p, and thermal conductivity, K for both fluids and solids in a model. The equations defining C_{eq} and K_{eq} are

$$C_{eq} = \frac{\sum \theta_{Li} \rho_{Li} C_{pLi} + \sum \theta_{Pi} \rho_{Pi} C_{pPi}}{\sum \theta_{Li} + \sum \theta_{Pi}}$$

$$K_{eq} = \frac{\sum \theta_{Li} K_{Li} + \sum \theta_{Pi} K_{Pi}}{\sum \theta_{Li} + \sum \theta_{Pi}}$$

where the subscripts "L" and "P" denote liquid and solid properties, respectively. The equations amount to volume averaging.

After incorporating the latent heat into the heat capacity, the heat conduction with phase change governing equation can be expressed as

$$(C_{eq} - L\rho_i \frac{\partial \theta_i}{\partial t}) \frac{\partial T}{\partial t} = \nabla(K_{eq} \nabla T)$$

where ρ_i is the density of ice, θ_i is the volumetric fraction of ice, L is the latent heat of fusion per unit mass of water (approximately 3.33×105 J / kg), ∇ is the gradient operator, $\nabla = \frac{\partial}{\partial x} + \frac{\partial}{\partial y} + \frac{\partial}{\partial z}$. $C_{eq} - L\rho_i \frac{\partial \theta_i}{\partial t}$ is termed the apparent volumetric heat capacity.

In the Earth Science Module of Comsol Multiphysics, under the Subdomain Settings, the equivalent volumetric heat capacity can be customized based on the above apparent volumetric heat capacity equation.

6.2. Dynamic freezing process of cylindrical Fairbanks silt specimen (IW simulation)

In Section5.1, the cylindrical Fairbanks silt (FS_IW) specimen, 101.6 mm in diameter, 152 mm in length, and 20% moisture content was used to perform the inward dynamic freezing experiment. The CUST scanning plane was perpendicular to the axis of the cylindrical specimen through the middle section of the specimen. Three thermal couples (T1, T2, and T3) were installed on the plane of 10mm below the horizontal scanning measurement plane at the positions of 5, 0; 27, 0; and 50, 0 mm based on the Cartesian coordinates system, with the origin at the center of the sample. The sample was sealed with a thin plastic film to prevent the loss of moisture and then placed in a freezer

with the inner ambient temperature maintained at -32°C. The CUST scanning was performed and recorded each 15 minutes until no significant travel time changes could be observed.

For simulating this scenario, 2D circular-shaped geometry with a 101.6mm diameter along the CUST scanning plane is constructed to simulate the heat flow during the freezing process (Figure 6-1). For the convenience of comparative analysis with the experimental CUST, the entire circular shape instead of a symmetrical half-circular shape is used. The settings and parameters of FEM simulation using Comsol Multiphysics are given below:

Figure 6-1. Geometry and mesh of IW simulation

1) Model properties:

Application mode type: 2D, Conduction in Porous Media (Earth Science Module)

2) Constants:

The physical constants and coefficient used in the IW simulation for Fairbanks silt are listed in Table 6-2.

3) Variable:

Dependent variable: T (temperature)

4) Boundary setting:

Type: Heat flux

Heat transfer coefficient: 40 W/(m²·K)

External temperature: -30°C

5) Subdomain setting:

Equivalent volumetric heat capacity:

$$C_{eq} = \frac{\sum \theta_{Li} \rho_{Li} C_{pLi} + \sum \theta_{Pi} \rho_{Pi} C_{pPi}}{\sum \theta_{Li} + \sum \theta_{Pi}} - L\rho_i \frac{\partial \theta_i}{\partial t}$$

Subdomain initial value (temperature): 17°C

6) Solver settings:

Analysis type: Transient

Solver: Time dependent

Table 6-2. Physical constants and coefficient of Fairbanks silt

Name	Expression	Value	Description
T_trans	0.3[degC]	0.3	Freezing point
scale	0.5	0.5	Width of smoothed step function
rho_s	2700[kg/m^3]	2730	Density of grain
rho_i	920[kg/m^3]	918	Density of ice
rho_w	1000[kg/m^3]	1000	Density of water
nu0	0.29	0.29	Poisson's ratio
alpha_s	0.8e-6[1/K]	0.8e-6	Coefficient of thermal expansion
T_init	17[degC]	17	Initial temperature
k_s	1.5[W/(m*K)]	1.5	Thermal conductivity above freezing point
k_i	2.13[W/(m*K)]	2.13	Thermal conductivity of ice
k_w	0.613[W/(m*K)]	0.613	Thermal conductivity of water
Cp_s	765[J/(kg*K)]	765	Heat capacity above freezing point
Cp_i	2052[J/(kg*K)]	2052	Heat capacity of ice
Cp_w	4179[J/(kg*K)]	4179	Heat capacity of water
kappa_s	3.2e-6[m^2]	3.2e-6	Permeability of unfrozen sand
eta_s	0.001[Pa*s]	0.001	Dynamic viscosity
E0_s	93[MPa]	93	Young's modulus
dT	0.5[K]	0.5	Half width of Gauss bell curve
lam	333[kJ/kg]	333	Latent heat of freezing
p_pore	150[kPa]	150	Pore pressure
T_s	-30[degC]	-30	surrounding temperature
phai	0.2	0.2	Initial soil water content

7) Time stepping:

Times (in seconds): 0:600:18000

Initial time step: 0.001

The temperature profiles along the OA cross-section are shown in Figure 6-2. The results are given for the following instances (in hours): 0, 0.5, 1, 1.5, 2, 2.5, 3, 3.5,4, 4.5 and 5. The 5 locations of x1, x2, x3, x4, x5 along the x axis on the O-A cross-section are the same as defined in Section 5.1 (x1 at 5mm from center, x2 at 16mm, x3 at 27mm, x4 at 38mm, and x5 at 50mm). Locations x1, x3, and x5 (5, 27 and 50 mm) are equivalent to the thermal couple locations T1, T2 and T3, as illustrated in Figure 6-1. The simulated temperature variations at locations x1, x2 and x3 are presented in Figure 6.2 and compared with the laboratory tested values from T1, T2, and T3 thermal couples. The initial temperature of the sample was 17°C (room temperature) at 0 hours of freezing. At T1 and T2 locations, the simulated and tested results yield good agreement. At the T3 location, the simulated temperatures are lower than the temperatures measured at 2 to 4 hours of freezing. For instance, at 2.5 hours of freezing, the simulated temperature is -14°C, but the tested temperature was -5°C. This maybe because 1) the temperature measurement is more sensitive at locations near the surface or 2) the heat transfer coefficient of the boundary with a thin plastic film is not accurately quantified. Between 1 to 2 hours of freezing, the temperatures at x1, x2 and x3 are close to -0°C and maintain a steady level. Beyond the 2-hour period, the temperatures drop with the magnitude of changes from high to low displayed at x3, x2 and x1, respectively. This demonstrates the effect of latent heat during the freezing of water.

The color contours of temperature distribution are shown in Figure 6-4. The results

are given from 0.5 to 5 hours of freezing, with 0.5 hour time intervals.
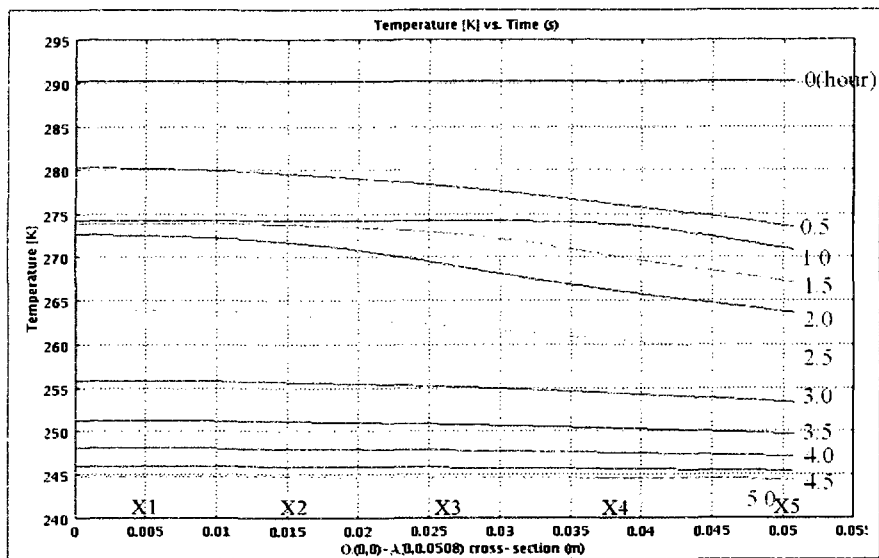
Figure 6-2. Temperature profiles of OA cross-section vs. time steps (IW simulation)
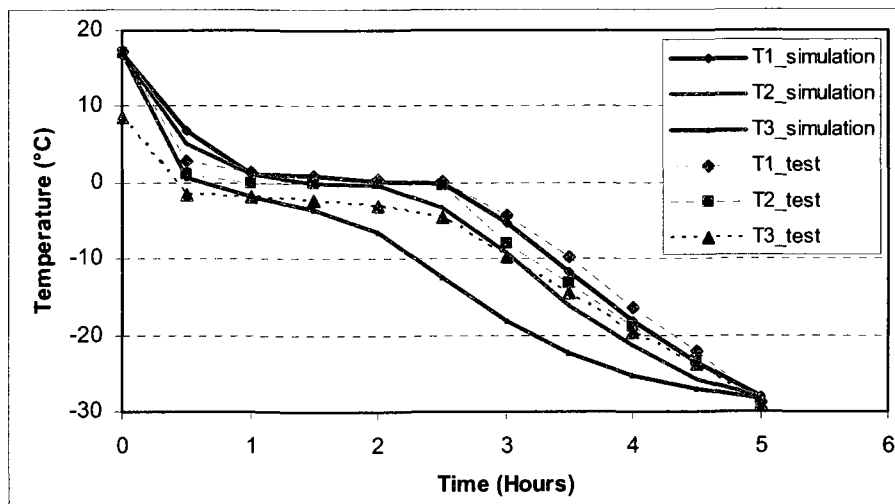
Figure 6-3. Temperature vs. time steps at 3 reference locations in IW simulation

compared with those from 3 thermal couple locations in IW laboratory test
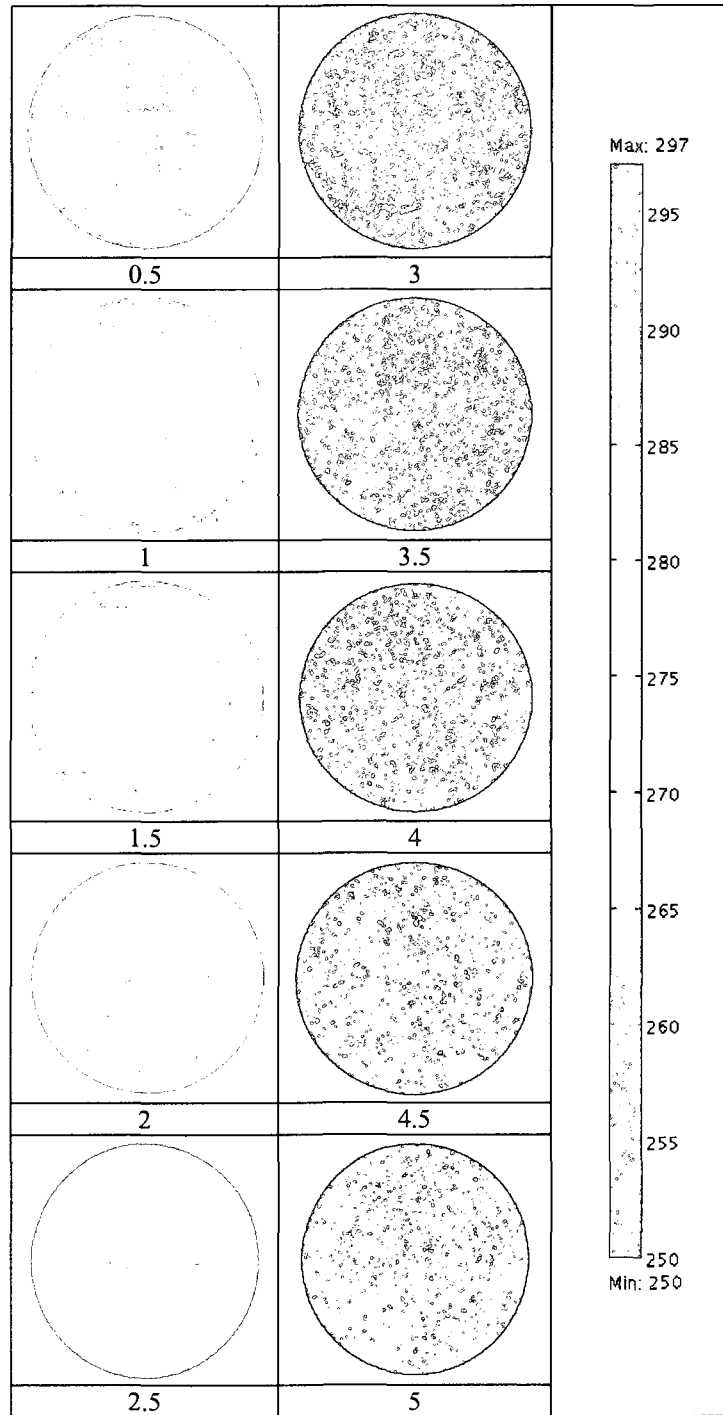
Figure. 6-4 Temperature distributions vs. time steps for IW simulation
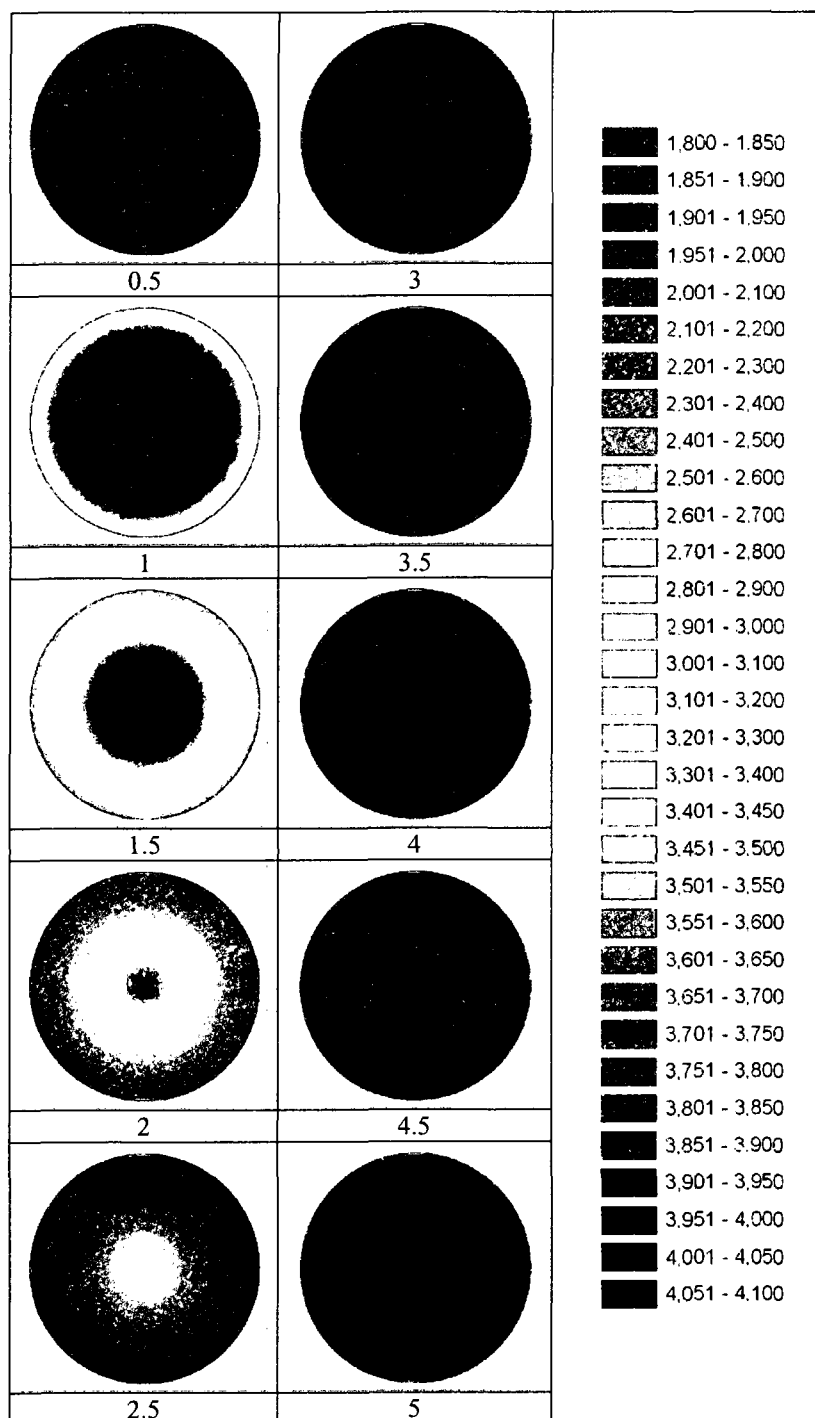
Figure 6-5. Sonic wave velocity distributions vs. time steps for IW simulation

The numerical modeling results of velocity-temperature for freezing Fairbanks silt

(FS01) are given in Section 4.4.2. The regression function is given by Eq. 4-5 as

$$Vp = 175.35Ln(-T) + 3338.2 \quad (T<0)$$

Based on this function, the outputs of temperature distributions for this IW

simulation are converted to velocity distributions using third-party image processing

software. In this study, this conversion is achieved by using the Raster Calculation

function in ArcGIS. The velocity distributions for this IW simulation are presented in

Figure 6-5. For comparison with experimental CUST scanning results, velocity profiles

of OA cross-section vs. time steps for the IW simulation are also generated and given in

Figure 6-6.
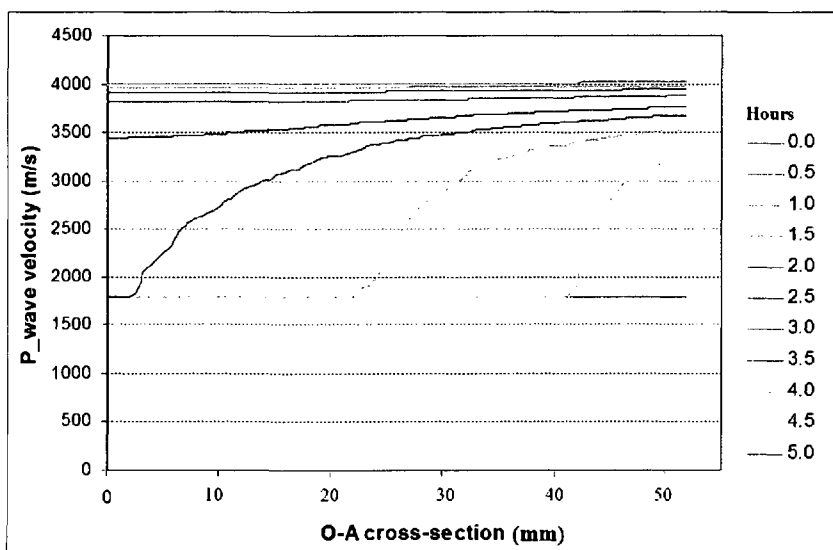
Figure 6-6. Sonic wave velocity profiles of OA cross-section vs. time steps (IW

simulation)

6.3. Dynamic frost bulb development in soil surrounding chilled pipe (OW Simulation)

In Section5.2, the cylindrical Fairbanks silt (FS_OW) specimen 10.16 cm in diameter, 15.2 cm in length and 20% moisture content was used to perform the outward dynamic freezing experiment (Figure 5-4). A copper pipe of 10mm in diameter was installed along the axis during specimen preparation. The CUST scanning plane was perpendicular to the axis, and crossed the middle section of the cylindrical specimen. Three thermal couples (T1, T2, T3) were installed on the plane 10 mm below the horizontal CUST scanning plane at the positions of 5, 0; 27, 0; and 50, 0, mm based on the Cartesian coordinates system with the origin at the center of the sample. The sample was sealed with thin plastic film to prevent the loss of moisture content. The sample was well insulated using insulation foam. The copper pipe was connected to a cold bath. The soil specimen was refrigerated by flowing cold antifreeze from the cold bath with the temperature of the antifreeze maintained at -18°C. The CUST scans were performed and recorded each 15 minutes for a total of 7 hours of freezing until no significant wave travel time changes could be observed.

For simulating this scenario, 2D geometry and mesh along the CUST scanning plane are constructed to simulate the heat flow during the freezing process (Figure 6-7). For the convenience of comparison analysis with experimental CUST, the entire circular shape is used instead of a symmetrical half-circular shape. The settings and parameters of the FEM simulation in Comsol Multiphysics are listed below:
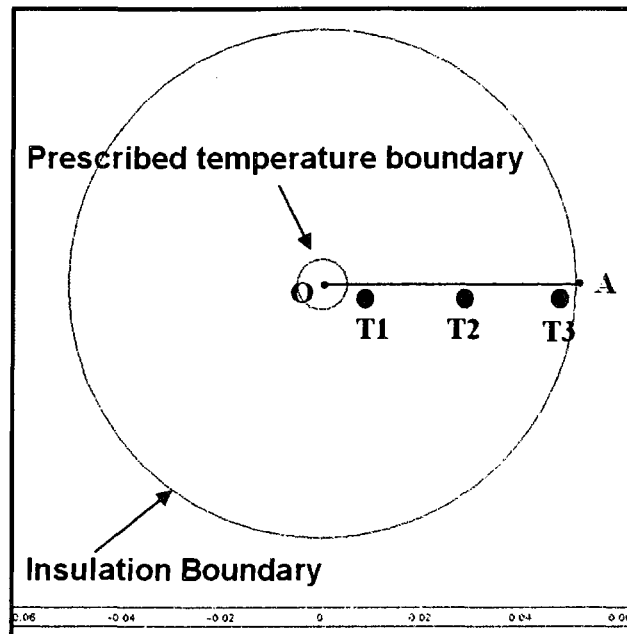
Figure 6-7. Geometry and Mesh of OW simulation

1) Model properties:

Application mode type: 2D, Conduction in Porous Media (Earth Science Module)

2) Constants:

The physical constants and coefficient used in the IW simulation for Fairbanks silt are listed in Table 6-2.

3) Variables:

Dependent variable: T (temperature)

Table 6-3. Physical constants and coefficient of Fairbanks silt

Name	Expression	Value	Description
T_trans	0.3[degC]	0.3	Freezing point
scale	0.5	0.5	Width of smoothed step function
rho_s	2700[kg/m^3]	2730	Density of grain
rho_i	920[kg/m^3]	918	Density of ice
rho_w	1000[kg/m^3]	1000	Density of water
nu0	0.29	0.29	Poisson's ratio
alpha_s	0.8e-6[1/K]	0.8e-6	Coefficient of thermal expansion
T_init	19.2[degC]	19.2	Initial temperature
k_s	1.5[W/(m*K)]	1.5	Thermal conductivity above freezing point
k_i	2.13[W/(m*K)]	2.13	Thermal conductivity of ice
k_w	0.613[W/(m*K)]	0.613	Thermal conductivity of water
Cp_s	765[J/(kg*K)]	765	Heat capacity above freezing point
Cp_i	2052[J/(kg*K)]	2052	Heat capacity of ice
Cp_w	4179[J/(kg*K)]	4179	Heat capacity of water
kappa_s	3.2e-6[m^2]	3.2e-6	Permeability, unfrozen sand
eta_s	0.001[Pa*s]	0.001	Dynamic viscosity
E0_s	93[MPa]	93	Young's modulus
dT	0.5[K]	0.5	Half width of Gauss bell curve
lam	333[kJ/kg]	333	Latent heat of freezing
p_pore	150[kPa]	150	Pore pressure
T_s	-18[degC]	-30	surrounding temperature
phai	0.2	0.2	Initial soil water content

4) Boundary settings:

Outside surface:

Type: thermal insulation

Heat transfer coefficient: 20 w/(m²·K)

External temperature: -18°C

Inside surface (copper pipe)

Type: temperature

Temperature (T0): -18°C

5) Subdomain setting:

Equivalent volumetric heat capacity:

$$C_{eq} = \frac{\sum \theta_{Li} \rho_{Li} C_{pLi} + \sum \theta_{Pi} \rho_{Pi} C_{pPi}}{\sum \theta_{Li} + \sum \theta_{Pi}} - L\rho_i \frac{\partial \theta_i}{\partial t}$$

Subdomain initial value (temperature): 19.2°C

6) Solver settings:

Analysis type: Transient

Solver: Time dependent

7) Time stepping:

Times (in seconds): 0:600:36000

Initial time step: 0.001

The temperature profiles of the OW simulation along the OA cross-section are

shown in Figure 6-8. The results are given for the following instances (in hours): 0, 0.5, 1,

1.5, 2, 2.5, 3, 3.5,4, 4.5 and 5. The naming of the 5 locations, x1, x2, x3, x4, x5, along the

x axis on the O-A cross-section (x1 at 5mm from center, x2 at 16mm, x3 at 27mm, x4 at 38mm, and x5 at 50mm) is the same as described in Section5.1. Locations of x1, x3, and x5 (5, 27 and 50 mm) are equivalent to thermal couple locations T1, T2 and T3 as shown in Figure 6-7. The simulated temperature variations at locations x1, x2 and x3 are presented in Figure 6-3 and compared with the laboratory tested values from the T1, T2, and T3 thermal couples. The initial temperature of the sample is 19.2°C (room temperature) at 0 hours of freezing. The simulated and tested results give good agreement at the three locations. At T1 (x1), both simulated and tested temperatures drop quickly to -13°C~ -14°C at 0.5 hours of freezing, because of the contact with copper pipe where the temperature is maintained at -18°C. Between 1 and 2.5 hours of freezing, the temperatures at x2 and x3 get close to 0°C and keep steady. Beyond 2.5 hours, the temperatures drops faster at x3 and x2.   This again is due to the effect of latent heat released during the water freezing. In Figure 6-9, after 2.5 hours of freezing, the tested temperatures at T2 and T3 are lower than those in the simulation. A number of factors may contribute to this difference, including the thermal properties of the soil, simulation parameters, or insulation differences.

The color contours of temperature distributions of the OW simulation are given in Figure 6-10. The results are given from 0.5 to 5 hours with 0.5 hour time intervals.

The relationship of velocity to temperature for freezing Fairbanks silt (FS01) is given by Eq. 4-5 in Section 4.4.2. Based on Eq. 4-5, the outputs of temperature distributions for this OW simulation are converted to velocity distributions using the Raster Calculation function in ArcGIS. The velocity distributions for this OW simulation are presented in

Figure 6-11. For comparison with the experimental CUST scanning result, sonic wave velocity profiles of the OA cross-section vs. time steps for the OW simulation are also generated and given in Figure 6-12. It appears that there is a minimum "cut-off" velocity of 1800m/s in the OW simulation. That's because the minimum V_p for Fairbanks silt (FS01) predicted by the modified Leclaire et al's Biot-type three-phase theory is 1800m/s.
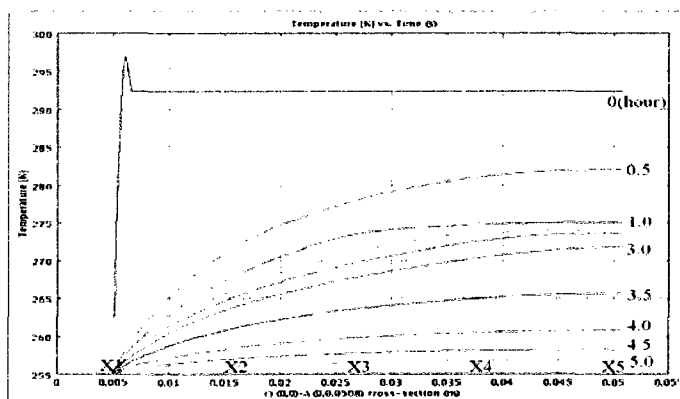
Figure 6-8. Temperature profiles of OA cross-section vs. time steps (OW simulation)
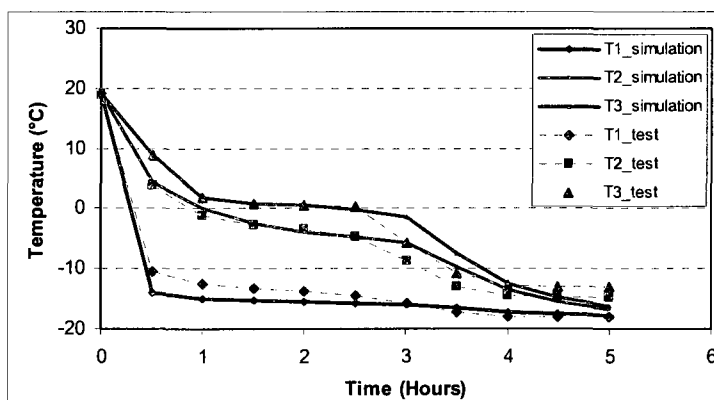
Figure 6-9. Temperature vs. time steps at 3 reference locations in OW simulation compared with those from the 3 thermal couples in OW laboratory test
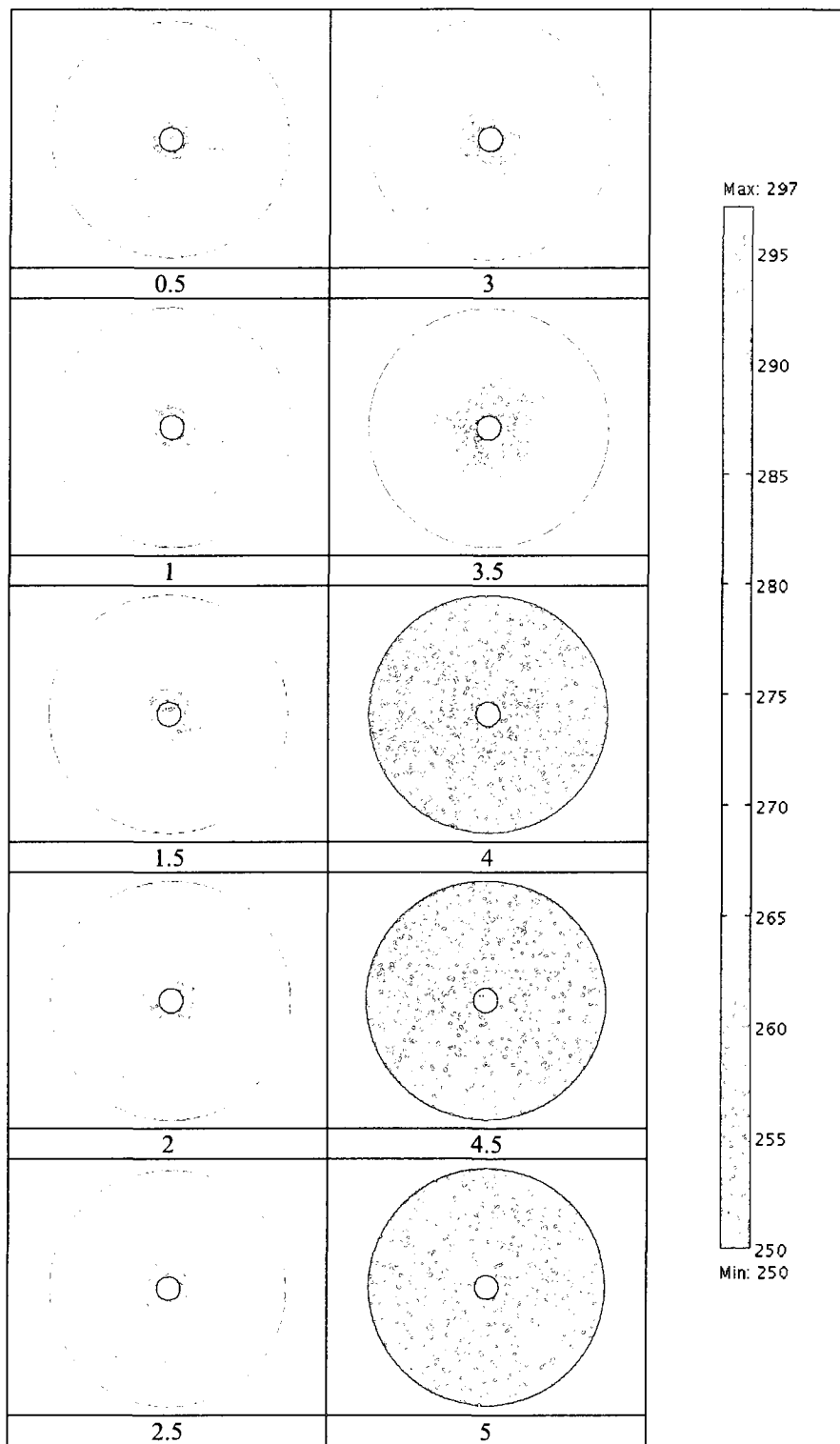
Figure 6-10. Temperature distribution vs. time steps for OW simulation
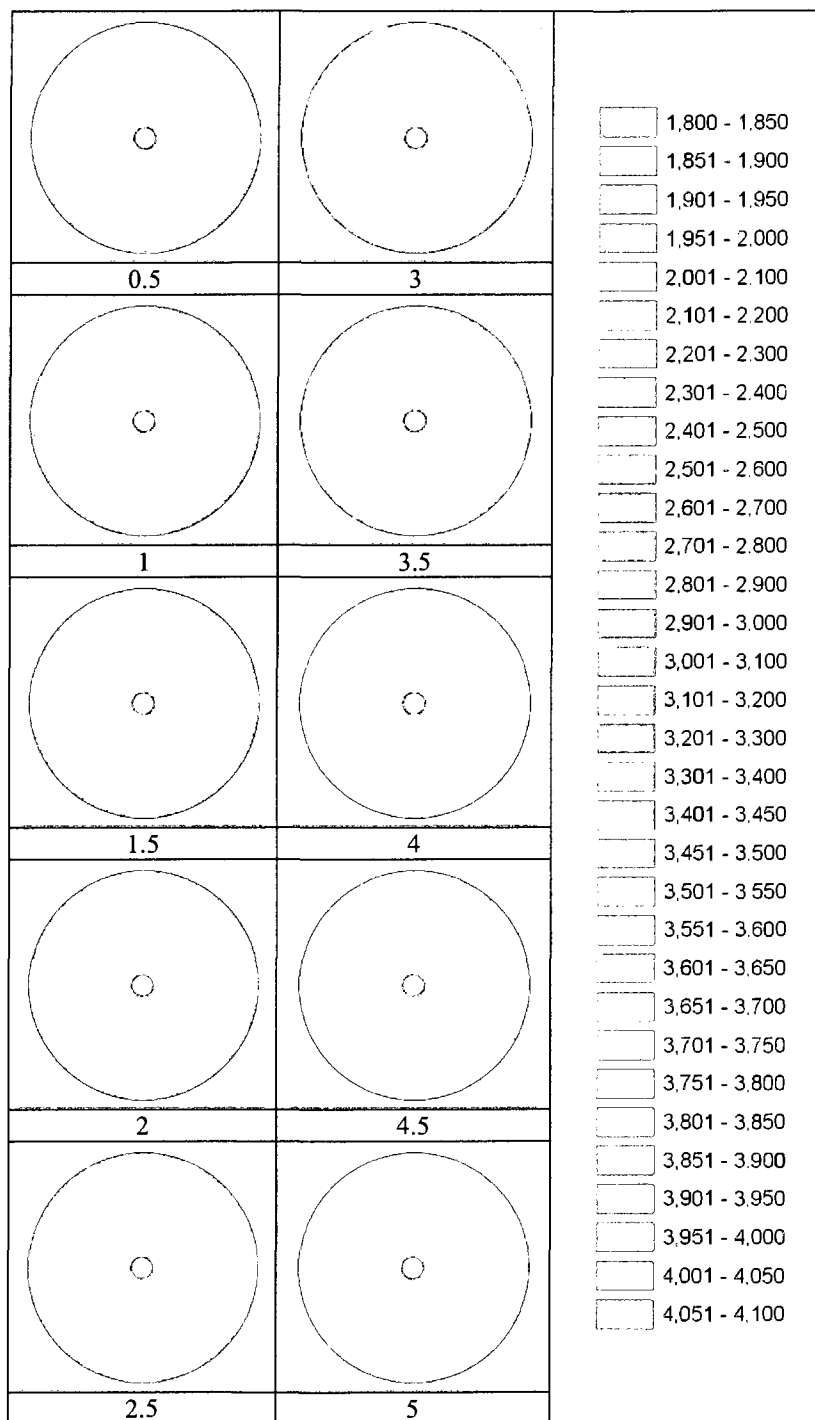
Figure 6-11. Sonic wave velocity distribution vs. time steps for OW simulation
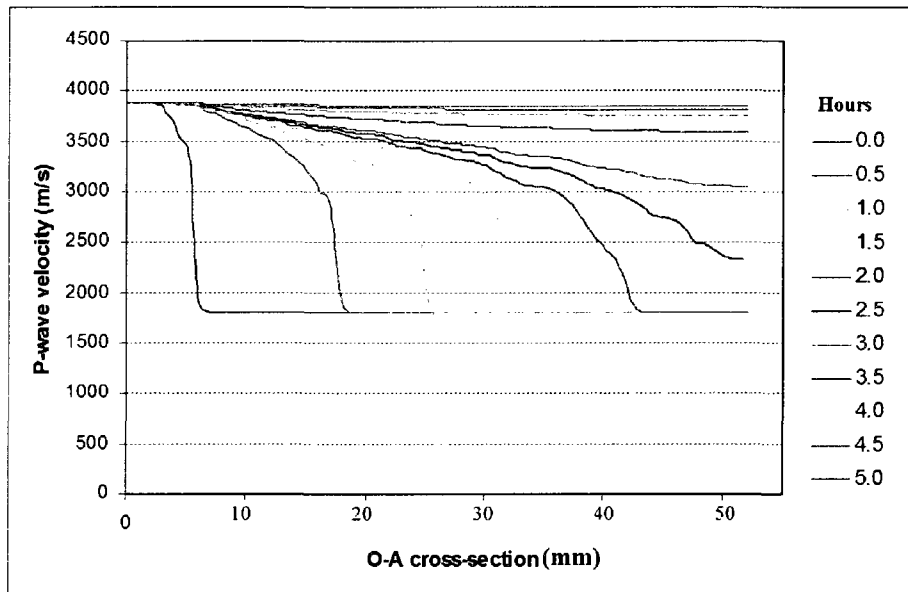
Figure 6-12. Velocity profiles of OA cross-section vs. time steps (OW simulation)

Chapter 7. Concluding Summaries and Suggestions

7.1. Concluding summaries

In this study, based on a good understanding of the acoustic properties of sand-clay mixtures and freezing soil, existing mathematical models are analyzed and modified to better characterize sonic wave propagation in frozen soil. Laboratory experiments utilizing CUST scanning were performed to observe the freezing process and the freezing front development in Fairbanks silt. Numerical simulations employing the finite element method were conducted to model and predict the characteristics of sonic wave propagation in Fairbanks silt. With a reasonably good agreement between the laboratory experiments and the numerical simulations, the following contributions are made to research on frozen soil:

1) A Multi-channel ultrasonic scanning system (MUSS) is designed, installed and programmed for the sample velocity tomography study. The system was developed in a LabVIEW programming environment. The plug and play capabilities of LabVIEW allow for upgrades of the control computer, sensors, and acquisition cards without any new programs being written. A LabVIEW first arrival time picking program is provided to filtering and magnifying waveforms, and then measuring the time of first rise as first arrival time. Velocity tomography is generated using simultaneous iterative reconstruction technique (SIRT) to perform tomographic inversions.

2) The inward and outward freezing process and freezing front development in Fairbanks silt samples are observed in laboratory experiments using MUSS. The freezing front is clearly identified in the computerized ultrasonic tomography (CUST) as a function of time and temperature. The study shows that acoustic tomography is an effective method for studying freezing processes. The method allows for simultaneous spatial and temporal measurements of freezing soil velocity variations. The method can also provide an indirect measurement of unfrozen water content variations without interfering with the freezing process.

3) Comprehensive FEM simulations, which account for the conduction in porous media, the latent heat effect, and the nonlinear thermal properties of soil, are performed on the numerical models of inward and outward freezing processes in Fairbanks silt. The UWC temperature function determined by FDR in laboratory experiments is integrated into the FEM models constructed with Comsol Multiphysics. The outputs of temperature distribution profiles as a function of time are converted to sonic wave velocity tomograms based on the temperature-sonic wave velocity function for Fairbanks silt developed using the Modified Leclaire et al's Biot-type three-phase theory. The comparative analysis of sonic velocity tomography obtained from CUST and FEM simulations shows a good agreement. It indicates that the FEM simulations can serve as an effective tool for the study of the dynamic freezing process in conjunction with the CUST technique.

4) Compared with the experimental results, Zimmerman and King's theory predicts lower P velocities and S-wave velocities. Zimmerman and King's three-phase spherical inclusion model does not account for the variation of particle sizes and shapes in the water-saturated media. The particle size distribution may not affect the moduli of frozen soil directly, but it appears to have a significant indirect effect. The unfrozen water content (UWC) at a given temperature is related to the distribution of pore spaces and hence the particle sizes. The frozen soil moduli, a key parameter to determine the sonic wave velocity, are closely related to the UWC. As a consequence, there is an indirect impact of particle sizes on sonic wave velocity. The experiments conducted in this study indicate that fine grains occupy more pore spaces and reduce the volume of pores than so coarser grains. Therefore, the effective moduli and the sonic wave velocities increase with more fines in the media materials.

5) Numerical temperature-sonic wave velocity models for reconstituted sand-clay mixtures and Fairbanks silt were constructed in Matlab based on Leclaire et al's Biot-type three-phase theory, which consider the existence of two solids (solid and ice matrices) and a liquid (unfrozen water) and assume that there is no direct contact between solid grains and ice. The theory adopts the Wood's average method for the estimation of the frozen soil moduli and the resulting values of the moduli and velocities are significantly lower than the values observed in the laboratory. This is due to the fact that Leclaire et al's theory does not account for the possible formation of a solid-ice frame when water is frozen. To bring the

solid-ice effective frame into account, the average bulk and shear moduli

estimation are modified with a proposed procedure in this study. First, the

time-average relationship is used to determine the moduli K_1 and G_1 for full ice

saturation. Second, Gassmann's equation is used to determine the moduli for the

water-filled sediment. Finally, the moduli for partial saturation are obtained by the

slowness averaging equation. This average bulk and shear moduli estimation

procedure is integrated into Leclaire et al's Biot-type three-phase theory to

replace the Wood's average model used previously. The modification gives

higher P-wave and S-wave velocities for reconstituted sand-clay mixtures and

Fairbanks silt, and the results fit experimental data well.

7.2. Suggestions for further studies

A change in the amount of unfrozen water below the freezing temperature

significantly influences soil properties such as strength, permeability, and thermal

conductivity. Furthermore, the amount of unfrozen water changes with pressure, the

surface area of soil particles, soil components, and other factors. The factors affecting the

amount of unfrozen water include specific surface area, temperature, overburden pressure,

osmotic potential of the soil solution, fine-pore geometry of mineral grains, particle-

packing geometry, and exchangeable ions. Because of the complexity of UWC in the soil

freezing process, we could not model the UWC in this study. We simply used the

experimental results in this study to model specific soil types. This limits the application

of the numerical modeling of sonic wave velocity-temperature functions and FEM

simulations to Fairbanks silt. A better understanding of UWC as a function of

temperature and freezing time may provide more accurate and complete numerical simulations.

Differences between the theoretically estimated sonic wave velocity and the experimental data may be due to several factors not considered by the modeling work conducted in the study. For instance, the chemical composition of clay, water salinity, dependence of the solid and ice moduli on temperature, and cementation between grains may all play a role in the sonic wave propagation in the media. The influence of these factors should be investigated in future work.

REFERENCES

Abo-Qudais, S., 2005, Effect of concrete mixing parameters on propagation of ultrasonic waves, Construction and Building Materials 19 (4), 257-263.

Aki, M. and Richards, PG., 1980, Quantitative seismology: Theory and methods. W.N. Freeman & Co., San Francisco.

Amin, M.H.G., Hall, LD., Chorley, R.J., and Richards, K., 1998, Infiltration into soils, with particular reference to its visualization and measurement by magnetic resonance imaging (MRI), Prog. Phys. Geogr. 22(2):135-165.

Anderson, D. M. and Morgenstern, N. R., 1973, Physics, chemistry and mechanics of frozen ground: A review, in Permafrost-the North American contribution to the 2nd International Conf. Yakutsk: National Acad. Sci., 257-295.

Anderson, D.M. and Hoekstra, P., 1965, Migration of interlamellar water during freezing and thawing of Wyoming bentonite, Soil Sci. Soc. Am. Proc. 35, 498-504.

Anderson, D.M. and Tice, A.R., 1971. Low temperature phases of interfacial water in clay-water systems. Soil Sci. Soc. Am. Proc. 35. 47-51.

Anderson, D.M. and Tice, A.R., 1972, Predicting unfrozen water contents in frozen soils from surface area measurements, Highw. Res. Rec. 393 (1972), 12–18.

Anderson, D.M. and Tice, A.R., 1973, The unfrozen interfacial phase in frozen soil water systems, Ecol. Stud. 4, 107-125.

Banthia, B.S., King, M.S., Fatt. 1., 1965. Ultrasonic shear wave velocities in rocks subjected to simulated overburden pressure and internal pore pressure. Geophysics 20, 117-121.

Barnes, D.F., 1963, A review of geophysical method for delineating permafrost, Proceedings of the International Permafrost Conference, 349-355.

Berkenhagen, J.H., Hickey, C.J., Prasad, S.N., and Romkens, M.J.M., 1998, Acoustic observation of a clay during a wetting drying cycle, In Proceedings of the Bouyoucos Conference on Agroacoustics. Third Symp.. Tishomingo, MS. 77-89.

Berryman, J.G., 1980, Confirmation of Biot's theory, Applied Physical Letters, 37, 382-384.

Berryman, J.G., 1995, Mixture theories for rock properties, in Ahrens, T. J., ed., Rock Physics and Phase Relations. A Handbook of Physical Constants, 205-228.

Beskow, G., 1935, Soil freezing and frost heaving with special applications to roads and railroads, Swedish Geological Society C, No. 375, Year Book no. 3 (translated by JO. Osterberg). In Historical Perspectives in Frost Heave Research, USA Cold Regions Research and Engineering Laboratory, Special Report 9 1-23, 41-157.

Biermans, M.B.G.M, Dijkema, K. M., and Vries, D. A., 1978, Water movement in porous media towards an ice front, Journal of Hydrology 37, 137-148.

Binley, A., Daily, W., and Ramirez, A., 1997, Detecting leaks from environmental barriers using electrical current imaging, J. Environ. Eng. Geophys. 2:11-19.

Biot, M.A., 1956a, Theory of propagation of elastic waves in a fluid saturated porous solid, I. Low frequency range. Journal of Acoustic Society of America 28: 168-178.

Biot, M.A., 1956b, Theory of propagation of elastic waves in a fluid saturated porous solid, II. High frequency range, Journal of Acoustic Society of America 28: 179-191.

Black, P.B. and Miller, R.D., 1985, A continuum approach to modeling frost heaving, In Freezing and Thawing of Soil-Water Systems (D.W. Anderson and P.J. Williams, Ed.), Technical Council on Cold Regions Engineering Monograph. New York: American Society of Civil Engineers, 36-45.

Black, P.B., 1995, Rigid ice model of secondary frost heave, USA Cold Regions Research and Engineering Laboratory, Special Report 95-12.

Blaha, P., 2002, Selected Examples of Seismic Tomography Usage in Mining and Geotechnics, Institute of Geophysics, Polish Academy of Science, M-24 (340): 215-225.

Blanchard, B. and Fremond, M., 1985, Soils frost heaving and thaw settlement. In Proceedings, Fourth International Symposium on Ground Freezing. Boston: A.A. Balkema, 209-216.

Bording, R.P., Gersztenkorn, A., Lines, L.R., Scales, J.A., and Treitel, S., 1987, Application of seismic travel-time tomography. Geophy. J. R. Astron. Soc. 90:285-303.

Bourbie, T., Coussy, O. & Zinszner, B., 1987, Acoustics of porous media, Houston: Gulf Publishing Company. 49-95.

Bridges, E., 1978, Worlds Soils, Cambridge University Press, 128.

Brutsaert, W., 1964, The propagation of elastic waves in unconsolidated unsaturated granular mediums, J. Geophys. Res. 69:243-257.

Bucur, V., 2005, Ultrasonic techniques for nondestructive testing of standing trees, Ultrasonics 43 (4), 237-239.

Campbell, J.E., 1988, Dielectric properties of moist soils at RF and microwave frequencies, Ph.D. diss. Dartmouth College, Hanover. NH (Diss. Abstr. 89-04909).

Campbell, J.E., 1990, Dielectric properties and influence of conductivity in soils at one to fifty megahertz, Soil Sci. Soc. Am. J. 54:332-341.

Carcione, J.M. and Helle, B.H., 1999, Numerical simulation of the poroviscoelastic wave equation on a staggered mesh, J. Comp. Phys., 154, 520-527.

Carcione, J.M. and Seriani, G., 1998, Seismic velocities in permafrost, Geophysical Prospecting, 46, 441-454.

Cheng, J., Li, L., Yu, S., Song, Y., Wen, X., 2001, Assessing changes in the mechanical condition of rock masses using P-wave computerized tomography, International Journal of Rock Mechanics and Mining Sciences, 38:   1065-1070.

Christensen, I.N., Wang, F. H., 1985, The influence of pore pressure and confining pressure on dynamic elastic properties of Berea sandstone, Geophysics, 50, 207-213.

Couvreur, J.F., Vervoort, A., King, M.S., Lousberg, E., and Thimus, J.F., 2001, Successive cracking steps of a limestone highlighted by ultrasonic wave propagation, Geophysical Prospecting, 49: 71-78.

Daily, W., and Owen, E., 1990, Cross Borehole resistivity tomography, Geophysics, Vol. 56, No. 8: 1228-1235.

Darrow, M.M., 2007, Experimental study of adsorbed cation effects on the frost susceptibility of natural soils, Ph.D Dissertation.

Darrow, M.M., Huang, S., and Akagawa, S., 2008, Adsorbed cation effects on the frost susceptibility of natural soils, Cold Regions Science and Technology. V55, Issue 3, P263-277.

Dash, J.G., Fu, H. and Wettlaufer, J.S., 1995, The premelting of ice and its environmental consequences, Rep. Prog. Phys. 58, 115.

Dérobert, X. and Abraham, O., 2000, GPR and seismic imaging in a gypsum quarry, Journal of Applied Geophysics, 45: 157-169.

Desai, K.P. and Moore, E.J., 1967, Well log interpretation in permafrost: Trans. Soc. Prof. Well Log Anal.

Dietrich, P., Fechner, T., and Teutsch, G., 1995, Application of tomographic methods to investigate parameters of aquifer, (In German.) Z. Dtsch. Geol. Ges. 146:161-166.

Dillon, H.B. and Andersland, O.B., 1966, Predicting unfrozen water contents in frozen soils, Can. Geotech. J. 3 (1966), 53–60.

Dines, K.A. and Lytle, R.J., 1979, Computerized Geophysical Tomography, Proceedings of the IEEE, Vol. 67, No. 7: 1065-1073.

Domenico, S.N., 1977, Elastic properties of unconsolidated porous sand reservoirs, Geophysics, 42, 1339-1368.

Everett, D.H., 1961, The thermodynamics of frost damage to porous solids, Transactions of the Faraday Society, Vol. S'7, 1541-1551.

Falls, S.D. and Young, R.P., 1998, Acoustic emission and ultrasonic-velocity methods used to characterize the excavation disturbance associated with deep tunnels in hard rock, Tectonophysics, 289: 1-15.

Falls, S.D., Young, R.P., Carlson, S.R., and Chow, T., 1992, Ultrasonic tomography and acoustic emission in hydraulically fractured Lac du Bonnet grey granite, Journal of Geophysical Research, Vol. 97, No. B5, 6867-6884.

Faraday, M., 1859, On regelation, and on the conservation of force. Philosophical Magazine 17, 162-169.

Flammer, I., Blunt, A., Leiser, A., and Germann, P., 2001, Acoustic assessment of flow patterns in unsaturated soil, J. Applied Geophysics. 46:115-128.

Friedel, M.J., Jackson, M.J., Williams, E.M., Olsen, M.S., and Westman, E., 1996, Tomographic Imaging of Coal Pillar Conditions: Observations and Implications, International Journal of Rock Mechanics and Mining Sciences and Geomechanical Abstracts, Vol. 33, No. 3: 279-290.

Frolov, A.D., 1961, Raspostranenie ul'trazubuka v merzlykh peschano glinistykh porodakh, Izv. Akad. Nauk. SSSR Ser. Geofiz., 5, 34.

Fukuda, M., 1991, Measurement of ultrasonic velocity of frozen soil near 0°C: Low Temperature Science, Series A: Physical Sciences = Teion Kagaku, Butsuri-Hen, v. 50, 83-86.

Gassmann, F., 1951, Über die elastizität poröser medien, Vierteljahrsschrift der Naturforschenden Gesellschaft in Zurich, 96, 1-23.

Gilbert, P., 1972, Iterative methods for the three-dimensional reconstruction of an object from projections, J. Theor. Biol. 36:105-117.

Gilpin, R.R., 1980, A model for the prediction of ice lensing and frost heave in soils, Water Resources Research, Vol. 16, 918-930.

Goldberg, I. and Gurevich, B., 1998, A semi-empirical velocity-porosity-clay model for petrophysical interpretation of P- and S- velocities, Geophysical Prospecting, 46, 271-285.

Goulty, N.R., 1993, Controlled-source tomography for mining and engineering applications , Seismic Tomography: Theory and Practice. London: Chapman and Hall.

Handa, Y.P., Zakrzewski, M. and Fairbridge, C., 1992, Effect if restricted geometries on the structure and thermodynamic properties of ice. J. Physics and Chemistry 96, 8594-8599.

Hanson, D.R., Vandergrift, T.L., DeMarco, M.J., and Hanna, K., 2002, Advanced techniques in site characterization and mining hazard detection for the underground coal industry, International Journal of Coal Geology, 50: 275-301.

Hartikainen, J., and M. Mikkola, 1997, General thermomechanical model of freezing soil with numerical application, In Proceedings, International Symposium on Ground Freezing and Frost Action in Soils (S. Knuts- son, Ed.). Rotterdam: A.A. Balkema, 101-105.

He, P., Zhu, Y., Zhang, J., 1993, Dynamic elastic modulus and dynamic strength of saturated frozen soil, Journal of Glaciology and Geocryology 15 (1), 170-174 (in Chinese).

Helle, H.B., Bhatt, A., and Ursin, B., 2001, Porosity and permeability prediction from wireline logs using artificial neural networks: a North Sea cased study, Geophysical Prospecting, 49, 431-444.

Henry, K.S., 2000, A review of the thermodynamics of frost heave, Tech. Rep. ERDC/CRREL TR-00-16, 19 , Cold Reg. Res. and Eng. Lab., U. S. Army Corps of Eng., Washington, D. C.

Horiguchi, K. and Miller R.D., 1980, Experimental studies with frozen soil in an ice sandwich permeameter. Cold Regions Science and Technology 3, 177-183.

Hoyer, W.A., Simmons, S.O., Spann, M. M., and Watson, A. T., 1975, Evaluation of permafrost with logs: Proc., Sot. Prof. Well Log Anal. 16th Ann. Logging Sympos., paper AA.

Inoue, I. and Kinoshita, S., 1975, Compressive strength and dynamic properties of frozen soils. Low Temperature Science 33: 243-253.

Ishizaki, T., 1995, Experimental study on unfrozen water migration in porous materials during freezing, J. Natural Disaster Science 17, 65-74.

Ishizaki, T., Maruyama, M., Furukawa, Y. and Dash, J.G., 1996, Premelting of ice in porous silica glass, J. Crystal Growth 163, 455-460.

Ishizaki, T., Yoneyama, K. and Nishio, N., 1985, X-ray technique for observation of ice lens growth in partially frozen saturated soil, Cold Regions Science and Technology 2, 213-221.

Itakura, K., Sato, K., and Ogasawara, A., 1995, Monitoring of AE Clustering Activity Prior to Main Faulting of Stressed Rock by Acoustic Tomography Technique , Fifth Conference on Acoustic Emission/Microseismic Activity in Geologic Structures and Materials, Penn State University, June 11-13, 1991, Clausthal-Zellerfeld, Germany: Trans Tech Publications, 1-17.

Ivanov, N.S., 1962, Heat exchange in permafrost, Nauka, Moscow.

Jacobs, P., Sevens, E., and Kunnen, K., 1995, Principles of computerized X-ray tomography and applications to building materials, Sci. Environ. 167:161-170.

Kane, D.L., 1997, The impact of hydrologic perturbations on Arctic ecosystems induces by climate change, Walter, C. et al. (ed.), Global Change and Arctic Terrestrial ecosystems, 63-81.

Kaplar, C.W., 1963, Laboratory determination of dynamic moduli of frozen soils and of ice, Proceedings of the International Permafrost Conference, publ. 1287, 293-301. National Research Council, National Academy of Sciences, Washington, D. C.

Kay, B.D., and E. Perfect, 1988, Heat and mass transfer in freezing soils, In Proceedings, 5th International Symposium on Ground Freezing, Rotterdam, Holland: Balkema, vol. 1, 3-21.

King, M.S., 1977, Acoustic velocities and electrical properties of frozen sandstones and shales, Canadian journal of Earth Sciences 14, 1004-1013.

King, M.S., Fatt, I., 1962, Ultrasonic shear wave velocities in rocks subjected to simulated overburden pressure, Geophysics 27, 590-598.

King, M.S., Pandit, B.I., Hunter, J.A., and Gajtani, M., 1982, Some seismic, electrical and thermal properties of sub-seabottom permafrost from the Beaufort Sea, in French, H. M., Ed., Proc. 4th Canadian Permafrost Conf.: Nat. Res. Comic. Can., 268-273.

King, M.S., Zimmerman, R.W. and Corwin, R.E., 1988, Seismic and electrical properties of unconsolidated permafrost, Geophysical Prospecting 36, 349-364.

Kolaian, J.H. and Low, P.F., 1963, Calorimetric determination of unfrozen water in montmorillonite pastes, Soil Sci. 95, 376–384.

Kolsky, H., 1963, Stress Waves in Solids, 54-65. Dover, New York.

Konrad, J.M., 1980, Frost heave mechanics, Ph. D. Thesis, University of Edmonton, Alberta, 472.

Kozlowski, T., 1995, Influence of temperature and total water content on the unfrozen water content below 0 °C in the model soils, Arch. Hydro-Eng. Environ. Mech. XLIII (3-4), 51-70.

Krajewski, C., Dresen, L., Gelbke, C., and Ruter, H., 1989, Iterative tomography methods to locate seismic low-velocity anomalies: A model study, Geophys. Prospect. 37:717—751.62:1319-1338.

Kurfurst, P.J., 1976, Ultrasonic wave measurements on frozen soils at permafrost temperatures, Canadian journal of Earth Sciences 13, 1571-1576.

Kuster, G.T. and Toksöz, M.N., 1974, Velocity and attenuation of seismic waves in two-phase media: Part II: Experimental results, Geophysics 39, 607-618.

Kuster, G.T. and Toksöz, M.N., 1974, Velocity and attenuation of seismic waves in two-phase media. Part I: Theoretical formulations: Geophysics, 39, 587-606.

Kuyala, K., 1989, Unfrozen water content of Finnish soils measured by NMR, Proc. "Frost in Geotechnical Engineering", VTT Symposium 94. VII, Espoo, 301-310.

Ladanyi, B. and Shen, M., 1989, Mechanics of freezing and thawing in soils, Proc., International Symposium on Frost in Geotechnical Engineering, Saariselka, Finland, 94, 73-104.

Leclaire, Ph., Cohen-Tenoudji, E., and Aguirre-Puente, J., 1994, Extension of Biot's theory of wave propagation to frozen porous media, journal of the Acoustical Society of America 96, 3753-3768.

Leclaire, Ph., Cohen-Tenoudji, E., and Aguirre-Puente, J., 1995, Observation of two longitudinal and two transverse waves in a frozen porous medium, journal of the Acoustical Society of America 97, 2052-2055.

Loch, J.P.G. and Kay B.D., 1978, Water redistribution in partially frozen, saturated silt under several temperature gradients and overburden lads, Soil Sci. Soc. Am., Proc. 12, 400-406.

Loch, J.P.G., 1978, Thermodynamic equilibrium between ice and water in porous media, Soil Science, 126(2): 77-80.

Mackay, J.R., 1993, Air temperature, snow cover, creep of frozen ground, and the time of ice-wedge cracking, western Arctic coast. Canadian J. Earth Sci. 30, 1720-1729.

Mackenzie, J.K., 1950, The elastic constants of a solid containing spherical holes: Proc. Phys. Soc. London. B63, 2-11.

Malinský, K., 1996, Ultrasonic investigations in a coal mine, Ultrasonics, 34: 421-423.

Marti, D., Carbonell, R., 2002, Try Calibrating 3D tomograms of a granitic pluton, Geophysical Research Letters, 29, No. 17: 151-154.

Merserau, R.M. and Oppenheimer, A.V., 1974, Digital reconstruction of multi-dimensional signals from their projections, Proc. IEEE.

Michalowski, R.L., 1992, A constitutive model for frost- susceptible soils, In Proceedings of the Fourth International Symposium on Numerical Models in Geomechanics. Rotterdam: A.A. Balkema, 159-167.

Michalowski, R.L., 1993, A constitutive model of saturate soils for frost heave simulations. Cold Regions Science and Technology, Vol. 22, 47-63.

Michelena, R.J. and Harris, J.M., 1991, Tomographic travel time inversion using natural pixels, Geophysics 56:635-644.

Miller, R.D., 1978, Frost heaving in non-colloidal soils, Third International Conference of Permafrost Proceedings, Ottawa, Vol. 1, pp 708–713. National Research Council, Canada.

Miller, R.D., Baker, J.H., and Kolaian, J.H., 1960, Particle size, overburden pressure, pore water pressure and freezing temperature of ice lenses in soil. In Proceedings, 7th International Congress of Soil Science, Madison, Wisconsin, 122-129.

Miller, R.D., Loch, J.P.G., and Bresler, E., 1975, Transport of water and heat in a frozen permeameter. Soil Science Society of America Proceedings, Vol. 39, No. 6, 1029-1036.

Minshull, T.A., Singh, S.C., and Westbrook, G.K., 1994, Seismic velocity structure at a gas hydrate reflector offshore western Colombia, from full waveform inversion, journal of Geophysical Research 99, 4715-4734.

Mohamed, A.M.O., Yong, R.N. and Mazus, M.T., 1995, Contaminant migration in engineered clay barriers due to heat and moisture redistribution under freezing conditions, Canadian Geotechnical J. 32, 40-59.

Molyneux, J.B. and Schmitt, D.R., 1999, First-break timing: Arrival onset by direct correlation, Geophysics, Vol. 64, No. 5: 1492-1501.

Müller, G., 1961, Geschwindigkeitsbestimmungen elastischer wellen in gefrorenen Gesteinen und die Anwendung akustischer Messungen auf Untersuchungen des Frostmantels an Gefrierschächten, Geophys. Prosp., v. 9, no. 2, 279-295.

Nakano, Y., Arnold, R., 1973, Acoustic properties of frozen Ottawa sand, Water Resources Research 9 (1), 178-184.

Nakano, Y., Martin, A.J., and Smith, M., 1972, Ultrasonic velocities of the dilatational and shear waves in frozen soils, Water Resources Research 8(4): 1024-1030.

Nixon, J.F., 1987, Thermally induced heave beneath chilled pipelines in frozen ground. Canadian Geotechnical J. 24, 260-266.

Nixon, J.F., 1991, Discrete ice lens theory for frost heave in soils, Canadian Geotechnical J. 28, 843-859.

Nolet, G. (Ed.), 1987, Seismic Tomography: With Applications in Global Seismology and Exploration Geophysics. Boston, MA: D. Reidel Publishing Co.

Pandit, B.I., and King, M.S., 1979, A study of the effects of pore-water salinity on some physical properties-of sedimentary rocks at permafrost temperatures: Can. J. Earth Sci., 16, 1566-1580.

Phillips, S.W., and Fehler, M.C., 1991, Travel time tomography: A comparison of popular methods, Geophysics 56(10):1639-1649.

Plocek, J., 1996, Equipment for ultrasonic investigation in mines , Ultrasonics, 34: 425-430.

Plona, T.J. and Johnson, D.L., 1980, Experimental study of the two compressional modes in water-saturated porous structures, Proc. IEEE Ultrason. Symp. 868-871.

Pusch, R., 1979, Unfrozen water as a function of clay microstructure. Engineering Geology, 13(1-4), 157-162.

Radd, T. and Oertle, D.H., 1973, Experimental pressure studies of frost heave mechanisms and growth fusion behavior of ice, In Proceedings, 2nd International Conference of Permafrost, 409.

Radon, J., 1917, Determination of functions by their integral-values along certain manifolds, (In German.) Ber. Sachsischer Akad. Wissenschaft 69:262-277.

Reuss, A., 1929, Berechnung der Fleissgrenze von Mischkristalen auf Grund der Plastizitats belingung für EinKristafle. Z. Angew. Math. Mech. 9, 49-58.

Robinson, E.A., 1982, Spectral approach to geophysical inversion by Lorentz, Fourier and Radon transformation. Proceedings of the IEEE 70: 1039-1054.

Rose, J., 1999, Ultrasonic Waves in Solid Media, Cambridge University Press, Cambridge, UK.

Schön, J.H., 1996, Physical Properties of Rocks, Fundamentals and Principles of Petrophysics, Pergamon Press, Inc.

Scott, D.F., Williams, T.J., Denton, D.K., and Friedel, M.J., 1999, Seismic tomography as a tool for measuring stress in mines, Mining Engineering, 77-80, January.

Scott, T.E., Ma, Q., Roegiers, J.C., and Reches, Z., 1994, Dynamic stress mapping utilizing ultrasonic tomography , Rock Mechanics, Nelson and Laubach (eds.), Balkema, Rotterdam, 427-434.

Seebold, I., Lehmann, B., Arribas, A., Ruiz, C., Shepherd, T.J., and Ashworth, K.L., 1999, Development of tomographic systems for mining, mineral exploration, and environmental purposes , Transactions of the Institution of Mining and Metallurgy, Section B: Applied Earth Science, 108: B105-B118.

Semandeni, T.J., Calder, P.N., 1990, High frequency microseismic monitoring applied to the determination of stress levels in hard rock mines, Rockbursts and Seismicity in Mines, Fairhurst (ed.).

Seyfried, M.S. and Murdock, M.D., 2002, Effects of soil type and temperature on soil water measurement using a soil dielectric sensor, 1-13. In I.C. Paltineanu (ed.) First international symposium on soil water measurement using capacitance and impedance. Beltsville. MD. 6-8 Nov.

Seyfried, M.S., Murdock, M.D., 2004, Measurement of Soil Water Content with a 50 MHZ Soil Dielectric Sensor, Soil Science Society of America Journal, Vol.68, pp 394-403.

Sheng, B., 1994, Thermodynamics of freezing soils: Theory and application. Doctoral thesis 141 D, Lulea University of Technology, 201.

Sheng, Y. and Fukuda, M., 1998, Characteristics of ultrasonic velocities through frozen soil. Proceedings of the 1998 Conference on Japanese Society of Snow and Ice, Shiozawa, Japan: 57.

Sheng, Y., Fukudu, M., Kim, H., 2000a, Effect of unfrozen water content on the ultrasonic velocities in tire-mixed frozen soils. Chinese Journal of Geotechnical Engineering 22 (6), 716-720 (in Chinese).

Sheng, Y., Fukuda, M., Kim, H., 2000b, Strength behavior of frozen silt mixed with tire powder. Journal of Glaciology and Geocryology 22 (suppl.): 204-206.

Sheng, Y., Peng, W., Wen, Z., 2003, Physical properties of frozen soils measured using ultrasonic techniques. In Proceedings, International Conference on Permafrost 2003.

Smith, M.W. and Tice, A.R., 1988, Measurement of the unfrozen water content of soils - comparison of NMR and TDR methods, CRREL Report vol. 88-18, US Army Cold Regions Research and Engineering Lab (CRREL).

Song, L., Liu, H., Chun, S., Song, Z., and Zhang, S., 1998, Mapping an underground rock mass by anisotropic acoustical transmission tomography, Ultrasonics, 52: 1009-1012.

Song, L., Suh, M., Woo, Y., Hao, T., 2004, Determination of the elastic modulus set of foliated rocks from ultrasonic velocity measurements. Engineering Geology (72), 293-308.

Spaans, E.J.A. and Baker, J.M., 1995, Examining the use of TDR for measuring liquid water content in frozen soils. Water Resources Research 31, 2917-2925.

Taber, S., 1929, Frost heaving, Journal of Geology, vol. 37, 428-461. Historical Perspectives in Frost Heave Research, USA Cold Regions Research and Engineering Laboratory, Special Report 91-23, 9-26.

Taber, S., 1930, The mechanics of frost heaving, Journal of Geology, Vol. 38, 303-3 17. In Historical Perspectives in Frost Heave Research, USA Cold Regions Research and Engineering Laboratory, Special Report 91-23, 29-35.

Takashi, T., Masuda, M., and Yamamoto, H., 1974, Experimental study on the influence of freezing speed upon frost heave of soil under constant effective stress (in Japanese). J. Japan. Soc. Snow and Ice 36, 49-67.

Terada, M., and Yanagidani, T., 1986, Application of Ultrasonic Computer Tomography to Rock Mechanics . Ultrasonic Spectroscopy and its applications to material science (1986): 205-210.

Thimus, J.F., Aguirre-Puente, J., Cohen-Tenoudji, F., 1991, Determination of unfrozen water content of an overconsolidated clay down to -160°C by sonic approaches comparison with classical methods, Ground Freezing, vol. 91. Balkema, Rotterdam, 83-88.

Tice, A.R. and Oliphant, J.L., 1984, The effects of magnetic particles on the unfrozen water content of frozen soils determined by nuclear magnetic resonance. Soil Science 138, 63-73.

Tice, A.R., Anderson, M.D.M., Sterrett, K.F., 1982, Unfrozen water contents of submarine permafrost by nuclear magnetic resonance, Selected Papers of the 2nd lot. Symp. on Ground Freezing, Elsevier, Amsterdam, 135-146.

Tice, A.R., Oliphant, J.L., Nakano, Y. and Jenkins, T.F., 1982, Relationship between the ice and unfrozen water phases in frozen soil as determined by pulsed nuclear magnetic resonance and physical desorption data. CRREL Report 82, 8.

Timur, A., 1968, Velocity of compressional waves in porous media at permafrost temperatures, Geophysics 33, 584-595.

Topp, G.C., and Davis, J.L., 1985, TDR and its application to irrigation scheduling. Advances in Irrigation, 107-127.

Topp, G.C., Davis, J.L., Annan, A.P., 1980, Electromagnetic determination of soil water content: measurements in coaxial transmission lines, Water Resources Research 16, 574-582.

Trampert, J., Leveque, J.J., 1990, Simultaneous iterative reconstruction technique: physical interpretation based on the generalized least squares solution, J. Geophysics. Res. 95, 12553–12559.

Villaescusa, E., Seto, M., and Baird, G., 2002, Stress measurements from oriented core, International Journal of Rock Mechanics and Mining Sciences, 39, 603-615.

Vitel. Inc., 1994, Hydra soil moisture probe user's manual, Ver. 1.2. Vitel Inc., Chantilly. VA.

Voigt, W., 1928, Lehrbuch der Kristallphysik. B.G. Terbner, Leipzig.

Votyakov, I.N., 1975, Physico-mechanical Properties of Frozen and Thawing Soils in Yakutia, Nauka. Novosibirsk, Russia.

Wang, D.Y., Zhu, Y.L. Ma, W, Niu, Y.H., 2006, Application of ultrasonic technology for physical-mechanical properties of frozen soils, Cold regions science and technology, 2006, vol. 44, No.1, 12-19.

Wang, K., Monteiro, B.J.M., Rubinsky, B., and Arav, A., 1996, Microscopic study of ice propagation in concrete. ACI Materials Journal, 370-377.

Washburn, A.L., 1980, Geocryology. John Wiley & Sons, New York, 18-41.

Wettlaufer, J.S. and Worster M.G., 1995, Dynamics of premelted films: Frost heave in a capillary, Physical Review E 51, 4679-4689.

White, J.E., 1965, Seismic Waves, Radiation, Transmission and Attenuation, McGraw-Hill Book Co.

Wood, A.B., 1941, A Textbook of Sound. G. Bell & Sons, Ltd, London. Wyllie M.R.J.

Worthington, M.H., 1984, An introduction to geophysical tomography, First Break 2(11): 20-26.

Wyllie, M.R.J., Gregory, A.R., and Gardner, L.W., 1956, Elastic waves velocities in heterogeneous and porous media, Geophysics 21 (1956) (1), 41–70

Wyllie, M.R.J., Gregory, A.R., and Gardner, L.W., 1958, An experimental investigation of factors affecting elastic wave velocities in porous media, Geophysics 23 (1958) (3), 459–493.

Yoshikawa, K. and Overduin, P.P., 2005, Comparing unfrozen water content measurements of frozen soil using recently developed commercial sensors. Cold Regions Science and Technology, Vol. 42, Issue 3, November 2005, 250-256.

Zhou, Q.Y., Shimada, J., and Sato, A., 2001, Three-dimensional spatial and temporal monitoring of soil water content using electrical resistivity tomography, Water Resour. Res. 37:273-285.

Zimmerman, R.W. and King, M.S., 1986, The effect of the extent of freezing on seismic velocities in unconsolidated permafrost, Geophysics 39, 587-606.

Zykov, I.U.D., 1966, Ultrasonic methods used in the study of elastic properties of frozen ground samples, Merzlotnye Issled., 5, 184-198.

Appendixes

Appendix A: Summary of notation and symbols

Symbol	Definition	Expression
ϕ_s	Proportion of solid	
ϕ_w	Proportion of water	
ϕ_i	Proportion of ice	
ρ_s	Density of solid	
ρ_w	Density of water	
ρ_i	Density of ice	
K_s	Bulk modulus of solid	
K_w	Bulk modulus of water	
K_i	Bulk modulus of ice	
K_a	Bulk modulus of air	
K_{sm}	Bulk modulus of the matrix formed by the solid phase	
K_{KT}	Kuster-Toksöz's bulk modulus	$\dfrac{K_{KT}}{K_i} = \dfrac{1+[4\mu_i(K_a - K_i)/((3K_a + 4\mu_i)K_i)]\phi_s}{1-[3(K_a - K_i)/(3K_a + 4\mu_i)]\phi_s}$
K_{im}	Bulk modulus of the matrix formed by ice	$K_{KT}[\phi_i/(1-\phi_s)]^{3.8}$
c_1	Consolidation coefficient for solids	$K_{sm}/\phi_s K_s$
c_3	Consolidation coefficient for ice	$K_{im}/\phi_i K_i$
K_{av}	Average bulk modulus	$[(1-c_1)\phi_s/K_s + \phi_w/K_w + (1-c_3)\phi_i/K_i]^{-1}$
μ_s	Shear modulus of solid	
μ_i	Shear modulus of ice	
μ_{sm}	Shear modulus of the matrix formed by the solid phase	
μ_{KT}	Kuster-Toksöz's shear modulus	$\dfrac{\mu_{KT}}{\mu_i} = \dfrac{(6K_i + 12\mu_i)\mu_a + (9K_i + 8\mu_i)[(1-\phi_s)\mu_i + \phi_s\mu_a]}{(9K_i + 8\mu_i)\mu_i + (6K_i + 12\mu_i)[(1-\phi_s)\mu_a + \phi_s\mu_i]}$
μ_{im}	Shear modulus of the matrix formed by ice	$\mu_{KT}[\phi_i/(1-\phi_s)]^{3.8}$
k_{s0}	Permeability of solid matrix	
k_{i0}	Permeability of ice matrix	
ω	Angular frequency	$2\pi f$
T	Water temperature in degrees Celsius	

$\overline{\eta}_w$	Viscosity of free water	$1.798\times10^{-3}\exp(-0.03753T)$ (MKS units)
h	Average thickness of the unfrozen water layer	$r_s[(1+\phi_w/\phi_s)^{1/3}-1]$
η_w	Viscosity of interstitial water	$\overline{\eta}_w(450+h)/h$, with
χ		$(h/2)(\omega\rho_w/\eta_w)^{0.5}$
$\mathrm{Re}[F(\chi)]$		$1+(1/0.7178)\exp[0.7178(\chi-3.2)]/12$; if $\chi\leq3.2$
$\mathrm{Re}[F(\chi)]$		$0.5+\{2\chi+\exp[-0.7178(\chi-3.2)]\}/12$; if $\chi\geq3.2$
$\mathrm{Im}[F(\chi)]$		$\chi/6$
η_D	Dynamical viscosity of interstitial water	$\eta_w F(x)$, with
g_1	Consolidation coefficient for solids	$\mu_{sm}/\phi_s\mu_s$
g_3	Consolidation coefficient for ice	$\mu_{im}/\phi_i\mu_i$
μ_{av}	Average shear modulus	$[(1-g_1)\phi_s/\mu_s+\phi_w/2\omega\eta_w+(1-g_3)\phi_i/\mu_i]^{-1}$
r_{12}	Geometrical aspect of the boundary separating solid from water	
r_{23}	Geometrical aspect of the boundary separating ice from water	
r_s	Average radius of solid grains	
r_{av}	Average radius of the capillary pore	
Δ_r	Standard deviation of the capillary pore	
D10	Effective grain size	d_{10} = the maximum grain size of the smallest 10% of the sample
V_p	Longitudinal wave velocity	
V_s	Transverse wave velocity	

Appendix B: Biot-type three-phase theory of frozen porous medium

In Leclaire et al's Biot-type three-phase theory, Leclaire et al. (1994) assumed that there is no direct mechanical contact between solids and ice because they are separated by water. In the following expressions, the effective solid, the unfrozen water as an effective fluid, and the ice as a second effective solid will sometimes be designated, respectively, by the term solids, water, and ice. The indices 1, 2, and 3 will be used, respectively, to refer to solids, water, and ice in the formulas.

1) Potential energy density V

When an elastic wave propagates, the porous medium is submitted to local deformations and temperature variations; the energy function used to describe these phenomena should be free energy. However, for small temperature variations, the potential energy $V(\varepsilon_{ij}^{(1)}, \varepsilon_{ij}^{(2)}, \varepsilon_{ij}^{(3)})$ can be considered as elastic energy and depends only on the strain tensors of solids $\varepsilon_{ij}^{(1)}$, of water $\varepsilon_{ij}^{(2)}$, and of ice $\varepsilon_{ij}^{(3)}$. The strain tensors are written as functions of the displacement vectors u_1, u_2, and u_3. For solids and ice,

$$\varepsilon_{ij}^{(1)} = \frac{1}{2}(gradu_1 + grad^T u_1)$$ and

$$\varepsilon_{ij}^{(3)} = \frac{1}{2}(gradu_3 + grad^T u_3)$$

where $grad$ is the space derivative operator with respect to the three space coordinates and $grad^T$ is the transposed operator. Since water is statistically isotropic

and without shear deformations, its strain tensor is diagonal and can be expressed with

the first invariant $\theta_2 = \varepsilon_{kk}^{(2)}$, is called the dilation (Einstein's convention of summation on

repeated indices is used):

$$\varepsilon_{ij}^{(2)} = \begin{pmatrix} \theta_2\!\big/\!_3 & 0 & 0 \\ 0 & \theta_2\!\big/\!_3 & 0 \\ 0 & 0 & \theta_2\!\big/\!_3 \end{pmatrix}$$

For small deformations from the equilibrium state generally associated with elastic

waves and in absence of external forces, the problem is linearized, developing V to the

second order:

$$V(\varepsilon_{ij}^{(1)},\theta_2,\varepsilon_{ij}^{(3)}) = V(0,0,0) + \frac{1}{2}\frac{\partial^2 V}{\partial \varepsilon_{ij}^{(1)}\partial \varepsilon_{kl}^{(1)}}\varepsilon_{ij}^{(1)}\varepsilon_{kl}^{(1)} + \frac{1}{2}\frac{\partial^2 V}{\partial \theta_2^2}\theta_2^2 + \frac{1}{2}\frac{\partial^2 V}{\partial \varepsilon_{ij}^{(3)}\partial \varepsilon_{kl}^{(3)}}\varepsilon_{ij}^{(3)}\varepsilon_{kl}^{(3)}$$

$$+ \frac{\partial^2 V}{\partial \varepsilon_{ij}^{(1)}\partial \theta_2}\varepsilon_{ij}^{(1)}\theta_2 + \frac{\partial^2 V}{\partial \varepsilon_{ij}^{(3)}\partial \theta_2}\varepsilon_{ij}^{(3)}\theta_2 + O^3(\varepsilon_{ij}^{(1)},\theta_2,\varepsilon_{ij}^{(3)})$$

(Eq. B-1)

We may define a fourth-order tensor of elastic coefficients for solids (indice 1) and

for ice (indice 3) and an elastic coefficient for water (indice 2):

$$C_{ijkl}^{(1)} = \frac{\partial^2 V}{\partial \varepsilon_{ij}^{(1)}\partial \varepsilon_{kl}^{(1)}}, \quad C_{ijkl}^{(3)} = \frac{\partial^2 V}{\partial \varepsilon_{ij}^{(3)}\partial \varepsilon_{kl}^{(3)}} \quad \text{and} \quad K_2 = \frac{\partial^2 V}{\partial \theta_2^2}$$

(Eq. B-2)

Two crossed terms appear in the development defining two second-order tensors of

elastic coupling coefficients:

$$C_{ij}^{sw} = \frac{\partial^2 V}{\partial \varepsilon_{ij}^{(1)}\partial \theta_2} \quad \text{and} \quad C_{ij}^{iw} = \frac{\partial^2 V}{\partial \varepsilon_{ij}^{(3)}\partial \theta_2}$$

(Eq. B-3)

These crossed terms describe, respectively, the exchange of elastic energy between solids and water and between ice and water. As an elastic wave propagates, the effective phases are submitted to the same macroscopic stresses, but the resulting deformations of each phase are different since their rigidities are different. However, the effective phases fill the same space at macroscopic scale, so the deformation of one phase can be transmitted to another one. This phenomenon, designated as elastic coupling, tends to be higher in a medium with a high specific area because it depends on the total area separating the phases. The crossed term relating the deformations of solids and of ice is missing in Eq. (B-1), according to the assumption on the absence of direct mechanical contact between these phases.

Disregarding the elastic coupling and using the definitions (B-2), the energy contribution of solids and ice in expression (B-1) are, respectively, given by

$$V_1 = \frac{1}{2} C_{ijkl}^{(1)} \varepsilon_{ij}^{(1)} \varepsilon_{kl}^{(1)} \quad \text{and} \quad V_3 = \frac{1}{2} C_{ijkl}^{(3)} \varepsilon_{ij}^{(3)} \varepsilon_{kl}^{(3)}$$

The phases being statistically isotropic, $C_{ijkl}^{(1)}$ and $C_{ijkl}^{(3)}$ can be expressed with only two independent coefficients and the expression of V_1 and V_3 can be simplified as

$$V_1 = \mu_1 d_1^2 + \frac{1}{2} K_1 \theta_1^2 \quad \text{and} \quad V_3 = \frac{1}{2} K_3 \theta_3^2 + \mu_3 d_3^2 \,,$$

where K_1 and μ_1 are, respectively, the bulk and shear moduli of the effective solid. Here, d_1 and θ_1 are the invariants of the strain tensor and are called the deviator and the dilatation (with $d_{ij}^{(1)} d_{ij}^{(1)} = d_1^2$ and $\varepsilon_{ii}^{(1)} \varepsilon_{jj}^{(1)} = \theta_1^2$). Analogous parameters are defined for

ice. The phases being isotropic and water having a zero shear modulus, it can be shown

that the tensors of coupling coefficients can be reduced to two coefficients: one denoted

c_{12} for the solid-water elastic coupling and the other c_{23} for the ice-water elastic

coupling. Finally, the potential energy density is expressed as

$$V = \mu_1 d_1^2 + \frac{1}{2}K_1\theta_1^2 + C_{12}\theta_1\theta_2 + \frac{1}{2}K_2\theta_2^2 + C_{23}\theta_2\theta_3 + \frac{1}{2}K_3\theta_3^2 + \mu_3 d_3^2$$

(Eq. B-4)

Stress-strain relationships

For infinitesimal deformations, the variation of potential energy may be expressed by

a differential form:

$$dV = \frac{\partial V}{\partial \varepsilon_{ij}^{(1)}} d\varepsilon_{ij}^{(1)} + \frac{\partial V}{\partial \theta_2} d\theta_2 + \frac{\partial V}{\partial \varepsilon_{ij}^{(3)}} d\varepsilon_{ij}^{(3)}$$

(Eq. B-5)

This expression allows the definition of a stress tensor for each phase:

$$\sigma_{ij}^{(1)} = \frac{\partial V}{\partial \varepsilon_{ij}^{(1)}} \quad , \quad \sigma^{(2)} = \frac{\partial V}{\partial \theta_2} \quad \text{and} \quad \sigma_{ij}^{(3)} = \frac{\partial V}{\partial \varepsilon_{ij}^{(3)}}$$

(Eq. B-6)

Using the definitions (B-6) and the expression (B-4) of potential energy, the

stress-strain relationships are expressed as

$$\sigma_{ij}^{(1)} = 2\mu_1 d_{ij}^{(1)} + (K_1\theta_1 + C_{12}\theta_2)\delta_{ij}$$

(Eq. B-7a)

$$\sigma^{(2)} = C_{12}\theta_1 + K_2\theta_2 + C_{23}\theta_3$$

(Eq. B-7b)

$$\sigma_{ij}^{(3)} = 2\mu_3 d_{ij}^{(3)} + (K_3\theta_3 + C_{23}\theta_3)\delta_{ij}$$

(Eq. B-7c)

where δ_{ij} is Kronecker's symbol. It may be noticed that the deformations of solids and of ice do not appear simultaneously in Equation (B-7a) and (B-7c), in accordance with the assumption of absence of direct contact between these two phases. The elastic coefficients appearing in expressions (B-4) and (B-7) will be discussed later. K_1, K_2, and K_3 are the bulk moduli; μ_1, μ_2, and μ_3 the shear moduli; C_{12} and C_{23} the coupling coefficients of effective solids (1), of unfrozen water as an effective fluid (2), and of ice as a second effective solid (3).

2) Kinetic energy density C

The displacements of solid, water, and ice are, represented, respectively, by the vectors μ_1, μ_2, and μ_3. The kinetic energy density C($\dot{\mu}_1$, $\dot{\mu}_2$, $\dot{\mu}_3$) is a function of local velocities $\dot{\mu}_1$, $\dot{\mu}_2$, and $\dot{\mu}_3$ given by the time derivative of displacements. With a development of C to the second order and assuming that the phases' motions are only caused by the wave propagation,

$$C = \frac{1}{2}\rho_{11}\dot{\mu}_1^2 + \rho_{12}\dot{\mu}_1\dot{\mu}_2 + \frac{1}{2}\rho_{22}\dot{\mu}_2^2 + \rho_{23}\dot{\mu}_2\dot{\mu}_3 + \frac{1}{2}\rho_{33}\dot{\mu}_3^2$$

(Eq. B-8)

where ρ_{ij} are the elements of an induced mass tensor. The crossed terms characterize the transfer of kinetic energy between solids and water and between ice and water. When an elastic wave propagates, local displacements of matter occur. In a porous medium, the phases tend to have local velocities different from one another since sinuous fluid flows may occur in pores. Phases with different mass densities filling the same

space at macroscopic scale imply exchanges of momentum between them. In fact, the motion of one phase may induce the motion of another one by inertial effect. This phenomenon, designated as inertial coupling, becomes more important as the tortuosity of the medium increases. Here again, the crossed term in $\dot{\mu}_1 \dot{\mu}_3$ has been rejected since there is no contact between solids and ice.

The variation of kinetic energy may be expressed by the differential form:

$$dC = \frac{\partial C}{\partial \dot{\mu}_1} d\dot{\mu}_1 + \frac{\partial C}{\partial \dot{\mu}_2} d\dot{\mu}_2 + \frac{\partial C}{\partial \dot{\mu}_3} d\dot{\mu}_3 \qquad \text{(Eq. B-9)}$$

Three generalized momenta are defined in this expression:

$$\pi_1 = \frac{\partial C}{\partial \dot{\mu}_1} = \rho_{11}\dot{\mu}_1 + \rho_{12}\dot{\mu}_2$$

$$\pi_2 = \frac{\partial C}{\partial \dot{\mu}_2} = \rho_{12}\dot{\mu}_1 + \rho_{22}\dot{\mu}_2 + \rho_{23}\dot{\mu}_3$$

$$\pi_3 = \frac{\partial C}{\partial \dot{\mu}_3} = \rho_{23}\dot{\mu}_2 + \rho_{33}\dot{\mu}_3 \qquad \text{(Eq. B-10)}$$

Here, ρ_{11}, ρ_{22}, and ρ_{33} are, respectively, the mass density of the effective solid, of water as effective fluid, and of ice as a second effective solid; ρ_{12}, ρ_{23} are the mass densities induced by inertial coupling between solids and water and between ice and water. All these coefficients are the elements of the mass tensor and will be discussed later.

3) Dissipation potential D

In Leclaire et al's study, only dissipations caused by viscous flows are considered. The internal thermoconduction phenomena in solids or the frictions between solid grains are not studied in this dissertation, and the losses caused by the presence of microbubbles of air also neglected. The medium is assumed to be totally saturated.

The dissipations potential D caused by viscous flows is given as:

$$D = \frac{1}{2} b_{11} |\dot{\mu}_{1-}\dot{\mu}_2|^2 + \frac{1}{2} b_{33} |\dot{\mu}_{2-}\dot{\mu}_3|^2$$

(Eq. B-11)

where b_{11} and b_{33} are real coefficients of a diagonal matrix and may be called, respectively, the friction coefficients between solids and water and between ice and water.

4) Equations of motion

The equations of motion are deduced using Lagrange's equations. Leclaire et al. (1994) take a simple form, using the expressions of stress tensors (B-7) and of generalized momenta (B-10):

$$\sigma_{ij,j}^{(1)} = \dot{\pi}_1 + b_{11}(\dot{\mu}_2 - \dot{\mu}_1)$$

$$\sigma_{,j}^{(2)} = \dot{\pi}_2 + b_{11}(\dot{\mu}_2 - \dot{\mu}_1) - b_{33}(\dot{\mu}_2 - \dot{\mu}_3)$$

$$\sigma_{ij,j}^{(3)} = \dot{\pi}_3 + b_{33}(\dot{\mu}_2 - \dot{\mu}_3)$$

(Eq. B-12)

The equations of motion are written in matrix form by substituting the expressions (7) and (10) in (12):

$$\overline{R}.grad.div.\overline{u} - \overline{\mu}.curl.curl.\overline{u} = \overline{\rho}\ddot{\overline{u}} + \overline{A}\dot{\overline{u}} \qquad\qquad \text{(Eq. B-13)}$$

where the notation $\overline{X}$ designates the matrix associated with the parameter X. The term $\overline{u}$ is the local displacement matrix. Also, $\dot{\overline{u}}$ is the velocities matrix, and $\ddot{\overline{u}}$ is the acceleration matrix.

The matrices of mass densities and friction coefficients are given by

$$\overline{\rho} = \begin{pmatrix} \rho_{11} & \rho_{12} & 0 \\ \rho_{21} & \rho_{22} & \rho_{23} \\ 0 & \rho_{32} & \rho_{33} \end{pmatrix}$$

and

$$\overline{A} = \begin{pmatrix} b_{11} & -b_{11} & 0 \\ -b_{11} & b_{11}+b_{33} & -b_{33} \\ 0 & -b_{33} & b_{33} \end{pmatrix}$$

Matrices of bulk and shear stiffness moduli are

$$\overline{R} = \begin{pmatrix} R_{11} & R_{12} & 0 \\ R_{21} & R_{22} & R_{23} \\ 0 & R_{32} & R_{33} \end{pmatrix}$$

and

$$\overline{\mu} = \begin{pmatrix} \mu_{11} & 0 & 0 \\ 0 & 0 & 0 \\ 0 & 0 & \mu_{33} \end{pmatrix},$$

whose elements are given by

$$R_{11} = K_1 + \frac{4}{3}\mu_1, \quad R_{12} = R_{21} = C_{12}, \quad R_{22} = K_2$$

$$R_{23} = R_{32} = C_{23}, \quad R_{33} = K_3 + \frac{4}{3}\mu_3 \qquad \text{(Eq. B-14)}$$

$$\mu_{11} = \mu_1, \quad \mu_{33} = \mu_3 \qquad \text{(Eq. B-15)}$$

5) Equations of propagation

Longitudinal solutions:

In the first step, Leclaire et al. assumed the case without attenuation, disregarding the matrix $\overline{A}$ of friction coefficients. If rigidity and mass density matrices are symmetrical and with real coefficients and if the conditions for the kinetic and potential energies to be positive definite forms have been previously determined by diagonalizing p and R separately, for longitudinal solutions one may find the condition

$$\left|\overline{\rho} - \Lambda_i \overline{R}\right| = 0 \qquad \text{(Eq. B-16)}$$

The coefficients Λ_i are called the eigenvalues of $\overline{\rho}$ relative to $\overline{R}$. Eq. B-16 can be expressed as a third-degree characteristic equation:

$$\Lambda^3 \det \overline{R} - \Lambda^2 \left[\rho_{11} \det \overline{R}_{iw} + \rho_{22} \det \overline{R}_{si} + \rho_{33} \det \overline{R}_{sw}) - 2(R_{11}R_{23}\rho_{23} + R_{33}R_{12}\rho_{12})\right]$$
$$+ \Lambda[R_{11} \det \overline{\rho}_{iw} + R_{22} \det \overline{\rho}_{si} + R_{33} \det \overline{\rho}_{sw}) - 2(R_{11}R_{23}\rho_{23} + R_{33}R_{12}\rho_{12})] - \det \overline{\rho} = 0$$

or

$$A\Lambda^3 - [\rho_{11}B + \rho_{22}C + \rho_{33}D - 2(R_{11}R_{22}\rho_{23} + R_{33}R_{12}\rho_{12})]\Lambda^2$$
$$+ [bR_{11} + cR_{22} + dR_{33} - 2(\rho_{11}\rho_{23}R_{23} + \rho_{33}\rho_{12}R_{12})]\Lambda - a = 0 \qquad \text{(Eq. B-17)}$$

with

$$A = \det \overline{R} = R_{11}R_{22}R_{33} - R_{23}^2 R_{11} - R_{12}^2 R_{33}$$

$$B = \det \overline{R}_{iw} = R_{22}R_{33} - R_{23}^2$$

$$C = \det \overline{R}_{si} = R_{11}R_{33}$$

$$D = \det \overline{R}_{sw} = R_{11}R_{22} - R_{12}^2$$

$$a = \det \overline{\rho} = \rho_{11}\rho_{22}\rho_{33} - \rho_{23}^2\rho_{11} - \rho_{12}^2\rho_{33}$$

$$b = \det \overline{\rho}_{iw} = \rho_{22}\rho_{33} - \rho_{23}^2$$

$$c = \det \overline{\rho}_{si} = \rho_{11}\rho_{33}$$

$$d = \det \overline{\rho}_{sw} = \rho_{11}\rho_{22} - \rho_{12}^2$$

The longitudinal wave velocities are given by the relationship

$$\Lambda = k^2 / \omega^2 = 1 / V_L^2$$

where k is the wave number and ω the angular frequency.

As a second step, they added attenuation into the study by introducing $\overline{A}$ in the formulation. A linear relationship exists between local velocities and accelerations for time sinusoidal displacements:

$$\dot{\varphi}_i = -(j / \omega)\ddot{\varphi}_i$$

where j is the imaginary unit complex number ($j^2 = -1$) and φ_i is scalar

potential.

Thus the complex term $j^{A_{ij}}/\omega$ must be subtracted from each element ρ_{ij} of the

mass density matrix in the characteristic equation (B-17). Hence ,a new characteristic

equation is obtained with complex coefficients:

$$Z_3\Lambda^3 - Z_2\Lambda^2 + Z_1\Lambda - Z_0 = 0 + 0j \qquad \text{(Eq. B-18)}$$

The three complex solutions are

$$\Lambda_i^{1/2} = R_i + jI_i, \quad i = 1,2\ldots\ldots,3$$

The three compressional velocities of the three-phase frozen porous medium are

given by

$$V_{Pi} = [\text{Re}(\sqrt{\Lambda_i})]^{-1}, \quad i = 1,2\ldots\ldots,3 \qquad \text{(Eq. B-19)}$$

where $\text{Re}()$ denotes the real part of the roots of Eq. B-18.

And the three corresponding attenuation coefficients are given by

$$a_{Li} = \omega/I_i, \quad i = 1,2\ldots\ldots,3$$

Transverse solutions:

The transverse solutions are obtained by replacing the rigidity matrix $\overline{R}$ with the

shear moduli matrix $\overline{\mu}$ in the equations. Disregarding the matrix $\overline{A}$, the characteristic

equation for transverse waves is written as

$$\Lambda^2 \rho_{22} \det \overline{\mu}_{si} - \Lambda(\mu_{11} \det \overline{\rho}_{iw} + \mu_{33} \det \overline{\rho}_{sw} + \det \overline{\rho} = 0 \qquad \text{(Eq. B-20)}$$

with $\det \overline{\mu}_{si} - \mu_{11}\mu_{33}$

Replacing ρ_{ij} by $\rho_{ij} - j^{A_{ij}} / \omega$ in B-20 leads to the resolution of a second-degree characteristic equation with complex coefficients. The solutions are

$$\Lambda_i^{1/2} = R_i + jI_i, \quad i = 1,2$$

The two transverse wave velocities are given by

$$V_{Ti} = [\text{Re}(\sqrt{\Lambda_i})]^{-1}, \quad i = 1,2$$

And the two corresponding attenuation coefficients are

$$a_{Ti} = \omega / I_i, \quad i = 1,2$$

6) Determination of the generalized elastic coefficients R_{ij}

For a fluid-saturated porous medium (without ice), three generalized elastic coefficients R_{ij} were defined in Biot's theory as

$$R_{11} = [(1-c_1)\phi_s]^2 K_{av} + K_{sm} + \frac{4}{3}\{[(1-g_1)\phi_s]^2 \mu_{av}\}$$

$$R_{12}[(1-c_1)\phi_s]\phi_w K_{av}$$

$$R_{22} = \phi_w^2 K_{av} \qquad \text{(Eq. B-21)}$$

The bulk consolidation coefficient for solids, c_1, and for ice (c_3), are

$$c_1 = K_{sm} / \phi_s K_s$$

$$c_3 = K_{im} / \phi_i K_i$$

The average bulk modulus is defined as

$$K_{av} = [(1 - c_1)\phi_s / K_s + \phi_w / K_w + (1 - c_3)\phi_i / K_i]^{-1}$$

The coefficients appearing in Eq. B-4 and B-7 are deduced by a simple analogy with the coefficients given in Eq. B-21:

$$K_1 = [(1 - c_1)\phi_s]^2 K_{av} + K_{sm}$$

$$K_2 = \phi_w^2 K_{av}$$

$$K_3 = [(1 - c_3)\phi_i]^2 K_{av} + K_{im}$$

$$C_{12} = [(1 - c_1)\phi_s]^2 \phi_w K_{av}$$

$$C_{23} = [(1 - c_3)\phi_i]\phi_w K_{av}$$

where K_s, K_w, and K_i are the bulk moduli of solids, water, and ice, respectively. K_{sm} and K_{im} are the bulk moduli of the solids matrix and the ice matrix.

The shear moduli μ_1 and μ_3 defined in in Eq. B-4 and B-7 are given by:

$$\mu_1 = [(1 - g_1)\phi_s]^2 \mu_{av} + \mu_{sm}$$

$$\mu_2 = [(1 - g_3)\phi_i]^2 \mu_{av} + \mu_{im}$$

where a shear coefficient of consolidation g_1 is defined for solids matrix and g_3 for the ice matrix as

$$g_1 = \mu_{sm} / \phi_s \mu_s$$

$$g_3 = \mu_{im} / \phi_i \mu_i$$

An average shear modulus, including the effect of water viscosity, is also defined for frozen porous media as

$$\mu_{av} = [(1 - g_1)\phi_s / \mu_s + \phi_w / 2\omega\eta_w + (1 - g_3)\phi_i / \mu_i]^{-1}$$

where μ_s and μ_i are the solid and ice shear moduli, respectively; μ_{sm} and μ_{im} the shear moduli of solid and ice matrices.

The ice matrix elastic moduli are evaluated as functions of ice proportion ϕ_i by

$$K_{im} = K_{KT}[\phi_i /(1 - \phi_s)]^{3.8}$$

$$\mu_{im} = \mu_{KT}[\phi_i /(1 - \phi_s)]^{3.8}$$

where K_{KT} and μ_{KT} are Kuster-Toksöz's bulk and shear modulus, respectively. They are obtained from the classical model:

$$\frac{K_{KT}}{K_i} = \frac{1+[4\mu_i(K_a - K_i)/((3K_a + 4\mu_i)K_i)]\phi_s}{1-[3(K_a - K_i)/(3K_a + 4\mu_i)]\phi_s}$$

$$\frac{\mu_{KT}}{\mu_i} = \frac{(6K_i +12\mu_i)\mu_a +(9K_i +8\mu_i)[(1-\phi_s)\mu_i +\phi_s\mu_a]}{(9K_i +8\mu_i)\mu_i +(6K_i +12\mu_i)[(1-\phi_s)\mu_a +\phi_s\mu_i]}$$

7) Determination of the generalized mass densities ρ_{ij}

The generalized mass densities ρ_{ij} are obtained from the identification of the coefficients of Eq. B-8:

$$\rho_{11} = \phi_s \rho_s + (a_{12} - 1)\phi_w \rho_w - ib_1 / \omega$$

$$\rho_{12} = -(a_{12} - 1)\phi_w \rho_w + ib_1 / \omega$$

$$\rho_{22} = (a_{12} + a_{23} - 1)\phi_w \rho_w - i(b_1 + b_3) / \omega$$

$$\rho_{23} = -(a_{23} - 1)\phi_w \rho_w + ib_3 / \omega$$

$$\rho_{33} = \phi_i \rho_i + (a_{23} - 1)\phi_w \rho_w - ib_3 / \omega$$

8) Determination of coefficients a_{12} and a_{23}

Assuming no direct contact between solid and ice and no water-ice relative motion, the solid matrix is surrounded by a fluid like medium whose mass density is given by

$$\rho = (\phi_w \rho_w + \phi_i \rho_i) / (\phi_w + \phi_i)$$

This problem is equivalent to the problem of inertial coupling in a fluid-saturated porous medium and already has been studied (Biot, 1956a). The inertial drag parameter a_{12} of the order of tortuosity is deduced using the results given by Berryman (1980):

$$a_{12} = a_{21} = r_{12}(\phi_s \rho) / (\phi_w \rho_w) + 1$$

where r_{12} characterizes the geometrical aspect of the boundary separating solids from water; $r_{12} = 0.5$ for spheres. Similarly, a_{23} is given as a function of the geometrical parameter r_{23} characterizing the ice-water boundary by

$$a_{23} = a_{32} = r_{23}(\phi_i \rho')/(\phi_w \rho_w) + 1$$

with

$$\rho' = (\phi_w \rho_w + \phi_s \rho_s)/(\phi_w + \phi_s)$$

9) Determination of the friction coefficients b_{11} and b_{33}

If $b_{33} = 0$, Using Darcy's law, b_{11} is expressed as a function of the solid matrix permeability k_s as

$$b_{11} = \eta_D \phi_w^2 / k_s$$

Similarly, if $b_{11} = 0$, b_{33} is expressed as a function of the ice matrix permeability k_i as

$$b_{33} = \eta_D \phi_w^2 / k_i$$

Table B-1. The expressions in Leclaire et al's model

Symbols	Expressions
A	$R_{11}R_{22}R_{33} - R_{23}^2 R_{11} - R_{12}^2 R_{33}$
B	$R_{22}R_{33} - R_{23}^2$
C	$R_{11}R_{33}$
D	$R_{11}R_{22} - R_{12}^2$
a	$\rho_{11}\rho_{22}\rho_{33} - \rho_{23}^2\rho_{11} - \rho_{12}^2\rho_{33}$
b	$\rho_{22}\rho_{33} - \rho_{23}^2$
c	$\rho_{11}\rho_{33}$
d	$\rho_{11}\rho_{22} - \rho_{12}^2$
R_{11}	$[(1-c_1)\phi_s]^2 K_{av} + K_{sm} + \dfrac{4}{3}\{[(1-g_1)\phi_s]^2 \mu_{av} + \mu_{sm}\}$
R_{12}	$[(1-c_1)\phi_s]\phi_w K_{av}$
R_{22}	$\phi_w^2 K_{av}$
R_{23}	$[(1-c_3)\phi_i]\phi_w K_{av}$
R_{33}	$[(1-c_3)\phi_s]^2 K_{av} + K_{im} + \dfrac{4}{3}\{[(1-g_3)\phi_i]^2 \mu_{av} + \mu_{im}\}$
ρ_{11}	$\phi_s \rho_s + (a_{12}-1)\phi_w\rho_w - ib_1/\omega$
ρ_{12}	$-(a_{12}-1)\phi_w\rho_w + ib_1/\omega$
ρ_{22}	$(a_{12}+a_{23}-1)\phi_w\rho_w - i(b_1+b_3)/\omega$
ρ_{23}	$-(a_{23}-1)\phi_w\rho_w + ib_3/\omega$
ρ_{33}	$\phi_i\rho_i + (a_{23}-1)\phi_w\rho_w - ib_3/\omega$
b_{12}	$\eta_D\phi_w^2/k_s$
b_{23}	$\eta_D\phi_w^2/k_i$
k_s	$k_{s0}\phi_w^3/(1-\phi_s)^3$
k_i	$k_{i0}[(1-\phi_s)/\phi_i]^2 (\phi_w/\phi_s)^3$
a_{12}	$r_{12}(\phi_s\rho)/(\phi_w\rho_w)+1$
a_{23}	$r_{23}(\phi_i\rho')/(\phi_w\rho_w)+1$
ρ	$(\phi_w\rho_w + \phi_i\rho_i)/(\phi_w+\phi_i)$
ρ'	$(\phi_w\rho_w + \phi_s\rho_s)/(\phi_w+\phi_s)$
μ_1	$[(1-g_1)\phi_s]^2 \mu_{av} + \mu_{sm}$
μ_3	$[(1-g_3)\phi_i]^2 \mu_{av} + \mu_{im}$
B'	$\rho_{11}B + \rho_{22}C + \rho_{33}D - 2(R_{11}R_{22}\rho_{23} + R_{33}R_{12}\rho_{12})$
C'	$bR_{11} + cR_{22} + dR_{33} - 2(\rho_{11}\rho_{22}R_{23} + \rho_{33}\rho_{12}R_{12})$
a'	$\rho_{22}\mu_1\mu_3$
b'	$\mu_1 b + \mu_3 d$